



TECHNISCHE UNIVERSITÄT BERLIN
FAKULTÄT IV
FACHGEBIET THEORETISCHE
ELEKTROTECHNIK
Master Thesis

In collaboration with: European Organization for Nuclear Research (CERN)

**Framework for automatic superconducting
magnet model generation & validation
against transients measured in LHC
magnets**

Candidate:
Marvin Janitschke
Mat. Nr.: 371493

Coordinator:
Prof. Dr. Rolf Schuhmann
(TU Berlin)

Advisor:
Prof. Dr. Friedel Gerfers
(TU Berlin)

Co-Advisor:
Dr. Emmanuele Ravaioli (CERN)

Abstract

Superconducting magnet circuits are a key part of particle accelerators. Simulating complex transients occurring in these circuits with dedicated models is crucial to analyze their behavior and assess the impact of failure cases. The recently developed STEAM framework from CERN tackles this challenge with a series of dedicated software tools and model libraries. These models need to be validated and evaluated against experimental transients. This thesis discusses a newly developed addition to the STEAM framework, which provides the possibility to automatically generate and validate the superconducting magnet models, and hence to significantly shorten the required time and effort to validate such models. This is achieved by conducting a parametric sweep analysis aiming at determining the unknown model parameters. The developed solution is supplementing the already existing Python programming interface within the STEAM framework for the model generation. Its usage, implementation, and integration into the framework is described. This thesis presents the application on two different use cases of LHC superconducting magnets. These achieve an excellent agreement between simulations and measurements collected during LHC operation. Furthermore, it is shown that this solution can also be used to predict the occurrence of specific behavior in the superconducting magnets such as quench-back. The application on a specific use-case on multiple quench events in the main bending dipoles of the LHC presents a way to offer simulation results to quickly and easily support the everyday operation of the accelerator. Therefore, this thesis can be seen as a guideline and presentation of the practicability, abilities, and limitations of the automated framework.

Zusammenfassung

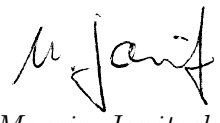
Supraleitende Magneten und ihre elektrischen Schaltungen sind ein wesentlicher Bestandteil von Teilchenbeschleunigern. Die Simulation von den komplexen Ausgleichsvorgängen und ihres Verhaltens mittels geeigneter Modelle ist entscheidend, um den Einfluss von eventuellen Fehlern zu analysieren, zu bewerten und einordnen zu können. Das vom CERN vor Kurzem neu entwickelte STEAM-Framework zielt darauf ab, dieses Problem mittels einer Reihe von Softwareprogrammen und Modelbibliotheken zu lösen. Diese Modelle müssen jedoch durch den Vergleich mit Messdaten zunächst validiert werden. Diese Arbeit diskutiert eine neue Ergänzung zu dem Framework, welche die Möglichkeit schafft, die Modelle der supraleitenden Magnete und ihrer elektrischen Schaltungen vollautomatisch zu validieren und dadurch, die benötigte Zeit und Arbeit signifikant zu reduzieren. Dies wird durch eine parametrische Analyse erreicht, die darauf abzielt, die unbekannten Modelparameter zu bestimmen. Das neue Konzept ergänzt dabei das bestehende Pythoninterface und die Anwendung und Einbindung ist genauer beschrieben. Diese Arbeit präsentiert zwei Anwendungsbeispiele an supraleitenden Magneten des LHC. Die dadurch validierten Modelle erzielen eine exzellente Übereinstimmung zwischen Messdaten und Simulationen. Des Weiteren wird in dieser Arbeit gezeigt, dass das neue Konzept auch zur Vorhersage von potenziell auftretenden physikalischen Phänomenen und Verhalten wie beispielsweise 'Quench-Back' genutzt werden kann. Ein Anwendungsfall an multiplen Quench-Events der Beugungsdipole im LHC zeigt einen Weg, wie das neue Konzept bei dem alltäglichen Betrieb assistieren kann. Diese Arbeit kann daher als Leitfaden und Präsentation der Praktikabilität, Fähigkeiten und Grenzen des automatisierten Frameworks angesehen werden.

Erklärung der Urheberschaft

Ich, Marvin Janitschke, erkläre hiermit an Eides statt, dass ich die vorliegende Arbeit ohne Hilfe Dritter und ohne Benutzung anderer als der angegebenen Hilfsmittel angefertigt habe; die aus fremden Quellen direkt oder indirekt übernommenen Gedanken sind als solche kenntlich gemacht. Die Arbeit wurde bisher in gleicher oder ähnlicher Form in keiner anderen Prüfungsbehörde vorgelegt und auch noch nicht veröffentlicht.

Berlin, 21.12.2021

Ort, Datum


Marvin Janitschke

Unterschrift

Contents

| | |
|---|-------------|
| List of abbreviations and symbols | x |
| List of Figures | xiv |
| List of Tables | xxii |
| 1 Introduction | 1 |
| 1.1 European Organization for Nuclear Research | 2 |
| 1.1.1 Large Hadron Collider | 2 |
| 1.1.2 CERN Magnet Test Facility - SM18 | 3 |
| 1.2 Superconductivity and Superconducting magnets | 4 |
| 1.2.1 Superconducting cable | 6 |
| 1.2.2 Quench | 7 |
| 1.2.3 Coupling currents | 10 |
| 1.2.4 Quench protection systems | 12 |
| 1.3 LHC superconducting circuits | 14 |
| 2 Modelling of superconducting magnets | 17 |
| 2.1 Lumped element modelling | 17 |
| 2.2 Thermal modelling of superconducting magnets | 18 |
| 2.2.1 Thermal lumped element sub-network | 18 |
| 2.2.2 Helium cooling | 21 |
| 2.3 Electro-magnetic modelling of superconducting magnets | 23 |
| 2.3.1 Electro-magnetic lumped element sub-network | 23 |
| 2.3.2 Electrical circuit representation | 24 |
| 2.4 Modelling of coupling currents in superconducting magnets | 25 |
| 2.5 Quench modelling | 26 |
| 2.6 Co-operative simulation | 28 |
| 3 Automatic generation and validation of superconducting magnet models | 31 |
| 3.1 Implementation | 31 |
| 3.2 Validation of a self-protecting 120 A superconducting magnet model . | 33 |
| 3.2.1 The MCBY magnets | 34 |
| 3.2.2 Parameter variation and their impact | 38 |
| 3.3 Validation of the LHC separation and recombination magnet models . | 48 |
| 3.3.1 The LHC separation and recombination magnet models | 49 |
| 3.3.2 Parameter variation and their impact | 51 |

| | |
|--|------------|
| 4 Automatic simulation of future events in LHC superconducting circuits | 61 |
| 4.1 Predicting the occurrence of quench-back | 61 |
| 4.1.1 LHC 600 A circuits | 62 |
| 4.1.2 Prediction of quench-back current in LHC 600 A circuit | 65 |
| 4.2 Analyzing the impact of different quench locations in the example of self-protecting magnets | 69 |
| 5 Automatic generation of LHC main dipole events | 77 |
| 5.1 Typical quench event in the LHC main dipole circuit | 77 |
| 5.2 Hierarchical co-operative simulation | 81 |
| 5.3 Results of hierarchical co-operative simulation of a multiple quench-event | 85 |
| 5.4 Alternative simulation approaches | 96 |
| 6 Conclusion and Outlook | 101 |
| Appendices | 105 |
| A Superconductors | 105 |
| B Strand characteristics | 106 |
| C Cable characteristics | 106 |
| D LHC magnets | 107 |
| E LHC circuits | 110 |
| F Annex to Chapter 3 | 111 |
| G Annex to Chapter 4 | 119 |
| H Annex to Chapter 5 | 125 |
| References | 129 |

List of abbreviations and symbols

Abbreviations

| | |
|--------|--|
| ALICE | A Large Ion Collider Experiment |
| API | Application programming interface |
| ATLAS | A Toroidal LHC ApparatuS |
| CERN | European center for Nuclear Research |
| CLIQ | Coupling loss induced quench |
| CMS | Compact Muon Solenoid |
| DCCT | Direct Current-Current Transformer |
| EE | Energy Extraction |
| FPA | Fast Power Abort |
| HL-LHC | High Luminosity LHC |
| HTS | High-Temperature Superconductor |
| HWC | Hardware Commissioning |
| IFCC | Inter Filament Coupling Currents |
| IFCL | Inter Filament Coupling Loss |
| IPD | Individually Powered Dipoles |
| ISCC | Inter Strand Coupling Currents |
| ISCL | Inter Strand Coupling Loss |
| LHC | Large Hadron Collider |
| NZPV | Normal zone propagation velocity |
| PC | Power Converter |
| QDS | Quench detection system |
| QH | Quench heater |
| QL | Quench load |
| QPS | Quench protection system |
| RMSE | Root mean square error |
| RRR | Residual Resistivity Ratio |
| SC | Superconductor |
| STEAM | Simulation of Transient Effects in Accelerator Magnets |

Latin symbols

| | | |
|----------------|---|-------------------------------------|
| A | Area | [m ²] |
| B | Magnetic field | [T] |
| C_p | Volumetric specific heat | [J/Km ³] |
| \bar{c} | Volumetric heat capacity | [Jm ⁻³ K ⁻¹] |
| d | Diameter | [m] |
| $f_{\rho,eff}$ | Effective transverse resistivity, scaling | [\cdot] |
| E_q | Minimal required quench energy | [J] |
| H | Thermal enthalpy | [J] |
| I | Current level | [A] |
| J | Current density | [A/m ²] |
| l | Length | [m] |
| L | Inductance | [H] |
| p | Perimeter | [m] |
| T | Temperature | [K] |
| v | Velocity | [m/s] |
| V | Volume | [m ³] |

Greek symbols

| | | |
|------------|---------------------------------|-------------------------------------|
| ϵ | Tolerance | [\cdot] |
| κ | Thermal conductivity | [Wm ⁻¹ K ⁻¹] |
| λ | London penetration depth | [m] |
| μ_0 | Magnetic permeability of vacuum | [TmA ⁻¹] |
| ρ | Electric resistivity | [Ω m] |
| Φ | Magnetic flux | [T m ²] |
| χ | Magnetic susceptibility | [\cdot] |

Upper and lower indices

| | |
|------|-----------------|
| Avg | Average |
| Bare | Bare cable |
| c | Critical |
| c1 | Lower critical |
| c2 | Upper critical |
| Circ | Circuit |
| Con | Conductor |
| cs | Current sharing |
| Cu | Copper specific |
| D | Diode |
| f | Filament |
| Ins | Insulation |
| If | Inter-filament |
| Is | Inter-strand |
| Mag | Magnet |
| Meas | Measurement |
| Nom | Nominal |
| Out | Output |
| Par | Parallel |
| q | Quench |
| s | Strand |

List of Figures

| | | |
|-----|---|----|
| 1.1 | CERN’s accelerator complex, illustrating the chain of particle accelerators, used particles and the different included experiments and detectors [6] | 3 |
| 1.2 | Magnetic field versus temperature, illustrating the expulsion of the magnetic field in the case of: a) superconducting state with $B < B_{c1}$ (or $B < B_c$ for type-I superconductors), b) the intermediate phase of type-II superconductors with $B_{c1} < B < B_{c2}$ and c) the normal state with $B > B_{c2}$ [13] | 5 |
| 1.3 | Critical surface of Nb-Ti, showing the J-B cross-section on a typical operational temperature of 1.9 K in grey [14] | 6 |
| 1.4 | Wires made of a) Nb-Ti filaments and b) Nb ₃ Sn filaments, both embedded in a copper stabilizer matrix [17] | 7 |
| 1.5 | a) Top-view and b) cross-section of a typical Nb-Ti Rutherford cable that is used in the LHC main dipole bending magnets [18] | 8 |
| 1.6 | Qualitative temperature evolution in a quench hot-spot just below and above the stability energy margin, that lead to either a thermal runaway or recovery [19] | 9 |
| 1.7 | Illustration of the heat evolution and current redistribution around a quench hot-spot [12] | 10 |
| 1.8 | Quench heater strips attached to parts of an insulated coil of a short MQXF magnet model, showing heating stations and copper-plated areas [26] | 14 |
| 2.1 | Representation of the three coupled sub-networks, used in STEAM-LEDET [16, 24] | 19 |
| 2.2 | Example of an equivalent lumped-element model of an thermal element b and the transition to one neighboring thermal element h, used in earlier versions of LEDET | 20 |
| 2.3 | Simplified graphical representation of a multi-stranded cable, showing different quantities of super-fluid helium (blue) in the voids between the strands(orange) and their insulation (purple). (a) All voids are filled with helium, (b) half of the voids are filled with helium, remaining parts filled with insulation and (c) all voids are filled with insulation and no helium crepted into the cables voids [34] | 22 |
| 2.4 | Equivalent lumped-element model used in LEDET, showing two electric elements a,n and the simplified electrical circuit, including power source, warm resistance and crowbar. Dashed elements can be optionally included. | 24 |
| 2.5 | Equivalent lumped-element model for the inter-filament coupling currents used in LEDET, showing only the coupling current loop for the x-direction | 25 |

LIST OF FIGURES

| | | |
|------|--|----|
| 2.6 | Illustration of the concept of waveform relaxation, showing the coupling of signals x_1 , x_2 between the two simulation tools S_1 , S_2 for multiple time-steps T [41] | 29 |
| 2.7 | Electrical model used in co-operative simulations to combine an electromagnetic thermal field model (providing U_{Field} and $U_{\text{Resistive}}$) and electrical model | 29 |
| 3.1 | Class diagram of the new additions to the STEAM notebook API, providing the possibility to set up a full set of simulations with varying parameter combinations | 32 |
| 3.2 | Magnetic model of the MCBYH magnet | 35 |
| 3.3 | Electrical model of the MCBYH coils | 36 |
| 3.4 | Thermal connections and quench propagation velocity of the MCBYH magnet | 37 |
| 3.5 | Current derivative in one quench event in an MCBYH magnet, shortly before the power abort at $t_{\text{PC}} = -18$ ms | 39 |
| 3.6 | Approximated minimum required quench energy for each turn in the MCBYH magnet at nominal current and indication of all considered quench locations for the validation (marked with Q1-8)) | 40 |
| 3.7 | Current decay in the MCBYH magnet for all performed simulations, showing the root-mean-square error (RMSE) compared to measurements, after a fast power abort at $t_{\text{PC}} = 0$ s. | 41 |
| 3.8 | Relative difference of the simulated quench loads and measured quench load as a function of simulation numbers. Color gradients indicate the distribution of simulated parameter | 42 |
| 3.9 | Ablation analysis of the MCBYH model to the selected parameter. Dependency of the inverse RMSE to changing one parameter at a time. If not changed, values are fixed to $\text{RRR} = 75$, $f_{\rho,\text{eff}} = 2.1$ and Quench position 4. | 44 |
| 3.10 | Simulated current decays for various values of $f_{\rho,\text{eff}}$, compared to a measurement. $\text{RRR} = 75$ and quench position 4 are fixed. | 45 |
| 3.11 | Simulated current decays for various initial quench positions, compared to a measurement. $\text{RRR} = 75$ and $f_{\rho,\text{eff}} = 2.1$ are fixed. | 45 |
| 3.12 | Simulated current decays for various values of RRR , compared to a measurement. $f_{\rho,\text{eff}} = 2.1$ and quench position 4 are fixed. | 46 |
| 3.13 | Evolution of the simulated coil resistance compared to experimental coil-resistance for selected simulations from Table 4. | 47 |
| 3.14 | Simulated fractions of conductor in the normal state (solid lines) and simulated hot-spot temperatures (dashed lines) for selected simulations from Table 4. | 48 |
| 3.15 | Magnetic field in the MBRS coils, calculated using ROXIE [43, 44] and including iron yoke effect | 50 |

| | | |
|------|---|----|
| 3.16 | Cross-section of one MBRS aperture and the location of their attached quench heater strips. Width of the quench heater strips are increased for the illustration. | 51 |
| 3.17 | Current decay in the MBRB magnet for all performed simulations, compared to measurements, after a fast power abort at $t_{PC} = 0$ s and quench heater firing at $t_{QH} = 2$ ms. | 53 |
| 3.18 | Relative difference of the simulated quench loads and measured quench load as a function of simulation numbers for the MBRB magnet | 54 |
| 3.19 | Enlarged section of the first 216 simulations and their relative difference of the simulated quench loads and measured quench load for the MBRB magnet | 54 |
| 3.20 | Ablation analysis of the MBRB model to the selected parameter. Dependency of the inverse RMSE to changing one parameter at a time. If not changed, values are fixed to $RRR = 68$, $f_{\rho,\text{eff}} = 1.4$, $f_{He} = 1.2\%$ and $R_C = 4 \cdot 10^{-6} \Omega$ | 56 |
| 3.21 | Simulated current decays for various values of RRR in the MBRB magnet model, compared to a measurement. $f_{\rho,\text{eff}} = 1.4$, $f_{He} = 1.2\%$ and $R_C = 4 \cdot 10^{-6} \Omega$ are fixed. | 57 |
| 3.22 | Simulated current decays for various values of f_{He} in the MBRB magnet model, compared to a measurement. $f_{\rho,\text{eff}} = 1.4$, $RRR = 68$ and $R_C = 4 \cdot 10^{-6} \Omega$ are fixed. | 57 |
| 3.23 | Simulated current decays for various values of $f_{\rho,\text{eff}}$ in the MBRB magnet model, compared to a measurement. $f_{He} = 1.2\%$, $RRR = 68$ and $R_C = 4 \cdot 10^{-6} \Omega$ are fixed. | 58 |
| 3.24 | Simulated current decays for various values of f_{He} in the MBRB magnet model, compared to a measurement. $f_{\rho,\text{eff}} = 1.4$, $RRR = 68$ and $f_{He} = 1.2\%$ are fixed. | 59 |
| 3.25 | Comparison of measurements and best fitting simulations for the current decay (a) and coil resistance (b). Chosen simulations are MBRB (Simulation number 1045), MBRC (254) and MBRS (145). | 60 |
| 4.1 | Generalized electrical circuit schematic of the LHC 600 A circuits. The parallel resistor R_{Par} and the energy extraction system are not present in all circuits (see Table 9). Nominal current $I_{Nom} = 550$ A and $R_{Crow} = 50$ m Ω . Energy extraction system is simplified. Circuit current is measured in the DCCT (Direct current-current transformer) | 62 |
| 4.2 | Simulated current discharge on different level in the RSD2.A34B1 circuit, after the power supply is switched off at $t_{PC} = 0$ s, for the simulations with and without an initial quench, representing a case with 'high' quench-back significance. | 67 |

| | | |
|-----|--|----|
| 4.3 | Time and cause of quench in each half-turn of one MS magnet aperture in the RSD circuit during a fast power abort transient at $t_{PC} = 0$ s from $I_{PC} = 550$ A. Causes refer to turns, either quenched by coupling losses or to turns, quenched by heat diffusion through insulation or electrical connections. | 68 |
| 4.4 | Magnetic field in the MCBYH coil turns and indicating the positions of the selected initial quench locations | 70 |
| 4.5 | Evolution of the hot-spot temperature in the MCBYH turns in an FPA at $t_{PC} = 0$ s for all selected initial quench positions from nominal current. Colors indicate the number of turns in the coil-block of the first quenching turn. | 71 |
| 4.6 | Development of the coil resistance in an FPA at $t_{PC} = 0$ s for all selected initial quench positions from nominal current. | 72 |
| 4.7 | Development of the amount of conductor in normal state in an FPA at $t_{PC} = 0$ s for all selected initial quench positions from nominal current. | 73 |
| 4.8 | Voltage across the MCBYH dipole in an FPA at $t_{PC} = 0$ s for all selected initial quench positions from nominal current. Colors indicate the initial magnetic field in the first quenching turn. | 74 |
| 4.9 | Decay of the magnet current in an FPA at $t_{PC} = 0$ s for all selected initial quench positions from nominal current. Colors indicate the initial magnetic field in the first quenching turn. | 74 |
| 5.1 | Illustration of the RB circuit in the LHC [56]. Numbering of the magnets shows the physical order in the chain, differing from the electrical order. | 78 |
| 5.2 | Measured discharge in one RB circuit, showing the measured circuit current I_{Meas} and current-to-current derivative ratio $-I_{Meas} \cdot \left(\frac{dI_{Meas}}{dt}\right)^{-1}$ compared to a reference, measured current [55]. RB.A78 circuit, 28.03.2021-22h09. | 79 |
| 5.3 | Measured discharge in one RB circuit, showing the current discharge (blue) and the measured voltages across the cold by-pass diodes $U_{Diode, RB}$ in different colors [55]. RB.A78 circuit, 28.03.2021-22h09. | 80 |
| 5.4 | Qualitative forward characteristics of the protection diode of MB magnets at different temperatures [27] | 81 |
| 5.5 | Hierarchical co-operative approach to simulate multiple quench events in RB circuits. Blue indicates moments of quench in magnets of the chain, red the time window for full co-operative simulations and green the time window for the PSPICE [©] simulation. Numbers show the simulation order. | 82 |
| 5.6 | Simplified and slightly edited output file of the HWC notebook, analyzing an RB event | 83 |

| | | |
|------|---|-----|
| 5.7 | Magnetic field in the MB coils, calculated using ROXIE [61] and including iron yoke effects, showing the two assumed quench positions (a) and (b) in the two apertures. Positions of quench heater strips on the coil are indicated in black. Width of heater strips is increased for illustration. | 85 |
| 5.8 | Simulated current discharge in the RB circuit, compared to a purely exponential decay with $\tau_{\text{EE}} = 102$ s, as well as all currents in the quenching magnets and their protection diodes | 86 |
| 5.9 | Current discharge in the RB circuits as well as in all quenching magnets and their diodes. a)-d) show the respective zoom for the different quenches | 87 |
| 5.10 | Coupling current losses in the first quenching MB magnet in the first 500 ms of the transient | 88 |
| 5.11 | Peak-temperatures in the strands of the first quenching MB magnet, with an initial current of $I_q = 11177$ A | 89 |
| 5.12 | Development of the MB coil resistance during the simulation. $t = 0$ s corresponds to the start of each simulation. | 90 |
| 5.13 | Voltages across each magnet for the full discharge in the RB circuit. Color grading describes the electrical position in the chain of magnets. | 92 |
| 5.14 | Voltages across each magnet in the RB circuit, zoomed around power abort at t_{PC} and the opening voltages of the energy extraction systems $t_{\text{EE},1}$, $t_{\text{EE},2}$ | 93 |
| 5.15 | Leakage currents to ground in the grounding system of the RB circuit, zoomed around the power abort and the opening times of the two EE systems | 94 |
| 5.16 | Pre-simulated coil-resistances on different current level and the interpolated coil-resistance, used for the final simulation | 97 |
| 5.17 | Normalized differences of the different simulation approaches for the currents in the RB circuit. I_{Δ}^* indicates the difference between the full COSIM simulation and the interpolation approach, I_{Δ}^{**} the difference between full COSIM and the LEDET-only approach. | 98 |
| 5.18 | Development of the coil-resistances for the different quenching magnets (colors follow Figure 5.12) for the three presented simulation approaches | 99 |
| F.1 | Electrical connections of the different groups of conductor (here: layers) in the MCBYH magnet. Only the Go-lines are shown, the return lines are in the respective other pole. | 113 |
| F.2 | Evolution of the simulated coil resistance compared to experimental coil-resistance for the different applied values for RRR. $f_{\rho,\text{eff}} = 2.1$ and quench position 4 are fixed. | 114 |

LIST OF FIGURES

| | | |
|------|--|-----|
| F.3 | Evolution of the simulated coil resistance compared to experimental coil-resistance for the different investigated quench positions. RRR=75 and $f_{\rho,\text{eff}} = 2.1$ are fixed. | 115 |
| F.4 | Evolution of the simulated coil resistance compared to experimental coil-resistance for the different applied values for $f_{\rho,\text{eff}}$. RRR = 75 and quench position 4 are fixed. | 115 |
| F.5 | Current decay in the MBRC magnet for all performed simulations, compared to measurements, after a fast power abort at $t_{\text{PC}} = 0$ s and quench heater firing at $t_{\text{QH}} = 2$ ms. | 116 |
| F.6 | Current decay in the MBRS magnet for all performed simulations, compared to measurements, after a fast power abort at $t_{\text{PC}} = 0$ s and quench heater firing at $t_{\text{QH}} = 2$ ms. | 116 |
| F.7 | Relative difference of the simulated quench loads and measured quench load as a function of simulation numbers for the MBRC magnet . . . | 117 |
| F.8 | Relative difference of the simulated quench loads and measured quench load as a function of simulation numbers for the MBRS magnet . . . | 117 |
| F.9 | Ablation analysis of the MBRC model to the selected parameter. Dependency of the inverse RMSE to changing one parameter at a time. If not changed, values are fixed to RRR = 101, $f_{\rho,\text{eff}} = 1.4$, $f_{\text{He}} = 1\%$ and $R_C = 4 \cdot 10^{-6} \Omega$ | 118 |
| F.10 | Ablation analysis of the MBRS model to the selected parameter. Dependency of the inverse RMSE to changing one parameter at a time. If not changed, values are fixed to RRR = 68, $f_{\rho,\text{eff}} = 1$, $f_{\text{He}} = 0\%$ and $R_C = 2.5 \cdot 10^{-4} \Omega$ | 118 |
| G.11 | Simulated current discharge on different current level in the RQSX3.L1 circuit, after the power supply is switched off at $t_{\text{PC}} = 0$ s, for the simulations with and without an initial quench, representing a case with 'medium' quench-back significance | 120 |
| G.12 | Simulated current discharge on different current level in the ROD.A12B2 circuit, after the power supply is switched off at $t_{\text{PC}} = 0$ s, for the simulations with and without an initial quench, representing a case with 'low' quench-back significance | 120 |
| G.13 | Simulated current discharge on different current level in the RQTL11.R5B1 circuit, after the power supply is switched off at $t_{\text{PC}} = 0$ s, for the simulations with and without an initial quench, representing a case with no expected quench-back | 121 |
| G.14 | Magnetic field in the coil of one aperture of the MS magnet, calculated using ROXIE [43, 44] and including iron yoke effects | 121 |
| G.15 | Development of the coil resistance in an FPA at $t_{\text{PC}} = 0$ s for all selected initial quench positions from nominal current. Colors indicate the number of neighboring turns to the first quenching turn. | 122 |

| | |
|---|-----|
| G.16 Development of the amount of conductor in normal state in an FPA at $t_{PC} = 0$ s for all selected initial quench positions from nominal current. Colors indicate the initial magnetic field in the first quenching turn. | 123 |
| G.17 Voltage across the MCBYH dipole in an FPA at $t_{PC} = 0$ s for all selected initial quench positions from nominal current. Colors indicate the electrical position of the assumed quench hot-spot, with negative lead at 5370 and positive lead at 0. | 123 |
| G.18 Decay of the magnet current in an FPA at $t_{PC} = 0$ s for all selected initial quench positions from nominal current. Colors the number of neighboring turns to the first quenching turn. | 124 |
| H.19 Cause of quench of each half-turn in the first quenching MB magnet, for the presented event in Chapter 5 | 125 |
| H.20 Time of quench of each half-turn in the first quenching MB magnet, for the presented event in Chapter 5 | 125 |
| H.21 Fraction of conductor, transferred into normal state for the simulations at different current levels. $t = 0$ s corresponds to the start of each simulation. | 126 |
| H.22 Remaining current flow in the magnets after the discharge in each magnet, shown for each quenching magnet | 127 |
| H.23 Voltages across each magnet in the RB circuit, shortly after the second quench at $t_{q,2}$ in the magnet with the electrical position 126 | 127 |

List of Tables

| | | |
|----|---|-----|
| 1 | Classification of quench protection systems and some frequently used examples | 13 |
| 2 | Main magnet and conductor parameters of the LHC MCBY magnet [1], used in the simulations | 34 |
| 3 | Simulation summary for the validation of the self-protecting magnet MCBYH | 40 |
| 4 | Obtained errors and quench loads for the selected best and worst simulations in the set of conducted simulations. Quench load of the measurement: $QL_{Meas} = 2.377 \text{ kA}^2\text{s}$ | 43 |
| 5 | Main magnet and conductor parameters of the LHC IPD magnets [1], used in the simulations | 49 |
| 6 | Simulation summary for the validation of the interaction point dipoles | 52 |
| 7 | Obtained errors and quench loads for the selected best and worst simulations in the set of conducted simulations. | 55 |
| 8 | Summary of the best fitting parameter values for the IPD magnets with respect to the quench load error. | 59 |
| 9 | Summary of some properties of the LHC 600 A circuits and their protection [1, 21]. Magnets marked with the same upper indice number are nested into each other. Magnets marked with * include nested magnets, not listed in the LHC 600 A circuits. | 63 |
| 10 | Quench-back prediction results for the different 600 A circuit types, including further information about the discharge and circuits [1]. | 66 |
| 11 | RB event - Original quench and all secondary quenches, showing the time of quench t_q and current at the moment of the quench I_q . RB.A78 circuit, 28.03.2021-22h09. | 80 |
| 12 | Simulation options for the co-operative simulations, including time stepping and convergence tolerances | 84 |
| 13 | Summary of discharge characteristics of the different quench simulations | 91 |
| 14 | Superconducting materials and their properties | 105 |
| 15 | Characteristics of strands, used in LHC magnets [1, 21] | 106 |
| 16 | Characteristics of multi-stranded cables in LHC magnets [1] | 106 |
| 17 | Characteristics of single-stranded cables, used in LHC magnets [1], guess values are indicated with (*) | 106 |
| 18 | Characteristics of LHC magnets [1, 11] | 107 |
| 19 | List of LHC circuits and their specifications [1, 11] | 110 |

Listings

| | | |
|---|---|-----|
| 1 | Coding example to prepare parts of the parameter sweep for the IPD magnet MBRB (more detailed explanation in Chapter 3.3) | 111 |
| 2 | Coding example to prepare all of the 600 A quench-back simulations . | 119 |
| 3 | Coding example to prepare the MCBYH quench location simulations | 122 |

1 Introduction

The Large Hadron Collider (LHC) at the European Organization for Nuclear Research accelerates different particles to high-energies and brings them to collision, in order to search for the fundamentals of these particles. This is largely made possible by superconducting magnets which keep the particle beams on their trajectory and allow the bending of the beamline [1].

Simulations of the complex electrical, magnetic and thermal transients in these magnets and their circuits are thus crucial for analyzing their behavior and to assess the impact of different failures that might occur. At CERN, these simulations can be for example performed with the STEAM framework [2] which was developed in the Section Performance Assessment and Electrical Quality Assurance (TE-MPE-PE). This framework includes a library of multi-physics models for the superconducting magnets, which is for example used to simulate on-demand events occurring in the magnets, test scenarios or potential failure cases. However, these models need to be validated in order to ensure their reliability. This validation includes, among other things, the determination of unknown model parameters by validating the simulation results to measurements from operation. So far, this was a relatively laborious and tedious process as it requires the execution of a huge number of simulations.

The goal of this thesis is thus, to provide a solution that expands the existing STEAM framework with the possibility to automatically generate models of superconducting magnets and to validate them against transients, measured in these LHC magnets. Furthermore, it should also open up the way for the prediction of for example occurring events or physical phenomena in the magnets.

The thesis is thus structured as follows:

- Chapter 1 describes the general fundamentals about CERN and superconductivity as well as superconducting magnets
- Chapter 2 explains the modelling approach of superconducting magnets, as used in the STEAM framework and this thesis.
- Chapter 3 shows the application of the newly developed solution, by conducting an automatic generation and validation of two different use cases
- Chapter 4 gives further examples on the possible usage, for example the prediction of physical phenomena, occurring in the superconducting magnets, by conducting automated simulations with different assumptions
- Chapter 5 then discusses the possibility to use the new solution and framework to be applied on the modelling and simulation of events in the main bending dipoles in the LHC during operation
- Chapter 6 finally concludes and discusses the implemented solution. Furthermore, it gives an outlook and proposes improving future work

1.1 European Organization for Nuclear Research

The European Organization for Nuclear Research or often called CERN (derived from the French "Conseil européen pour la recherche nucléaire") is Europe's largest physics laboratory [3] focusing on research in particle physics and high-energy physics. Situated on the Franco-Swiss border near Geneva, it was founded in 1951 by 11 member states with the goal to unite European scientists in their endeavours. In the following years, CERN quickly grew and is now hosting a huge variety of experiments and particle accelerator facilities, including since 2008 the world's largest particle collider, the Large Hadron Collider [3].

In the years of operation, CERN achieved some major break-throughs in particle- and high-energy physics, for example, the discoveries of the W and Z bosons in 1983 as well as the Higgs Boson in 2012, the discoveries of new fundamental physical effects and interactions, for example, the discovery of neutral currents in 1973 and direct CP violation in 1999, but also largely contributed to the engineering domain, for example by being the birthplace of the World Wide Web [3].

1.1.1 Large Hadron Collider

CERN's main accelerator complex is focused around the Large Hadron Collider (LHC) that started its operation in 2008. The LHC is a 27 km long ring of superconducting magnets along with supporting accelerating structures designed to boost different particles to a maximum energy of about 7 TeV, resulting in a collision energy of about 14 TeV [4]. These high energies are reached by a chain of accelerators with increasingly higher energies accelerating bunches of particles in different beam pipes. After injection into the LHC, these bunches are brought to collision within one of the four large detectors - CMS, ATLAS, ALICE and LHCb [5]. These detectors consist of a variety of smaller detectors, which aim to measure the physical properties of the collision debris in order to gain new insights into the physics of the sub-atomic and quantum particles. The chain of accelerators, the various used particles and the included experiments and detectors are illustrated in Figure 1.1.

A more detailed overview of the superconducting circuits and magnets installed in the LHC will be given in Chapter 1.3.

The LHC is currently being maintained and upgraded in the Long Shutdown 2 and will restart its operation in Spring 2022. It is then planned to operate for a further 3 years before 2025 the Long Shutdown 3 will start. In this maintenance period, the whole accelerator chain and ring will be upgraded for the High-Luminosity-LHC (HL-LHC) project, which is expected to drastically increase the luminosity, namely the number and quality of collisions [7].

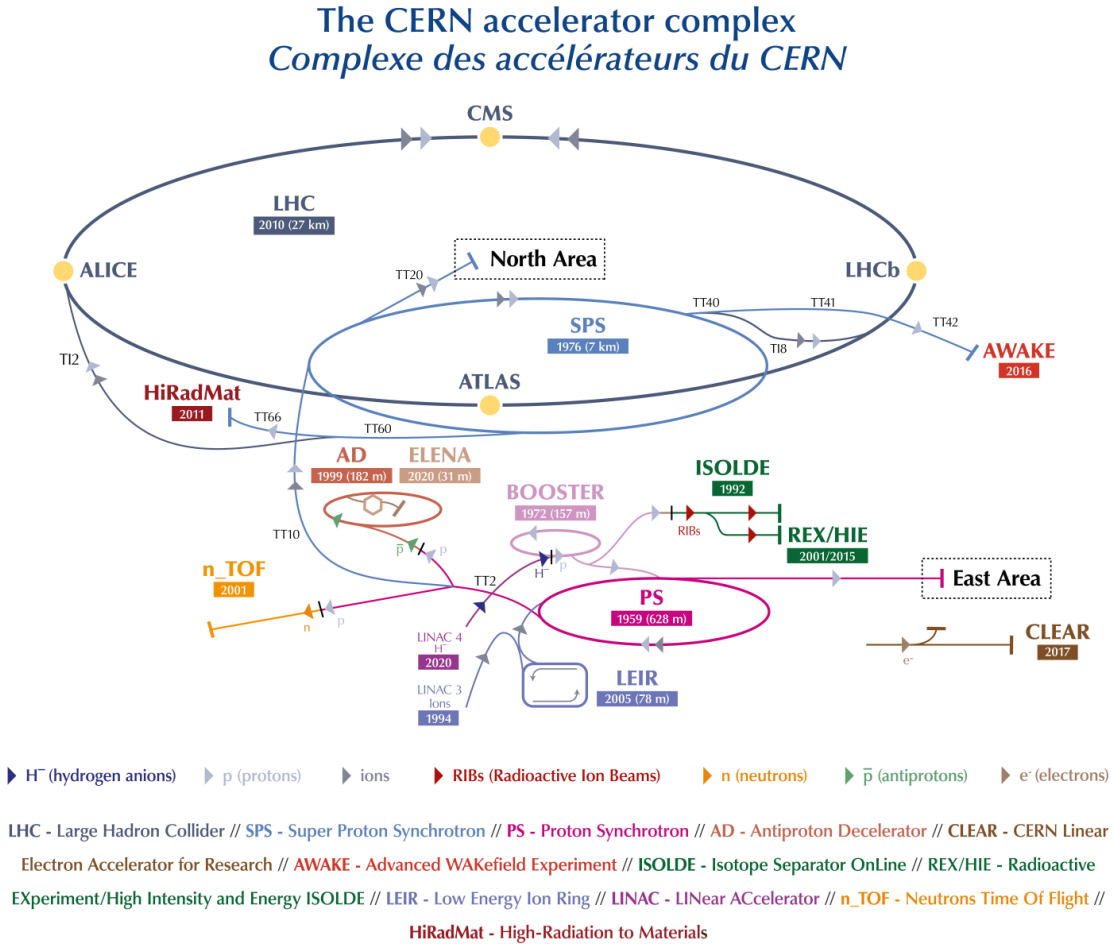


Figure 1.1: CERN's accelerator complex, illustrating the chain of particle accelerators, used particles and the different included experiments and detectors [6]

1.1.2 CERN Magnet Test Facility - SM18

Given the complex nature of the accelerator systems and their magnets at CERN, a magnet test facility, also referred to as SM18, was established. This facility provides the opportunity to test any of the magnets used at CERN, prior to their insertion into the machine, in realistic conditions, especially at their operating cryogenic temperature and current level. Before the start of the LHC in 2008 for example, every of the main bending dipoles and main quadrupoles were tested, trained and measured before their final installation.

Additionally to tests of magnets prior to their final installation, the facility is also supporting the development of future prototype magnets and transmission systems. For this reason, the facility consists of a variety of horizontal and vertical test benches,

which can deliver a maximum current of up to 30 kA, cryogenic temperatures between 1.9 and 80 K and can host different sized magnets up to 4 m (for the vertical test benches) and 15 m (horizontal benches) [8].

1.2 Superconductivity and Superconducting magnets

Superconductivity is a physical phenomenon causing certain materials under certain conditions to not show any electrical resistance and to expel the interior magnetic flux.

The state of superconductivity was first discovered by Heike Kammerling Onnes in 1911 while he was studying the electrical resistance of mercury wires at very low temperatures. At a temperature of 4.2 K, a sudden transition took place in which the electrical resistance in his experiment dropped to zero [9]. This temperature is nowadays called the critical temperate T_C [K], below which the material exhibits the properties of superconductivity. Furthermore, besides an absolutely zero electrical resistance, Walther Meissner and Robert Ochsenfeld discovered in 1933 the second governing property of superconductivity, i.e. the expulsion of a magnetic field from the inside of the superconductor, also called the Meissner effect. This effect was described in 1935 within the London equations, stated by Fritz and Heinz London. These equations include the London penetration depth λ [m] that is governing the exponential decay of the magnetic field from the outside of a superconductor towards its interior [9]. Following this first physical and mathematical description of superconductivity, the first microscopic quantum theory was proposed in 1957 by John Bardeen, Leon Cooper and John Robert Schrieffer, known as the BCS theory. This theory is still the most widely accepted explanation for superconductivity, even though, since the discovery of high-temperature superconductors in 1986, it is believed that other still not fully understood effects are involved [10].

Following the discovery of the Meissner effect, it was also discovered that the state of superconductivity can be not only lost by increasing the temperature but also by increasing the applied field to the superconductor. The value of the field at which this state is lost is named the critical field B_C [T].

Superconductors can be roughly split into two different categories: type-I and type-II superconductors.

Type-I superconductors show perfect diamagnetism, with a magnetic susceptibility of $\chi = 1$, meaning that the material shows a perfect magnetization opposing the direction of the applied field [11]. These superconductors are usually pure metals. Once the critical field or temperature is reached, the state of superconductivity abruptly breaks down.

Type-II superconductors, usually made of metal alloys or ceramics, show an intermediate phase in the transition between superconducting and normal state in which the properties are mixed. These materials include impurities that remain as normal conducting zones. Once the lower critical field of type-II superconductors B_{c1} [T]

is reached, these zones are functioning as pinning centers, that allow some of the magnetic flux to pass through and thus keep the material in superconducting state. Once the upper critical field B_{c2} [T] is reached, also type-II superconductors transition into normal state. The graph of the different phases for both superconductor types, dependent on the temperature and field, is shown in Figure 1.2. Because of this additional transition phase, type-II superconductors can reach much higher fields [12].

In the case of type-II superconductors, this has to be extended even further by a

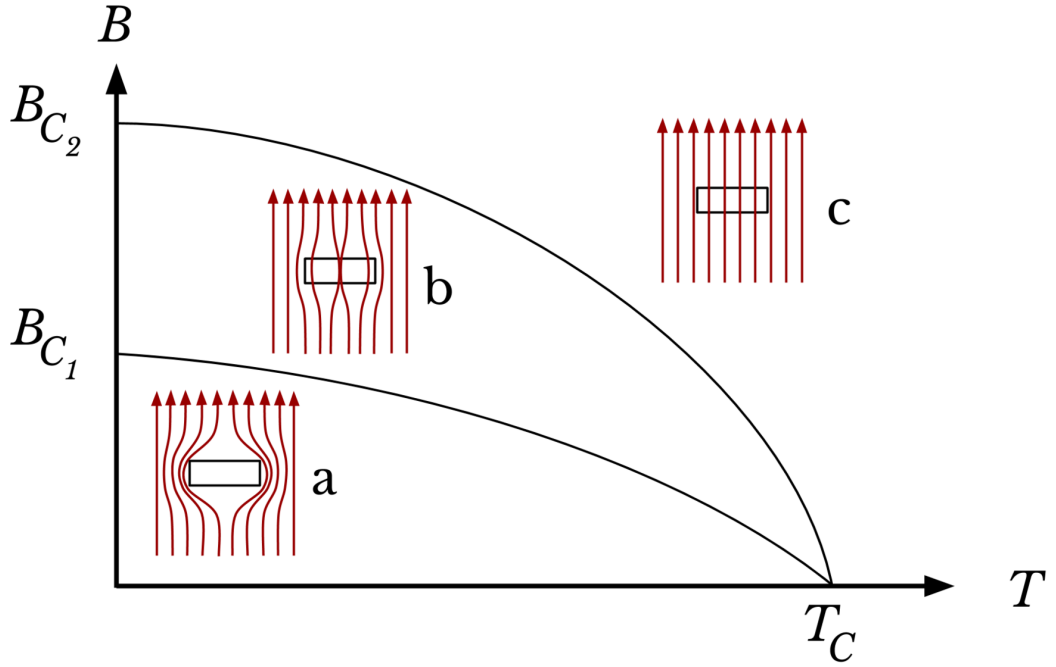


Figure 1.2: Magnetic field versus temperature, illustrating the expulsion of the magnetic field in the case of: a) superconducting state with $B < B_{c1}$ (or $B < B_c$ for type-I superconductors), b) the intermediate phase of type-II superconductors with $B_{c1} < B < B_{c2}$ and c) the normal state with $B > B_{c2}$ [13]

dependence on the current density J [$\frac{A}{m^2}$] in the superconductor. The pinning centers in the material exert a specific force holding the magnetic flux, called pinning force, which is opposing the Lorentz force of the applied field and current. If the Lorentz force exceeds this pinning force, the material will as well transition into the normal phase. Thus, in type-II superconductors, the state of superconductivity is dependent on a relation of $J-B-T$, also called critical surface [12]. An example of a critical surface for a commonly used superconductor, Niobium–titanium (Nb-Ti), is shown in Figure 1.3.

In Table 14 in the Annex, a general overview of some of the most used and re-

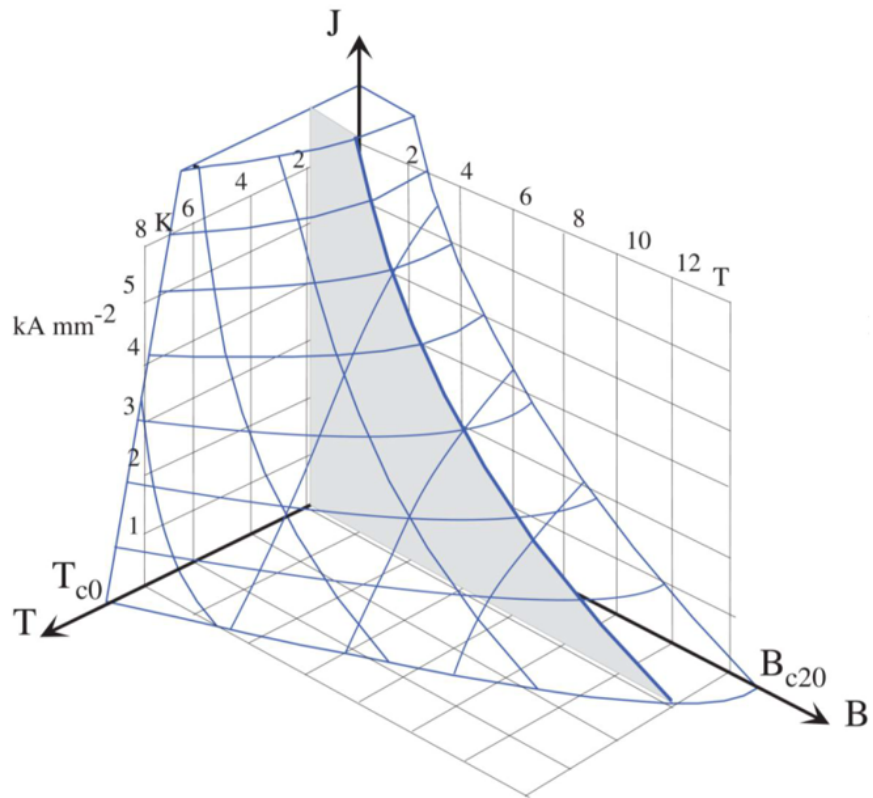


Figure 1.3: Critical surface of Nb-Ti, showing the J - B - T cross-section on a typical operational temperature of 1.9 K in grey [14]

cently developed superconducting materials and their characteristic properties is given. Also, some examples of high-temperature superconductors are given, those critical temperature is above the boiling temperature of liquid nitrogen (77 K) [10].

1.2.1 Superconducting cable

In the development of superconducting magnets, the design and manufacturing of the superconducting cables are the main challenges achieving large stability, good field quality and little transitory losses. As shown in Figure 1.3, the superconductive state depends on the J - B - T critical surface, where B and T are material intrinsic properties, while J is largely dependent on the operating conditions and the manufacturing of the cable [12]. Furthermore, because of the high currents, the superconducting cable has to bear the resulting strong mechanical forces and stresses [15]. In the scope of this thesis, only one of the most commonly used cable types is described the Rutherford cable.

In these, the superconducting material is usually arranged as filaments with a diameter of about a few micrometers. This is done in order to avoid flux jumps (mag-

netization losses in a superconductor bulk) in the impure material and to decrease the heat generated by eddy currents, occurring in the cable in the case of a changing field [16]. Moreover, the arrangement in filaments also reduces persistent currents, which cause large magnetic-field errors and hysteretic loss. In order to further reduce transient losses, these filaments are twisted by a specific length called the filament twist pitch l_f [m], which avoids the generation of large current loops [14]. The filaments are then embedded in a so-called stabilizer matrix, usually made of a low electrical-resistivity material like copper. In the case of a transition of some parts of the superconductor to normal state, these filaments show a very high normal state resistivity [15]. Thus in these cases, the stabilizer matrix is used to carry the current, drastically reducing the generated heat. This is further explained and illustrated in Chapter 1.2.2. Two examples of wires, composed of filaments in a stabilizer matrix are shown in Figure 1.4. In order to furthermore reduce the transitory losses and avoid flux jumps, these wires, then called strands, are often bundled and twisted together into multi-stranded cables [14]. The twist length of the strands is described with the strand-twist pitch length l_s [m]. One example for such a multi-stranded Rutherford cable is shown in Figure 1.5.

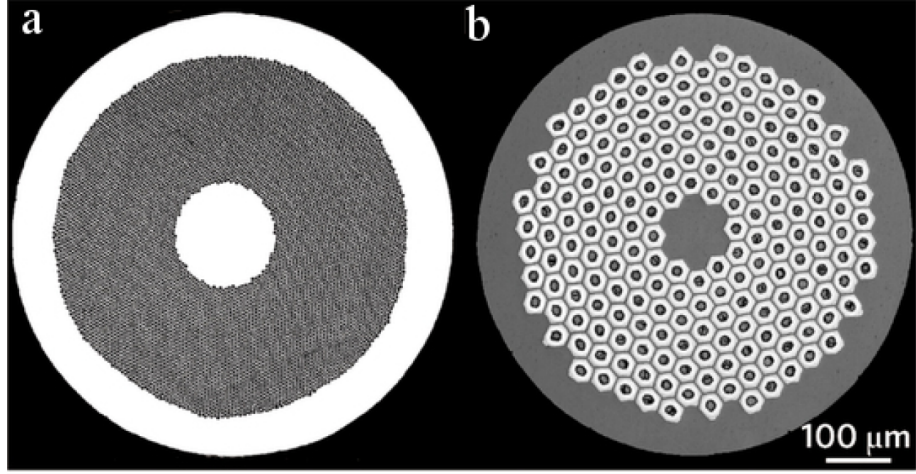


Figure 1.4: Wires made of a) Nb-Ti filaments and b) Nb₃Sn filaments, both embedded in a copper stabilizer matrix [17]

1.2.2 Quench

Superconducting materials can sometimes experience a phenomenon, called quench, which involves the sudden transition of parts of the material into the normal state. These spots of the superconducting material in a strand, which transferred into the normal zone, increase the resistance of the superconductor filaments. Hence, the

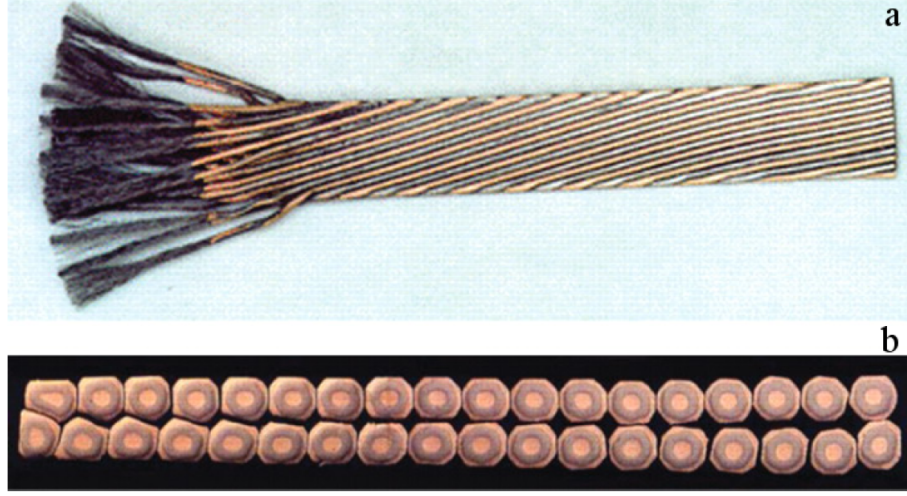


Figure 1.5: a) Top-view and b) cross-section of a typical Nb-Ti Rutherford cable that is used in the LHC main dipole bending magnets [18]

current redistributes inside the strands and the stabilizer matrix, usually made of copper, starts to carry the current. This is called the current sharing regime and is reached at the current sharing temperature T_{cs} [K]. The temperature in the spot increases and takes the superconducting cable above the critical conditions of the material, resulting in a quenched spot, also called the quench hot-spot.

In the case that the generated heat by the normal zone is smaller than the heat evacuation of the cooling system, the cable can recover the quench and returns to the superconducting state. In the case the generated heat can not be compensated by the cooling, a thermal runaway starts [19]. Figure 1.6 shows the qualitative temperature evolution of a superconducting cable just above and below the stability energy margin, causing either a thermal runaway or thermal recovery.

The heat is further propagating with a velocity, also referred to as quench propagation velocity v_q [$\frac{m}{s}$], throughout the cable and insulations, causing eventually the whole magnet to quench [12]. This principle is illustrated in Figure 1.7, showing the temperature and quench evolution as well as the current path in the superconductor (Sc) and the stabilizing copper matrix (Cu) around a quench hot-spot. Under adiabatic assumptions, the local thermal balance of a copper stabilized wire follows the equation [20]:

$$\frac{\rho_{Cu}(T, B)j_{Cu}^2}{f_{Cu}}dt = C_p(T)dT \quad (1.1)$$

where f_{Cu} [-] is the volumetric fraction of copper in the wire, ρ_{Cu} [Ωm] the resistivity of copper, j [$\frac{A}{m^2}$] the current density in the copper, T [K] the temperature and B [T] the field strength of the conductor, dt [s] the time derivative and C_p [$\frac{J}{Km^3}$] the volumetric specific heat of the conductor. The remaining resistance of the superconducting wire at low temperatures is often described using the Residual Resistivity

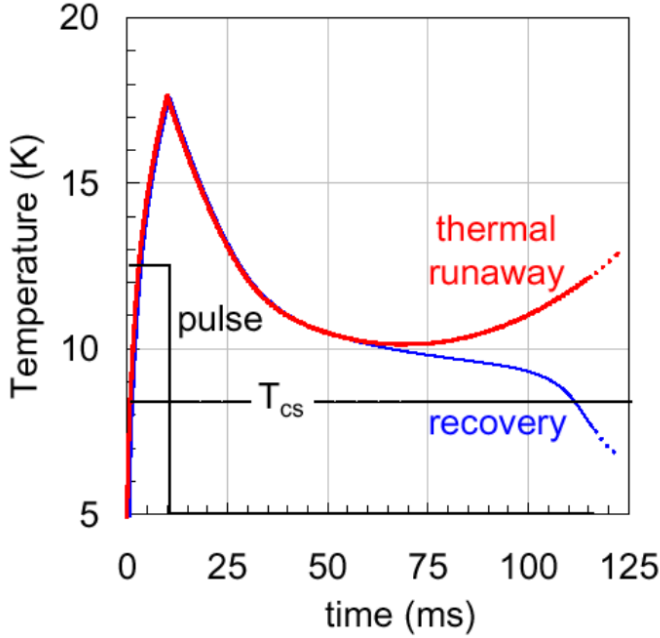


Figure 1.6: Qualitative temperature evolution in a quench hot-spot just below and above the stability energy margin, that lead to either a thermal runaway or recovery [19]

Ratio (RRR), which describes the ratio of the resistivity at cryogenic (e.g. 4 K) and at room temperature (e.g. 300 K) [15]. For commonly used superconducting wires using Nb-Ti this ratio is between 50-300 [1, 11, 21]. Sometimes, the RRR for some magnet cables was not measured and thus is not known for modelling. Hence, it is effectively used as a fitting parameter for the models within a physical range.

A series of energy inputs of very different natures, timescales, and magnitudes can cause a quench. These range from perturbations caused by wire or conductor motions, to flux jumps to AC losses or heat leaks. In the design of a superconducting cable, these causes have to be considered and the superconducting cable and the cooling system need to show certain stability towards perturbations [19]. Furthermore, usually superconducting cables rarely reach the critical current estimated from tests and measurements on short samples of the respective cables or materials. During the first tests, they often quench at current levels of 70 - 90% of the estimated values. This current level usually increases with the number of performed tests and quenches and is called the training of a superconducting magnet [22]. Even though the mechanisms causing the improved performance of superconducting magnets after training are not fully understood yet, it is expected to have mechanical reasons. Due to the strong forces exhibited by a quench in the magnet, the conductors and cables are pushed into more stable positions and thus withstanding higher current densities [19].

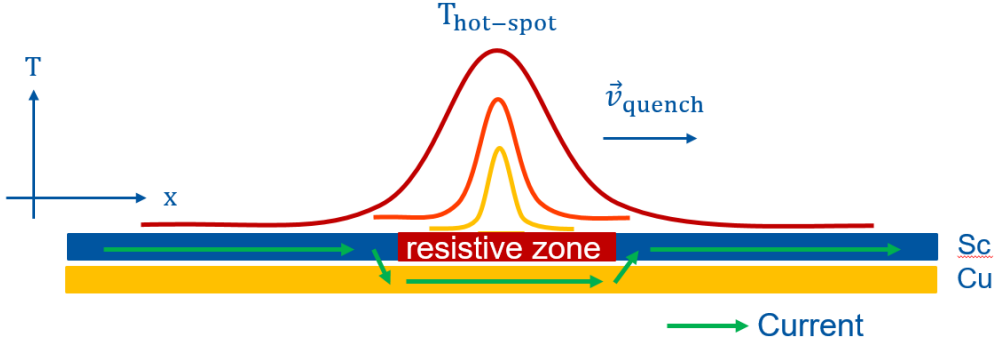


Figure 1.7: Illustration of the heat evolution and current redistribution around a quench hot-spot [12]

1.2.3 Coupling currents

The cables of superconducting magnets are often subject to magnetic field change, induced for example by a current decay in the magnets conductors due to a fast power abort in the magnets circuit. If the cables are exposed to a changing magnetic field, various currents are induced within them, following Lenz's Law, generating an induced field opposing the changes in the initial magnetic field. These currents can flow within the strands, between the filaments, also known as the Inter-Filament Coupling Currents (IFCC), but can also flow between the various strands of a cable, known as Inter-Strand Coupling Currents (ISCC) [23]. The total, local magnetic field change $\frac{dB_t}{dt}$ [$\frac{T}{s}$] thus results to [16]:

$$\frac{dB_t}{dt} = \frac{dB_a}{dt} + \frac{dB_{if}}{dt} + \frac{dB_{is}}{dt} \quad (1.2)$$

with $\frac{dB_a}{dt}$ [$\frac{T}{s}$] the applied magnetic field and the opposing magnetic field change $\frac{dB_{if}}{dt}$ and $\frac{dB_{is}}{dt}$ [$\frac{T}{s}$] generated by the inter-filament and inter-strand coupling currents, respectively. The magnitude of these coupling currents are proportional to increasing square of the filament or strand twist pitch, respectively, and to decreasing resistivity of the matrix material (IFCC) or strand contact resistance (ISCC) [23].

The rise of these coupling currents is described by the time constants τ_{if} [s] and τ_{is} [s], respectively. These typically range between 0.01 to 0.1 s for IFCC and 0.01 s to 10 s for ISCC. For the calculation of these time constants, the literature proposes [15,

23]:

$$\tau_{\text{if}} = \frac{\mu_0}{2} \left(\frac{l_f}{2\pi} \right)^2 \frac{1}{\rho_{\text{eff}}} \quad (1.3)$$

$$\tau_{\text{is}} = \frac{\mu_0}{\pi} \left[\ln \left(\frac{w}{h} \right) + \frac{3}{2} \right] \frac{h}{w} \beta_{\text{is}} \quad (1.4)$$

$$\beta_{\text{is}} = \frac{1}{120} \frac{l_s}{R_C} N_S (N_S - 1) \frac{w}{h} \quad (1.5)$$

$$\rho_{\text{eff}} = \rho_m f_{\rho,\text{eff}} \quad (1.6)$$

with $\mu_0 = 4\pi 10^{-7}$ TmA⁻¹ the magnetic permeability of vacuum, ρ_{eff} [Ωm] the effective transversive resistivity of the filament region, taking the magneto-resistivity and RRR into account, ρ_m [Ωm] the electrical resistance of the matrix material, $f_{\rho,\text{eff}}$ [-] scaling factor for the effective transversive resistivity, h and w [m] height and width of the cable, respectively, N_S [-] the number of strands and R_C [Ω] the cross-contact resistance.

The two parameter $f_{\rho,\text{eff}}$ and R_C are difficult to determine, as they depend on various complex phenomena. $f_{\rho,\text{eff}}$ depends for example on the interface resistance between the different filaments in a strand as well as on the position and distribution of the filaments within the cross-section of the strand. Typical values for $f_{\rho,\text{eff}}$ range between 1 and 3. The strand contact resistance R_C depends on various, difficult to determine factors, such as the level of oxidation of the bare strands (e.g. due to fabrication), the contact area between the strands or the pressure transversely applied on the cable. Typical values range between 10^{-4} and 10^{-6} Ω [23]. Usually, it is assumed, that these parameters are uniform along a strand and cable.

The flow of these currents through the wire and cable matrix leads to respective transient losses, that can heat up parts of the wire and might even lead to a quench [24]. The losses caused by the coupling currents are called Inter-Filament-Coupling-Losses (IFCL) and Inter-Strand-Coupling Losses (ISCL). The resulting power per conductor volume P_{if}''' [Wm⁻³], generated by IFCC can be described with [15, 23, 25]:

$$P_{\text{if}}''' = \left(\frac{l_f}{2\pi} \right)^2 \frac{1}{\rho_{\text{eff}}} \left(\frac{dB_t}{dt} \right)^2 \quad (1.7)$$

and the power per conductor volume P_{is}''' [Wm⁻³], generated by ISCC [15, 23, 25]:

$$P_{\text{is}}''' = \frac{2}{\mu_0} \tau_{\text{is}} \left(\frac{dB_{t,\perp}}{dt} \right)^2 \quad (1.8)$$

with $\frac{dB_{t,\perp}}{dt}$ the component of the total net field change, perpendicular to the cable broad face. There are also other types of ISCL, which are usually not considered as their amplitude is much lower.

1.2.4 Quench protection systems

Superconducting magnets usually operate at high current levels and have relatively large inductances. Thus, the magnetically stored energy in the magnet circuits is very high and in case of failure can cause serious damage to the magnets and supporting machines. For example, the main bending dipoles in the LHC are used in a chain of 154 magnets, operating at a current level of 11 kA. The stored energy can be approximated as [22]

$$E = \frac{n \cdot L \cdot I^2}{2} = \frac{154 \cdot 0.1 \text{ H} \cdot (11 \text{ kA})^2}{2} \approx 0.85 \text{ GJ} \quad (1.9)$$

with n [-] the number of magnets in the circuit, L [H] the nominal inductance of a single magnet and I [A] the operating current level. If this energy is discharged as Joule heating in the magnets coil, it can cause high hot-spot temperatures. If the acceptable ranges, for most superconducting magnets usually up to 300 K [11, 14], are exceeded too often, it can lead to the melt-down of insulations and conductor material and thus introduce for example short circuits. Furthermore, the resistive zones in the conductor can introduce large internal voltages. Therefore, it is very important to dissipate the stored energy in a fast and efficient way. Quench protection systems (QPS) can be classified into four groups, separated into two categories. The classification of quench protection systems and some frequently used examples are shown in Table 1 [16].

First, one can distinguish between active and passive protection systems. Active systems need to be activated by a quench detection system (QDS) or other interlock systems. These could be for example simple voltage taps, which monitor the voltage across specific parts of the magnets coil. If a quench occurs, the voltage across this resistive part rises and can be measured. Passive quench protection systems on the other hand do not need to be activated or are activated by their intrinsic properties. These are for example by-pass cold-diodes, that open and carry the current, once the resistive voltage of the magnet becomes larger than their threshold voltage.

A second classification can be made upon the way the QPS ensures protection. This can be done either by utilizing the internal, resistive behavior of the magnet, e.g. dissipating the energy as heat inside the magnets coils or by dissipating the energy externally, for example in a dump resistor.

Some QPS are described in more detail in the following paragraphs.

By-pass elements

By-pass elements are electric components connected in parallel to the magnet and start carrying the current in case the resistance in the quenching magnet becomes too large. The quenching magnet is thus protected, as the current bypasses through the parallel element. The most commonly used by-pass element are protection diodes, which carry most of the current once their threshold voltage across the magnet is reached.

Table 1: Classification of quench protection systems and some frequently used examples

| | Passive | Active |
|---------------------------|---|---|
| Internal discharge | Self-protection | Quench heater (QH), Coupling loss induced quench (CLIQ) |
| External discharge | By-pass elements, coupled secondary coils | Energy extraction (EE) |

Energy extraction (EE)

Energy extraction systems utilize an external dump resistor to dissipate the stored energy in the circuit. In the event of a discharge, switches in the circuit are opened in order to force the current through these resistors. The energy extraction resistance is then heating up and dissipating the energy. The time constant τ_{EE} for the discharge is thus:

$$\tau_{EE} = \frac{L_{\text{circ}}}{R_{EE}} \quad (1.10)$$

where R_{EE} [Ω] is the energy extraction resistance and L_{circ} [H] the total inductance of the magnets circuit. In order to dissipate the energy as quickly and efficiently as possible, one would like to choose the EE resistance as high as possible. On the other hand, during a discharge, the EE system and the magnet form a closed loop. The maximal voltage across the EE is thus defined by the maximal voltage across the magnet (or chain of magnets). In the case of the main de-/focussing quadrupoles in the LHC, the EE resistance was chosen to be $R_{EE} = 6.6$ m Ω and $L_{\text{Circ}} = 0.265$ H, resulting in a time constant of about $\tau_{EE} \approx 40$ s [1, 26, 27].

Quench heaters (QH)

Quench heaters are strips made of stainless steel that are attached to parts of the magnet coil. In the case of a detected quench, a capacitor is discharged into these strips which quickly heat up due to Joule heating. This heat is then diffusing through the insulation of the strips and coil, heating up the adjacent turns of the magnet coil. These turns are thus brought above their critical surface and quench. As the quench is propagating with v_q it is sufficient to only heat up parts of the coil turns. Therefore, the stainless steel strips are partially covered by copper, such that only a specific number of heated sections remain. These are called heating stations and considerably reduce the required voltage that needs to be applied to the strips to obtain the required temperatures. In the LHC the quench heaters are powered by a capacitor bank with a capacitance of 7.05 mF and an operating voltage of 900 V [28]. An example of a quench heater strip attached to a magnet coil can be seen in Figure 1.8. In the shown case, the quench heater strip is glued to different turns of the magnet coil in order to heat up and quench more turns, considerably decreasing the

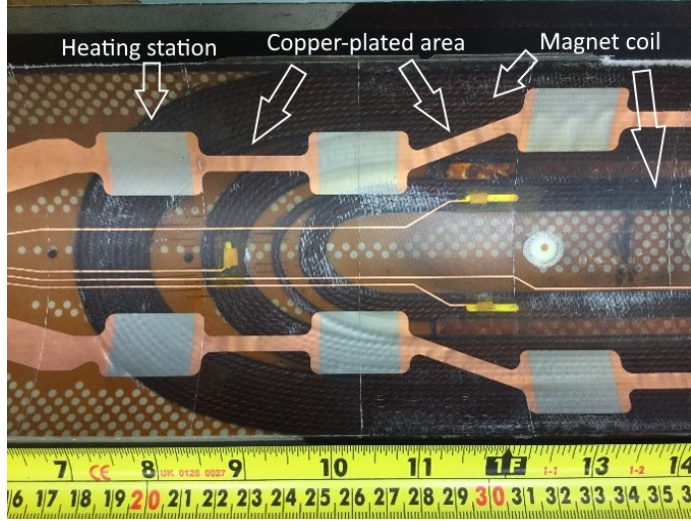


Figure 1.8: Quench heater strips attached to parts of an insulated coil of a short MQXF magnet model, showing heating stations and copper-plated areas [26]

required time to dissipate the energy.

Coupling loss induced quench (CLIQ)

Coupling loss induced quench is a relatively new quench protection scheme that utilizes inter-filament- and inter-strand-coupling currents in the magnets conductors in order to quench these [16, 29]. CLIQ utilizes the resulting losses to quench the magnet conductors and thus to quickly increase the internal coil resistance. This is achieved by connecting a charged capacitor and thyristor to the coil. In the case of a quench, this capacitor is discharged into the magnets coil and thus leads to a few short oscillations in the magnet conductors current. The resulting fast and strong change of the magnetic field leads to the generation of the inter-filament- and inter-strand-coupling losses, which heat up the conductor and thus induce a quench internally in the wires.

1.3 LHC superconducting circuits

The LHC consists of a total number of about 9600 superconducting magnets with different purposes within the ring and all operating at a cryogenic temperature ranging between 1.9 K and 4.5 K [5]. Currently, all magnets in the LHC are made out of Nb-Ti and thus require such low temperatures.

The different magnets and their tasks range from the main bending dipoles to focusing and de-focusing as well as tuning quadrupoles, onto a large variety of correction sextupoles, octupoles and decapoles. In general, the magnets can be arranged

into seven groups, depending on their function and position in the ring. A general overview of the magnets, used in the LHC is given in Table 18 in the Annex.

In total, there are also seven different classes of circuits with again each subgroups, ranging in electrical complexity from an operating current level of 11.85 kA down to 60 A, a magnet chain of 154 magnets to single magnets, as well as protection systems, that range from self-protecting to complex combinations of methods. An overview of the different circuits and magnets that are used in the LHC is given in Table 19 and for the strands and cables in Tables 15 and 16, 17 .

Some of the LHC superconducting circuits and magnets will be described and analyzed within this thesis in more detail.

2 Modelling of superconducting magnets

Modelling superconducting magnets poses various challenges to the modelling and simulation framework. Different physical domains, as well as a series of time- and spatial scales are combined. Usually, such complex problems are tackled either with finite-element or finite-difference modelling. However, such approaches can require a high computational effort and thus can become inefficient in simulating the non-linear behavior in superconducting magnets, or can lack accuracy from not including sufficient features.

The STEAM (Simulation of Transient Effects in Accelerator Magnets) framework [2], which was developed at CERN in the past years, tries to tackle these challenges with a consistent approach, combining multiple frameworks and software.

One part of this framework is STEAM-LEDET (Lumped-Element Dynamic Electro-Thermal) [16, 24] that utilizes the concept of lumped element modelling with three coupled sub-networks of lumped elements, reproducing the electrical transient of a simplified version of the magnets main circuit, the thermal transients in the coil cross-section and the electro-magnetic and thermal effects of the transitory losses. It was shown that this approach can simulate the occurring transients in the magnets with high accuracy, while greatly reducing the computational time with respect to finite-element models [16, 24]. STEAM-LEDET and the concept of lumped element modelling will be described in more detail in Chapter 2.1 ff.

Furthermore, the electro-magnetic thermal model from STEAM-LEDET can be combined with other simulation tools, more specialized on other physical domains or phenomena in a so-called co-operative simulation. Within the STEAM framework, this is handled by STEAM-COSIM, which ensures a consistent signal exchange between the simulations tools, taking possibly different temporal or spatial scales into account [30, 31, 32]. STEAM-COSIM and its application within the scope of this thesis will be described more explicit in Chapter 2.6.

2.1 Lumped element modelling

In order to describe and simulate complex systems, it is common practice to break down these systems into smaller, less complex chunks. In lumped element modelling these are small discrete chunks with each only having a small number of inputs and outputs. To each of these small, discrete chunks, one can then apply algebraic, numerical or conceptual abstractions that describe or approximate the behavior of the chunk on a more aggregate level. Lumped element modelling utilizes this concept by combining various systems and treating them under a set of assumptions as a single entity. The state-space model of the complex system, meaning the partial differential equations of the continuous-time domain as well as the space model, is thus transformed into a set of ordinary differential equations with a finite number of parameters [33]. A very simple example of a lumped element in electronics is a

resistor, where the interaction and behavior of a huge number of atoms are usually combined into a single current-voltage relationship. The concept of lumped elements can not only be applied to electronics but to nearly every physical problem such as thermodynamics or mechanical multi-body systems. Lumped-element modelling always remains an approximation of the real, physical system, while the level of approximation can be defined by the level of used discrete chunks. If the lumped element model or mesh is too coarse to precisely describe the behavior, it can be broken down into even smaller elements until the behavior of interest is satisfactorily captured. A similar concept is also used in finite-element modelling.

A big advantage of lumped-element modelling is, that it is able to combine the interaction and mutual influences of different physical domains by coupling the lumped elements together. In the context of STEAM-LEDET, this is achieved by coupling the sub-networks of the three physical domains, electro-magnetic, thermal and transitory coupling, together. In Figure 2.1 the energy exchange and coupling between these sub-networks is illustrated.

Elements corresponding to one sub-network are illustrated in Figure 2.1 as either yellow (electrical), red (thermal) or blue (coupling), while elements belonging to two networks are shown as orange (electrical-thermal), green (electrical-coupling) and purple (coupling-thermal) [24]. Each of these sub-networks will be described in more detail in the following chapter and parameters that are of special interest for the validation of the superconducting magnet model will be specifically pointed out.

In the version of STEAM-LEDET that was used for the validation of the models in this thesis, LEDET only takes a cross-sectional 2D model into account. In some cases, this 2D model is extended to include an additional longitudinal component, which simulates the quench propagation into the direction perpendicular to the cross-section and thus scales the electrical resistance of the respective turns. This will be described in more detail in Chapter 2.5.

The resulting differential equations from the coupled lumped element model are solved using the finite difference method with an explicit Euler implementation.

2.2 Thermal modelling of superconducting magnets

2.2.1 Thermal lumped element sub-network

Following the approach of lumped elements, the thermal heat transfer within the 2D cross-section of the magnet is approximated using the finite difference method on the thermal balance problem of each independent half-turn. Each turn consists of two half-turns, one for each current direction (e.g. one half-turn for go- and return line). The thermal diffusion equation is only solved in the direction perpendicular to the transport current. The computationally expensive longitudinal thermal gradient is neglected.

In LEDET each coil half-turn is seen as a thermal element and their thermal balance

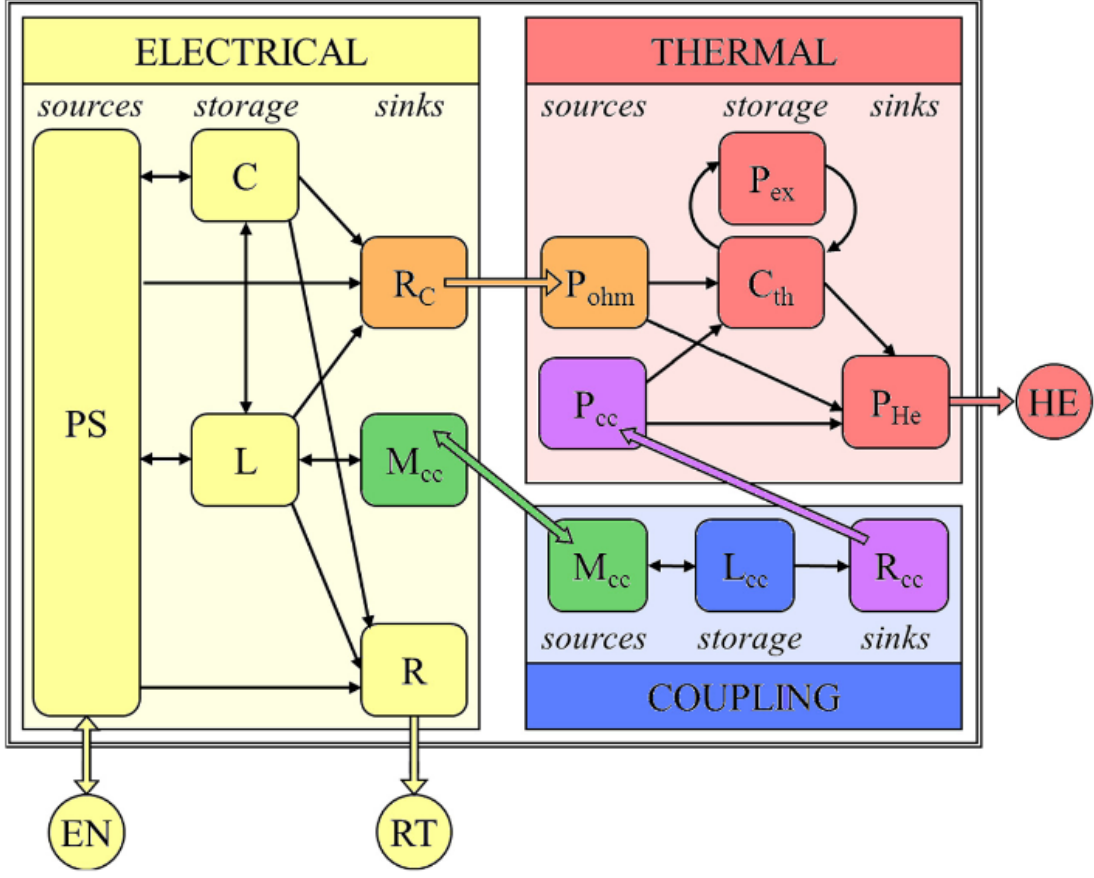


Figure 2.1: Representation of the three coupled sub-networks, used in STEAM-LEDET [16, 24]

equation reads [11, 24]:

$$P_{\text{if}} + P_{\text{is}} + P_{\text{Ohm}} + P_{\text{ex}} + P_{\text{Th}} = \bar{c}(T) \frac{dT}{dt} \quad (2.1)$$

where P_{if} and P_{is} [W] are the powers generated by inter-filament- and inter-strand-coupling losses [24, 21], P_{Ohm} [W] is the power generated by ohmic loss in the conductor, P_{ex} [W] the heat exchanged with other elements, P_{Th} [W] the heat transferred into a thermal sink, \bar{c} [JK⁻¹] the heat capacity of the element, averaged over its cross-section and T [K] its temperature. Each of the used thermal elements includes superconductor, stabilizer and insulation materials and all physical properties are assumed to be uniform within an element.

Following Equation 2.1, thermal energy is only introduced in two ways into the system, either via ohmic loss or via coupling loss in a conductor. The thermal energy is then exchanged between the coil turns or can be transferred to the thermal sink, i.e.

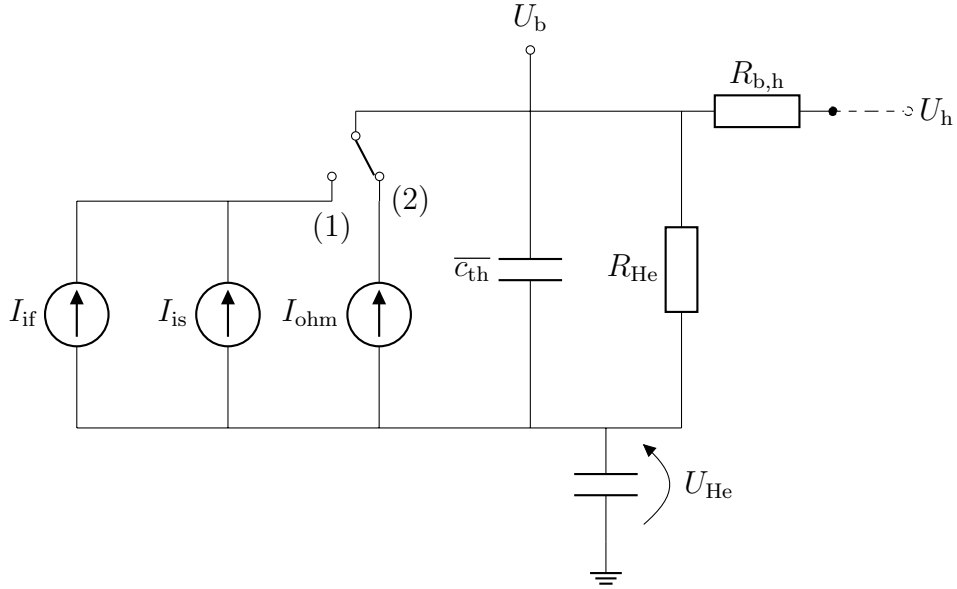


Figure 2.2: Example of an equivalent lumped-element model of an thermal element b and the transition to one neighboring thermal element h, used in earlier versions of LEDET

either the helium bath or other structural components of the magnet. An equivalent lumped-element sub-network, utilizing the equivalence in the electrical domain, for one thermal element is shown in Figure 2.2. Voltages U_b and U_h correspond to the temperatures of the thermal elements b, h, R_{He} and U_{He} to temperature and thermal resistance of the helium bath and the current sources I_{if} , I_{is} , I_{ohm} to the generated powers. Depending on the current state of the conductor, either in superconducting state only energy from coupling currents (1) or in normal state from ohmic loss (2) can be introduced to the system. However, this can be altered with different options in the model. Additionally heat can be exchanged with the neighboring element through a series of thermal resistances $R_{b,h}$ and is shown in Figure 2.1 as the corresponding power P_{ex} .

The coupling between the thermal and electro-magnetic models is twofold. First, the generation of ohmic loss due to Joule heating depends on the conductor current and follows [16, 24]:

$$P_{\text{Ohm}} = R_b(T_b, B_b, q_b) I_b^2 \quad (2.2)$$

where R_b [Ω] is the electric resistance of the thermal element and I_b [A] the current through the element. The second interaction between electro-magnetic and thermal model is in the dependency of the electric resistance R_b on B_b and T_b of the element as well as q_b [-], representing the current state of the conductor (superconducting

state: $q_b = 0$, normal state: $q_b = 1$). Furthermore, the changing resistance of a thermal element builds up a voltage across the conductor in the electric domain.

2.2.2 Helium cooling

Superconducting magnets so far usually require cooling to ensure the superconducting state of the conducting material. Magnets for the LHC and High Luminosity LHC, manufactured with low-temperature superconductors such as Nb-Ti ($T_c = 9.2$ K) or Nb₃Sn ($T_c = 18.1$ K), require even special cooling with helium, as their operational temperature is between 1.9 K (super-fluid helium) and 4.5 K (liquid helium), in order to keep some margin. Therefore, the magnets are usually kept in a helium bath, supplied by a constant flow [15].

Super-fluid helium, or also called helium II, describes a special phase of helium where it has a special set of characteristics. These properties include an almost perfect thermal conductivity and a frictionless flow if it flows with low velocity through tiny capillaries. As a result, due to the frictionless flow, the helium II can creep into the voids of cables and can conduct the heat from there, because of the very high thermal conductivity, without mass transport [11].

In order to improve the cooling of the magnets coils and conductors, sometimes the insulation of the cables is arranged such that they show a certain porosity and percolation to allow helium flow, while still preserving the mechanical resistance and dielectric strength [11]. As a result, the superconducting cables are not only cooled from their outside but also cooled from the inside by the helium, that crept through the insulation into the voids in between the strands. A simplified representation of a multi-stranded Rutherford cable and different quantities of helium II in the cables voids is shown in Figure 2.3.

In Figure 2.3 (a) all of the cable voids are filled with helium (blue background), in (b) about half of the voids are filled with helium, while the remaining parts are filled with insulation and in (c) all voids are only filled with insulation and there is no helium inside the cable cross-section [34]. Modelling this additional cooling is challenging, especially as the amount of helium inside the cable cross-section is not determinable. On the other hand, the additional cooling effect can be relevant, as the volumetric heat capacity of helium II is about 2000 times higher than the one of the conductors [11].

In LEDET, this additional effect can be taken into account, using two parameters $f_{\text{internal Voids}}$ and $f_{\text{external Voids}} [\%]$. The parameter $f_{\text{internal Voids}}$ defines the fraction of the cable cross-section, representing the inner voids in between the strands, while $f_{\text{external Voids}}$ defines the external voids between the strands and the outer insulation of the cable. Usually it is assumed that $f_{\text{internal Voids}}$ gives the fraction of cable cross-section filled by helium, while $f_{\text{external Voids}}$ defines the fraction of cable cross-section that is filled by Kapton insulation or epoxy impregnation [14]. Consequently, these parameters have to fulfil the following condition, forming the full cross-section of a

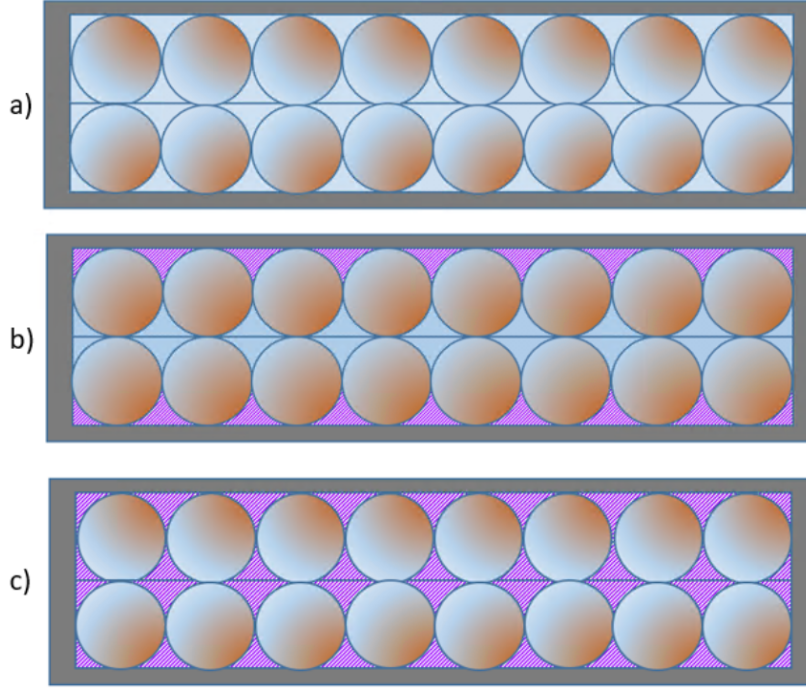


Figure 2.3: Simplified graphical representation of a multi-stranded cable, showing different quantities of super-fluid helium (blue) in the voids between the strands (orange) and their insulation (purple). (a) All voids are filled with helium, (b) half of the voids are filled with helium, remaining parts filled with insulation and (c) all voids are filled with insulation and no helium crepted into the cables voids [34]

cable as the sum of all fractions:

$$f_{\text{external Voids}} + f_{\text{internal Voids}} + f_{\text{Insulation}} + f_{\text{Strands}} = 1 \quad (2.3)$$

where $f_{\text{Insulation}} [\%]$ describes the fraction of cable insulation (grey area in Figure 2.3) and $f_{\text{Strands}} [\%]$ the fraction of cross-section, occupied by the bare strands.

As mentioned, the fraction of infiltrated helium II into the cable can not be feasibly measured. Nevertheless, a first, rough approximation of the amount of helium can be calculated. The area of the bare and insulated cable, assuming a rectangular shape, can be calculated following:

$$A_{\text{bare}} = w_{\text{bare}} \cdot h_{\text{bare}} \quad (2.4)$$

$$A_{\text{Ins}} = (w_{\text{bare}} + 2w_{\text{ins}}) \cdot (h_{\text{bare}} + 2h_{\text{ins}}) \quad (2.5)$$

where w_{bare} and w_{ins} [m] are the width of insulation and bare cable, respectively and h_{bare} and h_{ins} [m] the corresponding heights. The area in the cable that is occupied

by strands can be approximated, assuming perfectly round strands, by:

$$A_{\text{Strands}} = n_{\text{Strands}} \pi \frac{d_{\text{strands}}^2}{4} \quad (2.6)$$

where n_{Strands} [-] is the number of strands in the cable and d_{strands} [m] their diameter. The total ratio of voids inside the cable f_{voids} [-] is thus [27, 35]:

$$f_{\text{voids}} = \frac{A_{\text{bare}} - A_{\text{Strands}}}{A_{\text{Ins}}} \quad (2.7)$$

The fraction of helium in the voids then can be approximated, assuming all internal voids to be filled by helium, by:

$$f_{\text{internal Voids}} = \frac{(n_{s,l} - 1)(n_l - 1)}{n_{s,l}n_l} f_{\text{voids}} \quad (2.8)$$

where $n_{s,l}$ [-] represents the number of strands per layer and n_l [-] the number of layers in the cable.

The parameter of the helium fraction within the cable described with f_{He} [%], will be used as a fitting parameter within the range [0, f_{voids}] to account for the fact that the real amount of infiltrating helium is not known. The effect of varying the parameter will be shown in Chapter 3.3.2.

2.3 Electro-magnetic modelling of superconducting magnets

2.3.1 Electro-magnetic lumped element sub-network

The LEDET electrical lumped element model contains the conventional lumped elements, such as inductances, resistors or capacitors. Each electric element, usually representing either a pole of the magnet or a coil section, is composed of a self-inductance L [H], that is mutually coupled to the self-inductances of the other electrical components of the magnet and a resistor R , representing the electrical resistance of the element in the case, parts of the element transition into the normal state. The energy for the electrical model is provided by the power source (PS), which is in interaction with the remaining electrical network (EN), modelled as an infinite energy source. This energy can then be exchanged, either with the room-temperature environment (RT), modelled as an infinite sink, or with the thermal domain via the electrical resistance and resulting ohmic losses. Furthermore, the developed energy by coupling currents (represented in Figure 2.1 by the mutual inductance M_{cc}) can subtract energy from the magnet stored energy and additionally alter the magnet differential self-inductance, as the coupling currents lead to a non-linear relationship between the magnetic flux Φ [T m²] and the magnet current [24].

Usually, superconducting coils are placed within an iron yoke to enhance the field quality and strength. Due to the effect of iron yoke saturation, the differential-inductance of the electric elements decreases with the magnets transport current [15, 24].

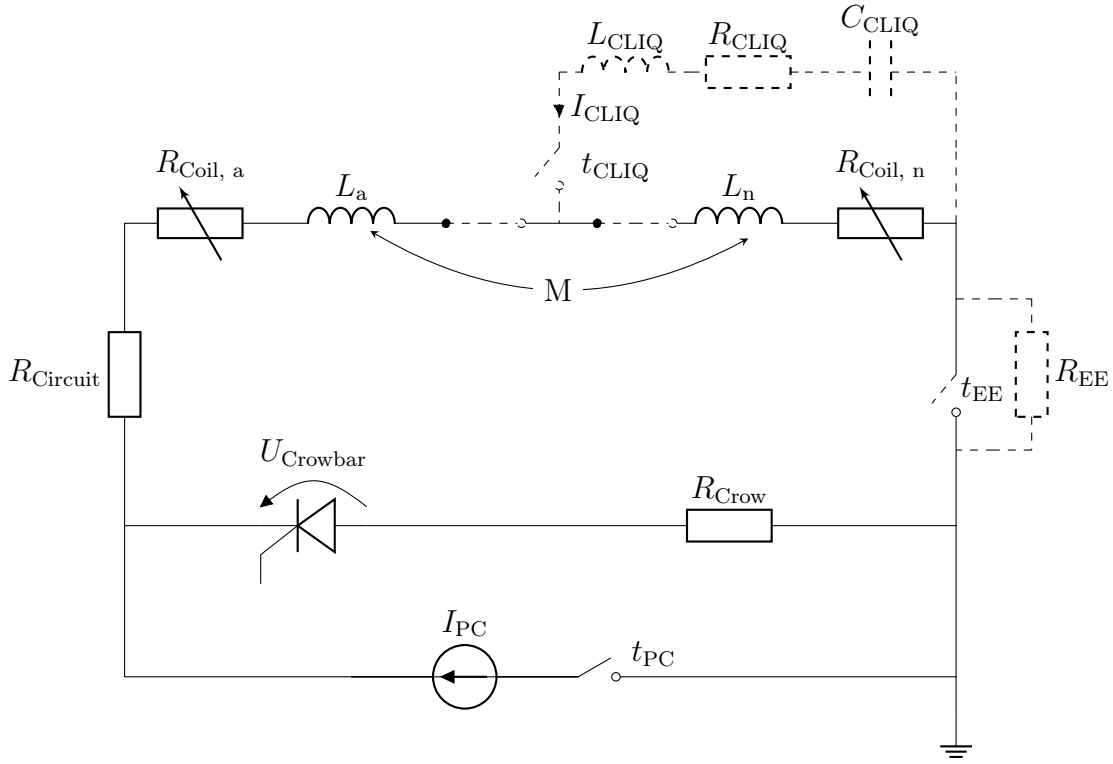


Figure 2.4: Equivalent lumped-element model used in LEDET, showing two electric elements a,n and the simplified electrical circuit, including power source, warm resistance and crowbar. Dashed elements can be optionally included.

2.3.2 Electrical circuit representation

The described lumped element model of the electric elements of the superconducting magnet is combined with a simplified electrical circuit representation, which is shown in Figure 2.4. This circuit additionally contains the power source, as an ideal current source providing I_{PC} , a switch turning the power source on or off at the time t_{PC} [s], the circuit resistance R_{Circuit} [Ω], representing the resistance of the circuits warm parts, as well as a crowbar, which carries the current in the case of a power abort and open circuit across the switch. The crowbar consists of a thyristor, that is opening once the threshold voltage U_{Crowbar} [V] is reached as well as a crowbar resistance. The mutual coupling between the self-inductances of the two electric elements is shown by M . Furthermore, the circuit can contain, based on the chosen quench protection scheme, a CLIQ unit, forcing a current into the magnet in the case of a power abort as well as an energy extraction, simplified as a resistance R_{EE} [36].

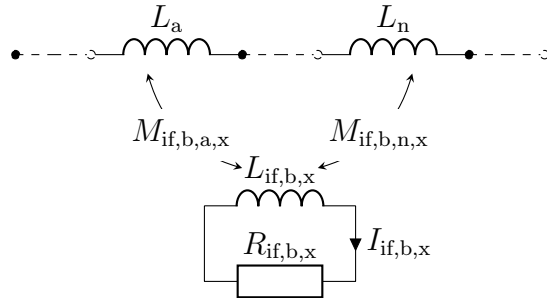


Figure 2.5: Equivalent lumped-element model for the inter-filament coupling currents used in LEDET, showing only the coupling current loop for the x-direction

2.4 Modelling of coupling currents in superconducting magnets

The third lumped-element network aims to simulate the effects of coupling currents in the transients occurring in the magnet. The coupling currents are modelled as current loops, consisting of inductance and resistance, coupled to the inductance of each element of the electric sub-network. In order to model the inter-filament coupling currents, two current loops for each electric element are implemented, that simulate the effects of a magnetic-field change in the x- and y-direction. The modelling of ISCC is only considered for the field change in the direction perpendicular to the cable broad face and hence only requires a single equivalent current loop per electric element. This is justified as this direction usually generates the largest fraction of transitory loss [23, 24]. In Figure 2.5 one loop, showing the coupling of the x-component of the IFCC to the inductances of the electrical sub-network, is shown. The coupling current sub-network of each half-turn in LEDET thus consists of n_{CC} -current loops:

$$n_{\text{cc}} = n_s \cdot 2 + 1$$

with n_s the number of strands in the turn.

The equivalent resistances, self- as well as mutual inductances for the current loops are calculated for each strand and cable and depend on the geometric parameter of the cable/strands, the number of conductors and strands as well as the field change [24]. The generated loss in each strand and cable is thus defined in the model as [24]:

$$P_{\text{if}} = R_{\text{if},x} I_{\text{if},x}^2 + R_{\text{if},y} I_{\text{if},y}^2 \quad (2.9)$$

$$P_{\text{is}} = R_{\text{is}} I_{\text{is}}^2 \quad (2.10)$$

The coupling of the coupling-current sub-network is twofold. First, the generated power introduces heat to the thermal network of the strands and cable (illustrated in Figure 2.1 as P_{CC}). Second, the coupling of the equivalent current loops of the cou-

pling currents to the electric inductances and thus modelling the non-linear, dynamic behavior of the magnets self-inductance.

2.5 Quench modelling

Once energy was introduced into a thermal element, for example, because of IFCC or ISCC or by heat exchange from a neighboring element, the temperature of the respective element starts rising. In the event that more energy is introduced into the thermal element than heat is transferred into the thermal sink or neighboring elements, the temperature continues rising past the critical temperature and the conductor transfers to the current sharing regime, followed by the normal state transition. The conductor can also transfer to normal state once the critical current or field is exceeded. Furthermore, the quench can also be initiated by the user in a pre-defined turn and time. The flag q_b will be set to 1 in the respective time step and the turn will suddenly start to develop an electrical resistance as well as ohmic loss due to Joule heating. In this way, the user can simulate a sudden, unexpected quench, occurring for example due to mechanical movement, and simulate the resulting behavior and transients.

As STEAM-LEDET is only simulating the superconducting magnets in a 2D cross-sectional model, a quench in a half-turn is assumed to appear on the full length of the magnet. Hence, the electrical resistance of the half-turn is developed instantaneously. This assumption holds for quenches, introduced by IFCC and ISCC, as these coupling currents are assumed to appear uniformly along the length of a magnet. On the other hand, for turns that transition to normal state because of heat diffusion from neighboring, already quenched turns, this assumption is overestimating the evolution of electrical resistance in the coil. In reality, a quench first only affects a small part of the conductor, also known as the quench hot-spot. From there on, the heat diffuses along the cable and through insulations and the quench propagates throughout the coil winding pack.

As an approximation to tackle this problem, but still to keep the computational time below full 3D simulations, a feature in STEAM-LEDET was proposed, which models the quench development in a turn into the third dimension using an analytical formula [27, 37]. In this approach, the electrical resistance of each half-turn following a quench is multiplied by the estimated time-dependent fraction of quenched conductor in the longitudinal direction, simulating the longitudinal quench propagation as a running wave along the direction perpendicular to the cross-section. The initial quench is thus propagating from the original hot-spot with an analytically calculated velocity v_q [$\frac{m}{s}$] following [38, 39]:

$$v_q = \frac{J}{\bar{c}} \left(\frac{p\kappa}{T_{cs}/2 + T_c/2 - T} \right)^{1/2} \quad (2.11)$$

where J is the current density of the insulated conductor, p [m] its perimeter, κ [Am^{-2}] its thermal conductivity, \bar{c} [$\text{Jm}^{-3}\text{K}^{-1}$] the volumetric heat capacity and, T_{cs} and T_c its current sharing and critical temperature, respectively. The quench propagation velocity is also often referred to as Normal Zone Propagation Velocity (NZPV). Equation 2.11 approximates the wavefront propagation assuming an adiabatic condition. Hence, the limitations of this approach are twofold. First, as the longitudinal gradient of the thermal evolution is neglected the average resistivity is overestimated, as the temperature for each turn is calculated in the 2D cross-section where the quench started. Second, the pre-heating of the coil-turns due to thermal diffusion from the neighboring elements is neglected in the third dimension. In reality, this could lead to a higher propagation velocity. However, it was shown in the literature that this approach can greatly improve the accuracy of the simulated electrical resistance, while still representing a computationally efficient alternative to a full three-dimensional model [27, 34, 37].

Furthermore, the quench propagation between half-turns following their electrical connections is included. Assuming an initial quench hot-spot in the middle point of a half-turn, the electrically connected return line of the quenched conductor, as well as the following turn in the electrical order, are brought to quench in [37]

$$t_q = \frac{l_{\text{mag}}/2}{v_q} \quad (2.12)$$

where l_{mag} [m] is the length of the magnet. This feature also enables the quench to travel to coil-blocks that were originally in no thermal contact to the coil-block where the hot-spot is located. However, the additional length of the turn due to the bent magnet ends is not taken into consideration but could be included with a correction factor.

A special case has to be considered for magnets that are protected by quench heater. When the quench is detected in the magnet and the capacitor bank is discharged into the strip, all of the heating stations of the QH strip are equally heated up and thus initiate multiple normal zones in the turns to which they are in thermal contact. From each of these normal zones, initiated by the heating stations, the quench is then propagating into both directions. As an example, the main bending dipole MB, with a total length of about 14.4 m, is protected with QH strips with periodic stainless-steel and copper pattern $\frac{l_{\text{QH,SS}}}{l_{\text{QH,Cu}}} [-]$ of 120 mm/400 mm [28]. Thus, the QH strips have

$$n_{\text{QH,stations}} = \frac{l_{\text{mag}}}{(l_{\text{QH,Cu}} + l_{\text{QH,SS}})} = \frac{14.4 \text{ m}}{(0.12 \text{ m} + 0.4 \text{ m})} \approx 28$$

heating stations. The NZPV for the turns connected to these QH strips thus results to:

$$v_q^{\text{QH}} = 2 \cdot n_{\text{QH,stations}} \cdot v_q$$

Furthermore, the coil turns in thermal contact to the turns, to which the QH strips are attached, are heated up as well in multiple zones and thus also in these regions the NZPV is assumed to be v_q^{QH} .

2.6 Co-operative simulation

In Chapter 2.3.2 the simplified electrical circuit representation used in STEAM-LEDET was presented. However, the assumption of this simplified electrical circuit does not hold for some superconducting magnet circuits as these can be significantly more complex, for example including a chain of series-connected magnets and/or by-pass elements. In order to model accurately such circuits, a more sophisticated electrical model needs to be included.

The STEAM framework tackles this problem using the concept of co-operative simulations introduced in the program STEAM-COSIM [30, 31, 32]. The software couples different simulation tools, modelling different physical domains and problems together and tries to achieve convergence in the coupling parameters. The resulting modelling approach thus can handle complex, multi-physics, multi-scale and multi-rate problems, as for example different spatial or temporal scales can be applied to different tools. Furthermore, the tools integrated in the co-operative simulation are optimized for their specific physical domain and phenomena and thus can hugely increase the flexibility and reliability of the model.

In the context of this thesis, this co-operative simulation is combining STEAM-LEDET, modelling the electro-magnetic-thermal magnet domain, and PSPICE[©], modelling the complex electrical circuit. This is achieved by using the calculated current through the coil inductances in PSPICE[©][40] as input parameters for LEDET. LEDET then uses these currents in the different coil sections of the 2D-magnet model to calculate the inductive voltages across the coil sections as well as their electrical resistances. These, on the other hand, are used again as input parameters for PSPICE[©] for the same time window. This procedure is repeated iteratively within each time window until convergence, in terms of pre-defined absolute and relative error tolerances, is reached and the next time window is started. In the literature, this concept is defined as Waveform relaxation [32, 41]. In Figure 2.6 the concept is shown for the coupling of two signals x_1, x_2 between the two simulation tools S_1, S_2 for multiple time-windows T . The convergence for each time step is achieved using the Gauss-Seidel scheme. The scheme approximates the solution of the system of linear equations by sequentially approaching the solution until the convergence criteria are fulfilled.

The implementation in the STEAM framework uses a port-based scheme to implement the signal exchange between the different tools of the co-operative simulation. Prior to the simulation, the user defines the ports between the tools, comprising the port name, possible inputs and outputs as well as the type of signal that shall be exchanged [42].

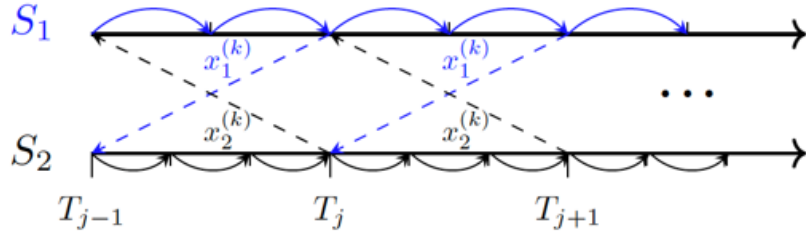


Figure 2.6: Illustration of the concept of waveform relaxation, showing the coupling of signals x_1, x_2 between the two simulation tools S_1, S_2 for multiple time-steps T [41]

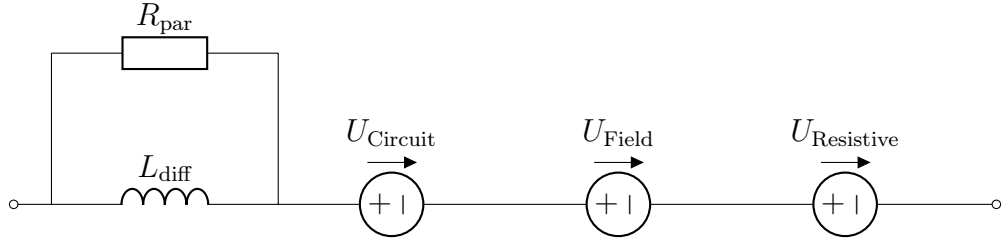


Figure 2.7: Electrical model used in co-operative simulations to combine an electro-magnetic thermal field model (providing U_{Field} and $U_{\text{Resistive}}$) and electrical model

The port-based scheme will then be applied to an electrical model, including the exchanged signals. The model that is used in PSPICE[©] is shown in Figure 2.7. It consists of a differential inductance L_{diff} [H], equivalent to the inductance of the magnet-to-model, in parallel to a resistor $R_{\text{par}} = 1000 \Omega$ that is used for numerical stability. The voltage source U_{Circuit} [V] contains the value of the voltage across the differential inductance from the previous circuit iteration, while U_{Field} [V] includes the inductive voltage calculated by the electro-magnetic thermal model. $U_{\text{Resistive}}$ [V] is the resistive voltage of the coupled magnet and follows:

$$U_{\text{Resistive}} = I_{L, \text{diff}} R_{\text{Coil}} \quad (2.13)$$

where $I_{L, \text{diff}}$ [A] is the current through the differential inductance L_{diff} , calculated by PSPICE[©] and R_{Coil} [Ω] the developed coil-resistance from the electro-magnetic thermal model.

Furthermore, the user has to define the time-stepping and convergence options for the simulation. These are:

- t_{Start} : Definition of the start time of each time window
- t_{End} : Definition of the end time of each time window
- $t_{\text{Step, LEDET}}$: Definition of time step of each time window for STEAM-LEDET

- $t_{\text{Step, PSPICE}}$: Definition of time step of each time window for PSPICE[©]
- $\epsilon_{\text{Relative}}$: Relative tolerance for the convergence calculation, applied to the convergence signal
- $\epsilon_{\text{Absolute}}$: Absolute tolerance for the convergence calculation, applied to the convergence signal
- Execution order: Definition of the order of execution of PSPICE[©] and STEAM-LEDET (Note that multiple LEDET models can run in parallel mode)

Usually, the convergence signal is defined to be $I_{L, \text{diff}}$.

The resulting simulation and modelling approach provides the possibility to simulate the complex fast transients occurring in superconducting magnets with high flexibility and reliability. Thus, different scenarios can be simulated in the specialized tools, while still embedding the most important physical phenomena of the overall system.

3 Automatic generation and validation of superconducting magnet models

After the generation of a superconducting magnet model, its validation against experimental results is required in order to ensure their reliability. Most of these models contain some unknown parameters which impact different physical transients. These parameters were either not measured for each specific magnet because of too much required effort or, simply because of their complex nature, not measurable. Thus, they need to be found with simulations.

The superconducting magnet models of the STEAM framework at CERN are generated using dedicated Jupyter Python notebooks and an in-house developed application programming interface (API). These facilitate a relatively quick, easy and semi-automatic generation of the models, while still preserving and ensuring user-friendliness, versioning and consistency.

However, for the validation, numerous simulations have to be performed. The framework developed for this thesis provides the possibility to set up, run and evaluate these fully automatically. In Chapter 3.1 the general implementation of the framework will be discussed and a coding example for its usage will be provided. The Chapters 3.2 and 3.3 then will show two use-cases of magnet families which were validated using the framework. These are a self-protecting 120 A superconducting magnet in Chapter 3.2 and the recombination and separation dipoles in Chapter 3.3.

3.1 Implementation

The superconducting magnet models are first generated semi-automatically in generic Jupyter notebooks. These require the user only to provide a limited number of inputs, such as conductor physical and geometrical parameters, information about the electrical connections as well as information about the reference simulation such as for example opening times of switches. Furthermore, the notebooks also require the magnetic field maps and strand locations in the 2D geometry. These were generated using the software ROXIE [43, 44].

The Jupyter notebooks then use this information to structure the data and calculate further information, such as the self-and mutual-inductances of all turns or the thermal connections in between neighboring turns. As a result, the notebooks generate a reference Excel-File containing all the relevant information about the magnet. This file, together with the magnetic field map from ROXIE, is the basis for the developed framework. The reading and writing of the STEAM-LEDET Excel-Files are performed with a class called 'LEDETParameters' in the STEAM notebook API [45]. The full class diagram of the framework is shown in Figure 3.1. The central component of this new framework which is part of the described API is a class called 'ParameterSweep'. This class requires as an input a pre-generated reference model file of the magnet [46]. Furthermore, the user also has to provide information about

3.1 IMPLEMENTATION

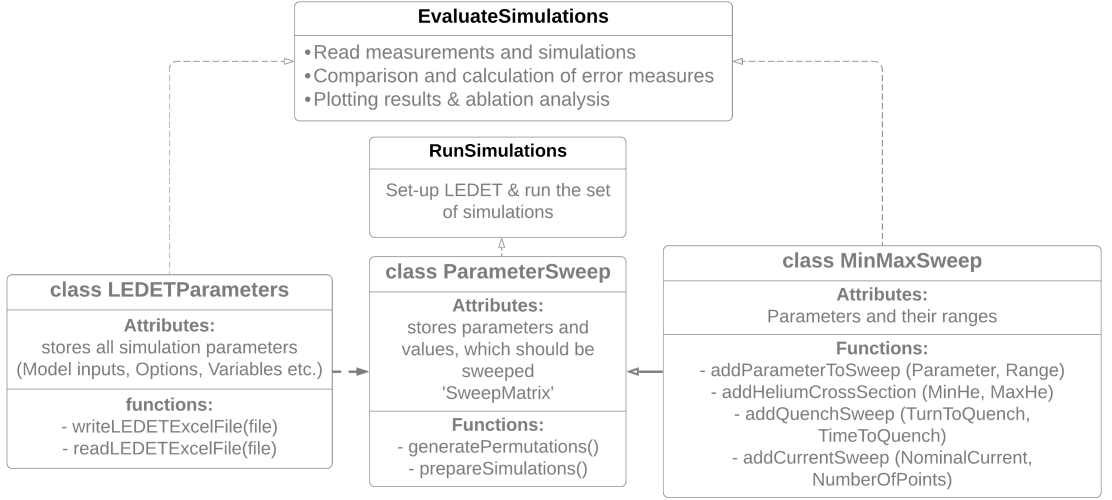


Figure 3.1: Class diagram of the new additions to the STEAM notebook API, providing the possibility to set up a full set of simulations with varying parameter combinations

which parameters should be changed, in which range of values and how many data points for each parameter shall be investigated. This is performed in the child class 'MinMaxSweep'. Using the child class provides the possibility to add in the future further functions with different assumptions to the framework. The class 'ParameterSweep' then generates a variable 'SweepMatrix' that contains all possible combinations of these simulations.

Following this generation, the framework then reads the provided reference file, adjusts the parameter according to the 'SweepMatrix' and writes the file back into the simulation directory. This is repeated for all rows of the 'SweepMatrix'. As a result, a set of

$$n_{\text{Simulations}} = \prod_{k=1}^l n_k \quad (3.1)$$

is generated, where l [-] is the number of parameters and n_k [-] the number of tried values for each parameter.

Afterwards, the simulations can be run automatically and the results are read. The user can specify whether to read from .txt files, requiring less space, or from .mat files. In the evaluation part of the framework, realized in the class 'EvaluateSimulations', the results of all simulations are then compared to a measurement which was provided by the user. For example, these measurements can be obtained using the LHC Signal monitoring API [47], which can be easily combined with the Python code for the evaluation. The evaluation calculates different error measures, such as root-mean-square error, the smallest absolute deviation between measurement and simulation or differences in quench loads. Furthermore, it conducts an ablation analysis to

investigate the sensitivity of the model to each of the parameters. The results of this evaluation analysis will be shown in the Chapters 3.2 and 3.3.

A short coding example explaining some of the functions is shown in the Annex in Listing 1. The process is split into five phases:

1. Initialization, providing and loading the reference simulation file. All parameters and options that are included in the reference file can be used in the parametric sweep or manually changed in the process.
2. Setting the parameter values which are planned to be investigated. The user can provide the range as well as how the data points should be arranged (e.g. linearly or logarithmically between a minimum and maximum). Alternatively, fully customized vectors with values can be included. Specific sweeps are realized with dedicated functions (e.g. including sweeps of f_{He} , current level or quench location). The different parameter and their values do not need to have the same number of points.
3. Preparation of the simulations, which writes all files in the correct directories. Together with the STEAM-LEDET simulation files, also an additional file, including the 'SweepMatrix' is written. This file can be used later, e.g. in the evaluation, or to repeat sweeps at another time.
4. Running the simulation, one after each other.
5. Plotting of the results, comparison to the measurement and calculation of error metrics and ablation analysis. So far, the framework only supports comparison to one measured current. Future work could extend this, e.g. for voltages or multiple current levels.

3.2 Validation of a self-protecting 120 A superconducting magnet model

The LHC contains a series of self-protecting magnets. These magnets are usually powered at lower current levels and are not protected by any quench protection system, but fully rely on the heat dissipation within their coils. The modelling of such magnets thus represents a special challenge. The thermal diffusion and quench development inside the coils are of special interest and the electro-thermal-magnetic model needs to properly take them into account, as the heat exchange within the coil winding pack, especially also into the longitudinal, third dimension, are the governing mechanisms for their discharge.

As an example for a magnet from this family, in this chapter the self-protecting MCBY magnet will be presented and the automatic validation framework will be applied. Therefore, in Chapter 3.2.1 the MCBY magnet [1, 46, 48] will be presented

and afterwards, in Chapter 3.2.2 the impact of the variation of the free parameters in the MCBY model will be shown.

3.2.1 The MCBY magnets

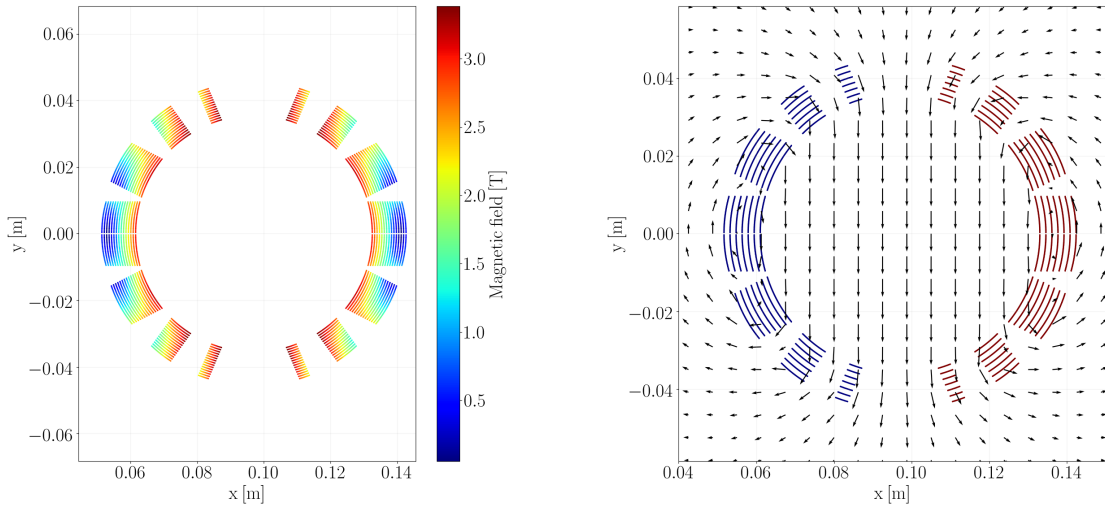
The LHC MCBY magnet is a self-protecting, superconducting Nb-Ti dipole magnet operated at current levels up to 120 A. These magnets are used in the LHC as dipole orbit correcting magnets and are installed in the insertion regions, in order to prepare the beams to be merged into a single beamline. They come in two versions, one generating a horizontal dipole field with vertical beam correction (MCBYV) and another generating a vertical dipole field with horizontal orbit correction (MCBYH). Both magnets are identical for the 90 degrees rotation of their cross-section [1]. However, in the scope of this thesis, only the MCBYH magnet will be validated. The magnets are twin-aperture dipoles, where both modules are mounted together in a common support structure. Because of the presence of an iron yoke in the mechanical support structure, the two-beam apertures are magnetically decoupled and are therefore simulated independently.

Due to the fact that the circuits of the MCBYH magnet only contain one magnet aperture, the transients occurring in the circuit and the magnet can be simulated using STEAM-LEDET as a stand-alone tool. The main parameters of the MCBY magnet and its conductor are summarized in Table 2.

Table 2: Main magnet and conductor parameters of the LHC MCBY magnet [1], used in the simulations

| Parameter | Unit | Value |
|---|------|-------|
| Nominal current, I_{nom} | A | 88 |
| Nominal field strength at I_{nom} | T | 3.0 |
| Peak field in the conductor at I_{nom} | T | 3.4 |
| Operating temperature | K | 1.9 |
| Differential inductance at I_{nom} | H | 5.27 |
| Maximum stored energy | kJ | 13.7 |
| Number of turns | - | 2670 |
| Magnetic length, l_{mag} | m | 0.899 |
| Conductor width | mm | 0.67 |
| Conductor height | mm | 0.32 |
| Cu/SC Ratio | - | 4.4 |
| Conductor insulation thickness | mm | 0.03 |
| Wedge and collar insulation thickness | mm | 0.2 |
| Filament Twist-Pitch (guess value) | mm | 0.015 |

The magnetic field in the conductors of the MCBYH magnet reaches a maximum of



(a) Magnetic field in the MCBYH coils, calculated using ROXIE [43, 44] and including iron yoke effects

(b) Magnetic field lines inside the MCBYH, ignoring iron yoke effects. Colors indicate polarity of the transport current (blue = negative, red = positive)

Figure 3.2: Magnetic model of the MCBYH magnet

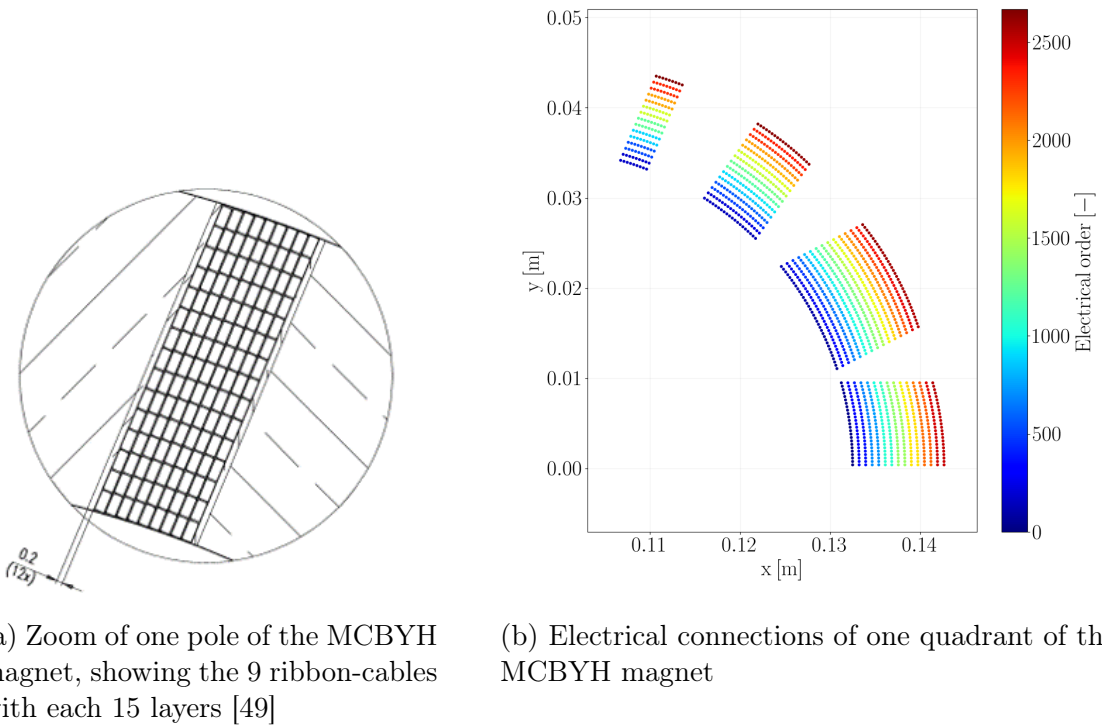
around 3.4 T at nominal current. The magnetic field inside the coils, as well as the field lines (ignoring the iron effect) inside the magnet, are shown in Figure 3.2 [48].

One magnet aperture has an outer diameter of 159.8 mm and an inner diameter of 70 mm. The total length of one magnet is 1.1 m. Due to the saddle-shaped coils and their magnet ends, its magnetic length is only defined to be 0.899 m.

There are two dipole coils which consist of LHC flat-ribbon cables. These are built by winding 15 layers of LHC Type Corr-02 conductors together (compare Table 17) [1]. The 15 layers are then electrically connected in series at the coil end. The wires have a rectangular cross-section and are arranged and insulated as a ribbon-cable conductor. Hence, it is assumed that they are very well impregnated and no helium penetrates between the wires and their insulation layer, nor between adjacent wires.

In Figure 3.3a one of the pole blocks of the MCBYH magnet can be seen, showing the 9 ribbon cables with each 15 layers. In Figure 3.3b the electrical connections of the turns of one quadrant are shown. For this special magnet, the turns in the ribbon cables are connected layer by layer. Note that only the odd numbers are shown, as the return lines to the shown, first quadrant, are located in the second quadrant. The electrical connections of the layers are shown in the Annex in Figure F.1.

Each of the MCBYH magnets is powered in its own RCBY circuit, where the magnet is in series with the power converters and a circuit resistance. A crowbar is present in parallel to the power converter, which provides an alternative path for the circuit current when the power converter is switched off. The electrical diagram of these



(a) Zoom of one pole of the MCBYH magnet, showing the 9 ribbon-cables with each 15 layers [49]

(b) Electrical connections of one quadrant of the MCBYH magnet

Figure 3.3: Electrical model of the MCBYH coils

circuits thus equals the electrical circuit included in STEAM-LEDET and shown in Figure 2.4. The power converters used for these circuits are the RPLBx /LHC 120 A - 10 V [50]. These provide a maximum current of up to ± 120 A with a maximum voltage of ± 10 V. The power supply also includes the crowbar, which consists of two back-to-back thyristors and an $R_{\text{Crowbar}} = 80$ m Ω resistance connected in series. The thyristors are activated when the voltage across them becomes larger than 13 V. When the thyristors are conducting, the voltage drop across them is around $U_{\text{Crowbar}} = 0.9$ V. The circuit cables have a resistance of about $R_{\text{Circuit}} \approx 67$ m Ω . In circuits of this family, the current I_{Meas} is measured within the power converters. In the case of a fast power abort (FPA) at t_{PC} [s] and the disconnection of the power supply from the circuit, the current in the circuit I_{Circuit} [A] needs to be calculated using the measured output voltage U_{Out} [V] and the equations:

$$I_{\text{Circuit}} = \begin{cases} I_{\text{Meas}} & t \leq t_{\text{PC}} \\ \frac{U_{\text{Out}} - U_{\text{Crowbar}}}{R_{\text{Crowbar}}} & t > t_{\text{PC}} \end{cases} \quad (3.2)$$

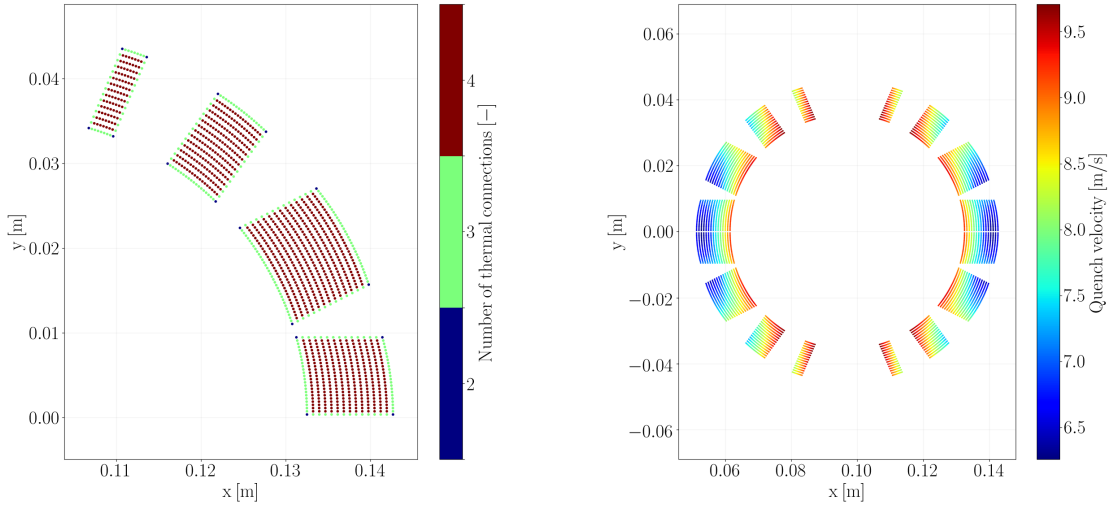
and the experimental coil resistance $R_{\text{Exp,Meas}}$ [Ω] is calculated as:

$$R_{\text{Exp,Meas}} = \frac{U_{\text{Out}} - L_{\text{mag}}(I) \frac{dI_{\text{Circuit}}}{dt}}{I_{\text{Circuit}}} \quad (3.3)$$

where $L_{\text{mag}}(I)$ [H] is the current-dependent magnet inductance. The effect of coupling currents on the differential inductance is neglected in this calculation.

The thermal model of the MCBYH magnet simulates the heat diffusion between the different coil turns of the magnet. All thermal connections between the coil turns are thus included in the model. These are calculated based on the spatial orientation and distance and are separated into thermal connections along the narrow and along the wide side of each turn. Depending on into which group each of these thermal connections falls, the contact area and insulation properties are adjusted to calculate the thermal resistance $R_{b,h}$ for the respective neighbors, as described in Chapter 2.2.1 and the resulting diffusing heat. Figure 3.4a shows the number of thermal connections for each turn in the first quadrant along the narrow as well as along the wide side. Most of the turns in the MCBYH magnet are thermally connected into all directions of the 2D cross-section. Thus, the heat can propagate quickly within each coil block.

Furthermore, it was shown that the modelling of the quench propagation into the third dimension becomes crucial for self-protecting magnets [37]. First, this includes the quench propagation along the longitudinal direction of the magnet, scaling the electrical resistance based on the fraction of quenched half-turn in the longitudinal direction. Second, this includes the quench propagation following the electrical connections. Including the latter enables the quench to also propagate into coil blocks



(a) Number of thermal connections, including along the narrow and wide side, for each turn in the first quadrant

(b) Analytically calculated quench propagation velocity at nominal current, following Equation 2.11 for the MCBYH magnet

Figure 3.4: Thermal connections and quench propagation velocity of the MCBYH magnet

that are not in thermal contact with the initial quenching part of the coil. The quench propagation velocity, which was calculated according to Equation 2.11 for each half-turn, is shown in Figure 3.4b and is included in the model. The quench propagation velocity is automatically re-calculated by the framework for each current level.

3.2.2 Parameter variation and their impact

The model of the MCBYH requires some parameters, which were, so far, not measured for this type of magnet or simply can not be practically measured, as they include very complex phenomena. For the MCBYH magnet, the validation is mainly about the determination of the two parameters: RRR and $f_{\rho,\text{eff}}$. The first parameter influences multiple phenomena in the wires during the transient. The second parameter is a governing parameter in the modelling of the inter-filament coupling losses. Note that for the MCBYH magnet also the filament twist pitch is not known and only a guess value is used. However, as the filament twist pitch, as well as $f_{\rho,\text{eff}}$ are closely related, only the parameter $f_{\rho,\text{eff}}$ is changed and assumed to include the uncertainty introduced by the twist-pitch. Moreover, as the MCBYH magnet is self-protecting, also the quench origin might impact the transient occurring in the magnet. During the validation, few different quench locations will be considered. However, this will be investigated in more depth in Chapter 4.2.

Other parameters, for example the cross-contact resistance (R_C) or the helium fraction (f_{He}) do not influence the transients in the MCBYH magnet and are therefore neglected. This is justified by the fact that the magnet only contains single-stranded conductors and these conductors are well insulated and impregnated due to their fabrication.

The validation of the MCBYH magnet was conducted solely in STEAM-LEDET, which was justified in Chapter 3.2.1. The determination of the optimal parameter set was performed by comparing the STEAM-LEDET simulation results with experimental data collected during LHC operation. Quench events occurring in the MCBYH magnet introduce the challenge to deduce the exact moment of quench in the magnet. As the electrical resistance of the spot where the quench starts is initially rather small, the resistive voltages during the early moments of a quench in this magnet are too small to be detected within the measured noise. Hence, the time of the quench cannot be determined exactly. The quench may already spread through parts of the magnet coil, but the resistance is not rising enough to be detected. In Figure 3.5 the measured current derivative shortly before the power abort is shown. After the current reaches its nominal current plateau, the current starts decreasing around -150 ms before the power supply is switched off. This indicates that the quench occurred at least at that moment, and possibly even earlier. The initial time

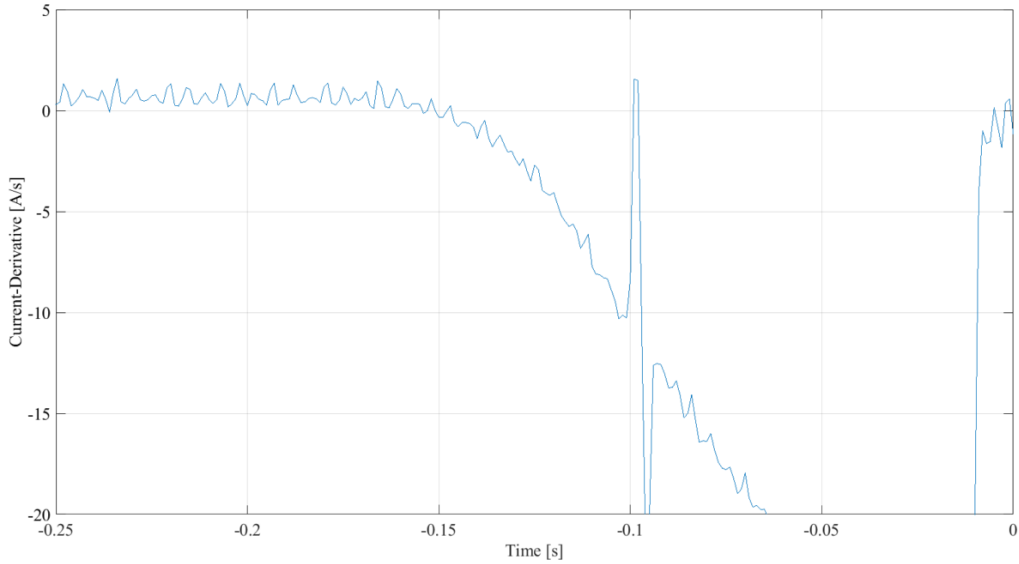


Figure 3.5: Current derivative in one quench event in an MCBYH magnet, shortly before the power abort at $t_{PC} = -18$ ms

of quench in the simulations is set to:

$$t_q = -185 \text{ ms}$$

The initial quench hot-spots in this validation are assumed to be in the high-field areas, in the innermost layer of the magnet, where it is most likely for a turn to quench, given the lower margin to quench. In Figure 3.6 the minimum required quench energy for all turns in the MCBYH magnet is shown. These were calculated following Equation F.1, which is shown and explained in the Annex F. As the transients in the MCBYH magnet can differ depending on the assumed quench location, the validation takes different quench locations into account. The considered locations are indicated in Figure 3.6 by Q1-8. The locations are solely selected from the second quadrant, as the turns in this quadrant are placed in the center of the electrical connections. Further locations are studied in more depth in Chapter 4.2. In order to find the optimal parameter set, the framework sets up automatically all combinations of the parameter and the proposed locations. The total set of 288 simulations is summarized in Table 3.

The resulting current transients for all simulations, compared to a measurement, are shown in Figure 3.7. The color gradient in Figure 3.7 indicates the root-mean-square error (RMSE) [A] between the measurement and the respective simulation, calculated following :

$$\text{RMSE} = \sqrt{\frac{1}{N} \sum_{n=0}^N (I_{\text{Meas}} - I_{\text{Sim}})^2} \quad (3.4)$$

Table 3: Simulation summary for the validation of the self-protecting magnet MCBYH

| Parameter | Number of data points | Range of values | Type |
|---|-----------------------|------------------------------|--------|
| RRR | 6 | [75, 300] | Linear |
| $f_{\rho, \text{eff}}$ | 6 | [0.75, 3] | Linear |
| Quench location | 8 | High field: midplane to pole | |
| Total number of simulations: 288 | | | |

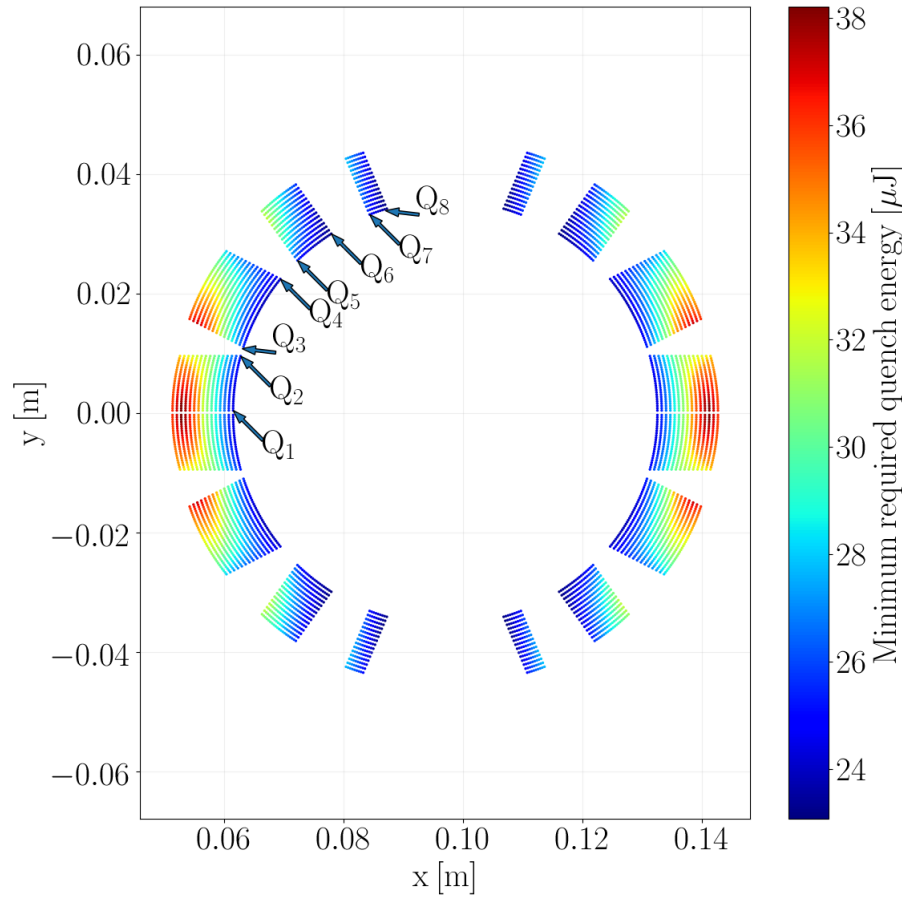


Figure 3.6: Approximated minimum required quench energy for each turn in the MCBYH magnet at nominal current and indication of all considered quench locations for the validation (marked with Q1-8)

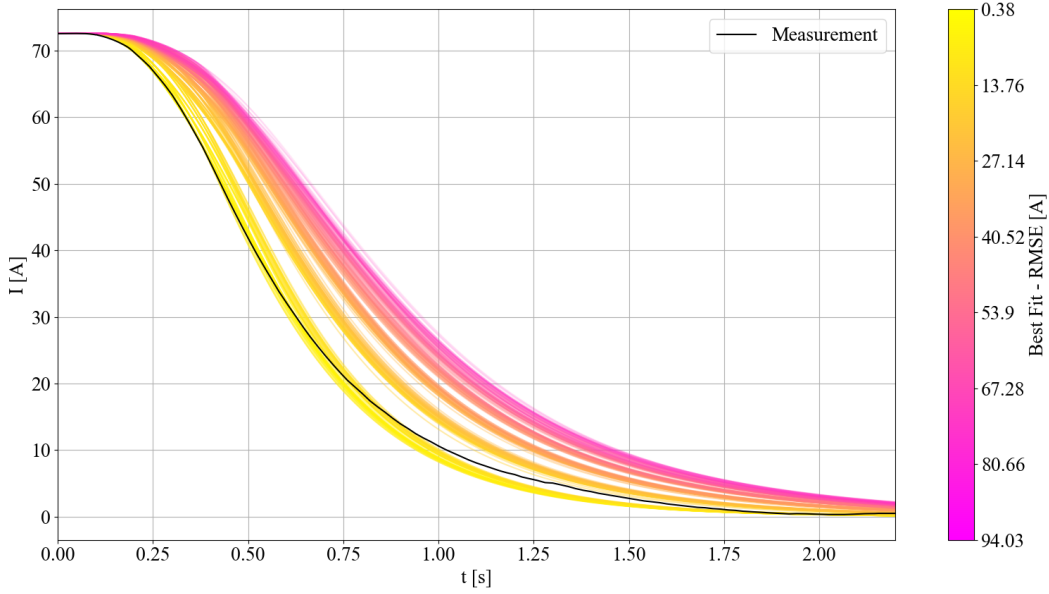


Figure 3.7: Current decay in the MCBYH magnet for all performed simulations, showing the root-mean-square error (RMSE) compared to measurements, after a fast power abort at $t_{PC} = 0$ s.

with N [-] the total number of measured data points. One can observe that in the whole set different branches form. The current decay in the simulations is in general slower than in the measurement. However, one branch shows rather good agreement with the measurement.

In order to better investigate the simulations and their results, the quench load difference as a function of the simulation number is shown in Figure 3.8. The quench load QL [A^2s] is defined as:

$$QL = \int_{t_{PC}}^{\infty} I^2 dt \quad (3.5)$$

The quench load is calculated from t_{PC} to ease the comparison with the measurement. The quench load is often used to compare or evaluate current transients in superconducting magnets, as it is roughly proportional to the energy deposited in the hot-spot [19].

Figure 3.8 shows the relative difference of the measured quench load $QL_{Meas} = 2.377$ kA 2 s with respect to the calculated quench loads for each simulation. The color gradients indicate the distribution of the applied parameter.

One can observe that the differences range from almost 0% up to 55%. This is mostly governed by the parameter RRR which is being gradually increased within each group of 48 simulations. The larger the RRR, the larger the difference between measured and simulated quench load becomes. Also, the different quench positions seem to influence the simulated transient. For most sets of eight simulated quench

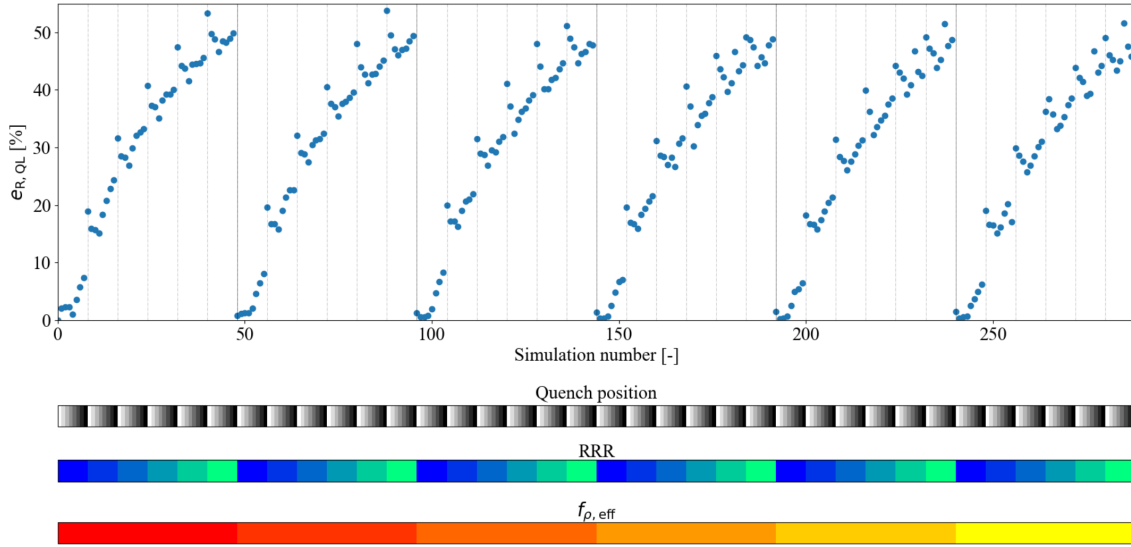


Figure 3.8: Relative difference of the simulated quench loads and measured quench load as a function of simulation numbers. Color gradients indicate the distribution of simulated parameter

positions Q1-8, one can observe a "V"-shape. The quench position Q1, as well as Q5-8, seem to fit less to the selected measurement. Furthermore, Figure 3.8 shows that the parameter $f_{p,eff}$ has only a little impact on the simulation of the transient, as the overall quench load difference does not greatly vary along the full set of simulations.

In Table 4 the results for the best and worst fitting simulations are shown. These include as metrics the relative quench load difference $e_{R,QL} [\%]$, the maximum absolute error between simulations and measurement $\max(|e|) [A]$ as well as the RMSE. Table 4 shows the best two simulations with respect to RMSE (Simulations 147 & 195), largest absolute difference (Simulations 0 & 193) and relative quench load difference (Simulations 192 & 240). The worst fitting simulations (Numbers 285, 40, 88) show the highest error in all performance measures.

The selected best-fitting simulations show an excellent agreement with the measurement. The relative quench load difference is below $<1.5\%$ and can even be reduced to less than 0.3% for selected simulations. The maximum absolute difference between measurements and simulations is also below $<2 A$, which corresponds to a maximum relative error of $<3\%$ with respect to the initial current.

All of the well-fitting simulations were performed assuming a RRR of 75. However, the value of RRR always depends on the assumed reference temperatures. STEAM-LEDET and the specification assume different cryogenic and room reference temperatures [16, 51]. Thus, a correction factor of 1.086 needs to be applied, if converted. The applied RRR value in STEAM-LEDET would correspond to 81.5, assuming the

reference temperatures in the specification. The specification for the MCBYH magnet mentions a $\text{RRR} > 100$ [1, 21]. The best-fitting value for RRR thus would be slightly smaller as specified.

Table 4: Obtained errors and quench loads for the selected best and worst simulations in the set of conducted simulations. Quench load of the measurement: $QL_{\text{Meas}} = 2.377 \text{ kA}^2\text{s}$

| Simulation number | $f_{\rho,\text{eff}}$ | RRR | Quench position | RMSE [A] | $\max(e)$ [A] | QL [kA^2s] | $e_{\text{R},\text{QL}} [\%]$ |
|-------------------|-----------------------|-----|-----------------|----------|-----------------|------------------------------|-------------------------------|
| 147 | 2.1 | 75 | 4 | 0.61 | 1.86 | 2.363 | 0.62 |
| 195 | 2.55 | 75 | 4 | 0.62 | 1.87 | 2.363 | 0.62 |
| 193 | 2.55 | 75 | 2 | 0.66 | 1.95 | 2.372 | 0.21 |
| 194 | 2.55 | 75 | 3 | 0.66 | 1.95 | 2.373 | 0.21 |
| 192 | 2.55 | 75 | 1 | 0.85 | 1.83 | 2.411 | 1.43 |
| 240 | 3 | 75 | 1 | 0.85 | 1.83 | 2.412 | 1.46 |
| ... | | | | | | | |
| 285 | 3 | 300 | 6 | 9.41 | 22.89 | 3.603 | 51.6 |
| 40 | 0.75 | 300 | 1 | 9.62 | 23.00 | 3.644 | 53.30 |
| 88 | 1.2 | 300 | 1 | 9.70 | 23.29 | 3.656 | 53.79 |

As shown in Figure 3.8 is the impact of $f_{\rho,\text{eff}}$ rather small. However, a value of 2-3 seems to achieve the best simulation results. The literature proposes for magnets with rectangular wires and an width/height ratio of about 2, a value of $f_{\rho,\text{eff}}$ approximately between 2 - 4 [52]. As the magnetic-field change during the discharge of this magnet is rather low, inter-filament-coupling losses do not play an important role. Inter-strand coupling currents do not occur as only single-stranded wires are used. Furthermore, also the quench position changes the current transient. In general, the quench positions 3 and 4 seem to provide the best simulation results. These positions are the edges of the largest coil block. Hence, a quench in these positions would lead to a fast quench propagation through the wire insulations throughout the block. On the other end of the simulations, assuming a RRR value of 300 leads to a very poor agreement with the measurement. For different values of $f_{\rho,\text{eff}}$ and the quench position, the error can reach more than 50% in the quench load. The maximum absolute difference between measurement and simulation can reach about 23 A, which correspond to a maximum relative error of 32% with respect to the initial current.

As the best fitting parameters $\text{RRR} \in [75, 100]$ and $f_{\rho,\text{eff}} \in [2.1, 2.5]$ are proposed. For the given measurement it is most likely that the quench started in position 4, centered between midplane and pole.

Assuming the proposed parameter set, the framework also conducts an ablation analysis. While one parameter is being changed, the others remain fixed. This can

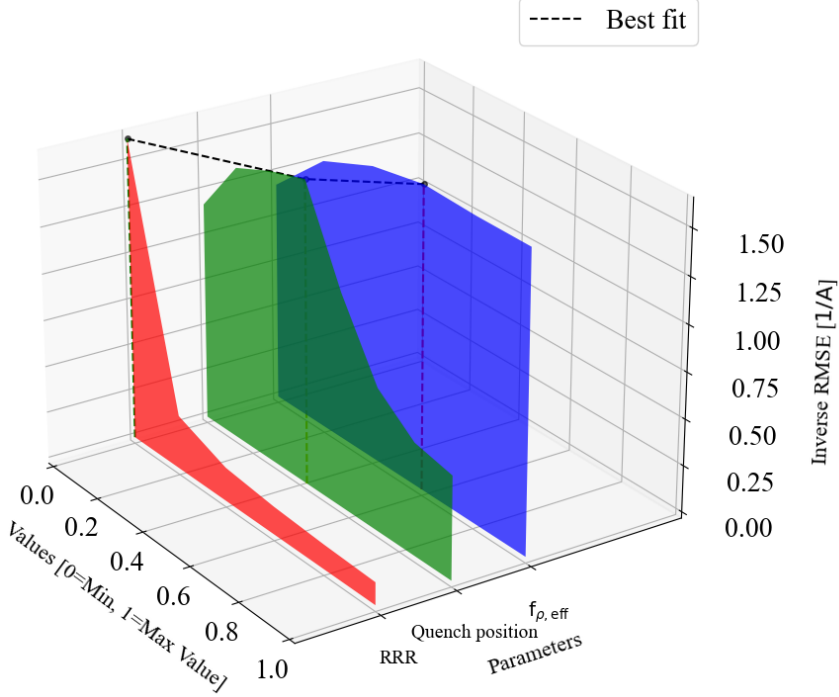


Figure 3.9: Ablation analysis of the MCBYH model to the selected parameter. Dependency of the inverse RMSE to changing one parameter at a time. If not changed, values are fixed to $\text{RRR} = 75$, $f_{\rho,\text{eff}} = 2.1$ and Quench position 4.

provide insights into the sensitivity of the specific model towards a parameter. This is illustrated in Figure 3.9 which shows the dependency of the inverse RMSE [$\frac{1}{A}$] to changing one parameter at a time. Note that the inverse RMSE is only chosen for illustration reasons.

One can see that changing only $f_{\rho,\text{eff}}$ does not greatly impact the error. This can also be observed in Figure 3.10 which shows the current decay compared to the measurement for the different applied values.

The assumed position where the quench starts, on the contrary, can increase the error by almost a factor 3, as it can be seen in Figure 3.9. The current decays of these simulations, compared to the measurement, are shown in Figure 3.11. Changing the location of the initial hot-spot especially changes the initial rate of the current decay. This correlates to the size of the coil-block, where the quench is assumed to start. Following Equation 2.12 the quench propagation along the electrical connection would take about 45 ms, assuming a quench in the middle point of the half-turn and the analytically calculated quench propagation velocity shown in Figure 3.4b. Meanwhile, in the MCBYH the quench propagation through the insulation into a thermally connected neighbor takes only about 4 ms. Hence quench hot-spots in a larger coil-block lead to a faster current decay.

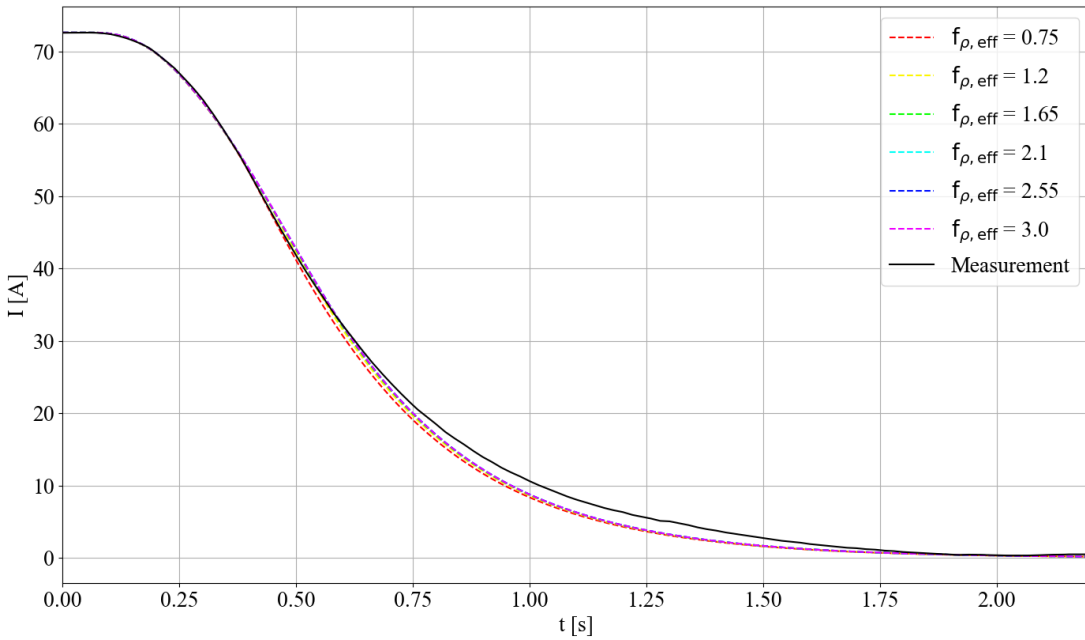


Figure 3.10: Simulated current decays for various values of $f_{\rho, \text{eff}}$, compared to a measurement. RRR = 75 and quench position 4 are fixed.

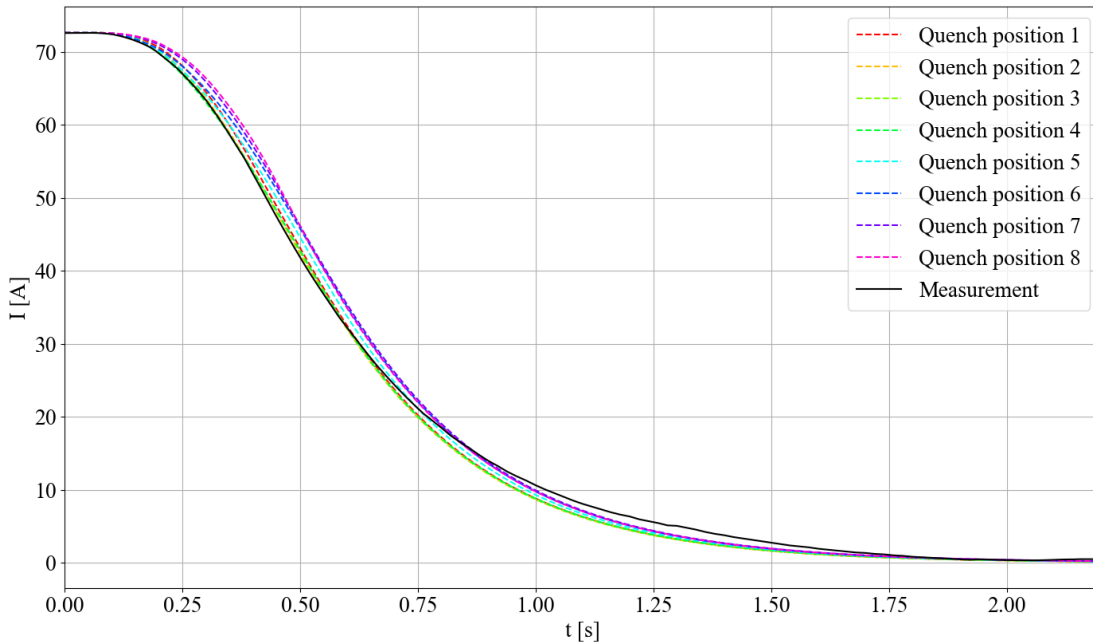


Figure 3.11: Simulated current decays for various initial quench positions, compared to a measurement. RRR = 75 and $f_{\rho, \text{eff}} = 2.1$ are fixed.

3.2 VALIDATION OF A SELF-PROTECTING 120 A SUPERCONDUCTING MAGNET MODEL

The RRR has the strongest influence on the model performance. Already slightly increasing the value of RRR above 100 leads to a significant error between the measurement and the simulations. In Figure 3.12 the different current decays for all investigated RRR values are shown.

Furthermore, one can obtain more insights into the model behavior and the fitting of the simulations by investigating the coil-resistance evolution. The experimental coil resistance is thus calculated following Equation 3.3. In Figure 3.13 the evolution of the simulated coil resistances from selected simulations from Table 4 are shown. These are compared to the experimental coil resistance. Note that the coil resistance is only shown until 1 s, since afterwards the experimental circuit current becomes smaller and relatively noisy.

One can see that the simulated coil resistances also show a very good agreement with the experimental coil resistances. The evolutions for the different selected simulations are all very similar. Especially the initial development of the coil resistance, before the power supply is switched off, is very well captured in the model. Only after the coil resistances reach their maximum, simulated and experimental resistance start to diverge. This might be caused by additional cooling effects in the magnet, which are not included in the model.

Only the simulations that were not representing the current decay accurately also show a poor agreement in the coil resistance. The simulations assuming an RRR = 300 show a coil resistance that is almost lower by a factor of two with respect to the best

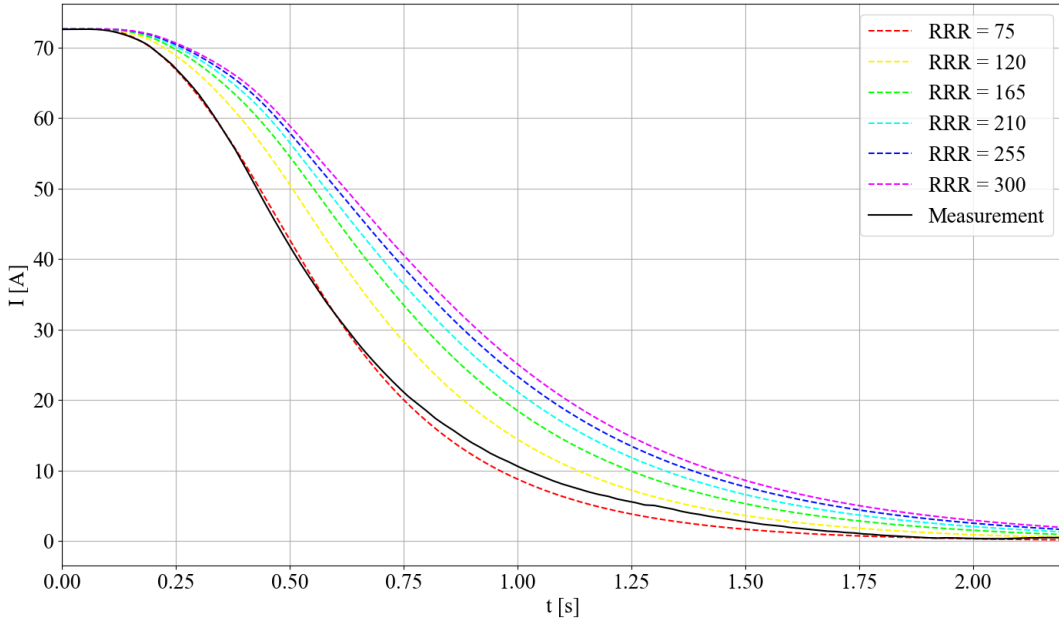


Figure 3.12: Simulated current decays for various values of RRR, compared to a measurement. $f_{\rho,\text{eff}} = 2.1$ and quench position 4 are fixed.

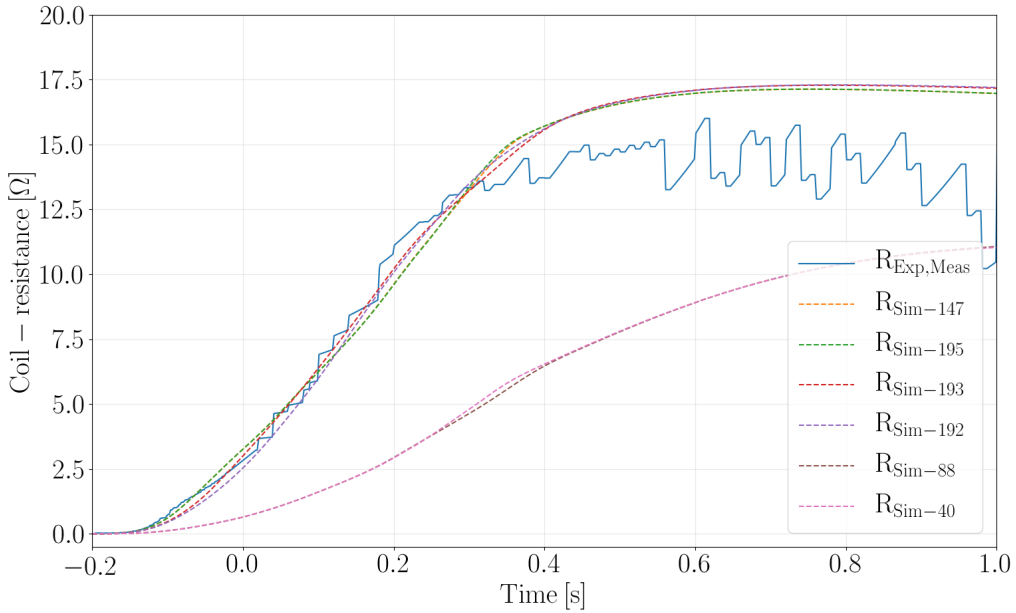


Figure 3.13: Evolution of the simulated coil resistance compared to experimental coil-resistance for selected simulations from Table 4.

fitting simulations. The coil resistance development for the proposed parameter set and only changing one parameter at a time are shown in the Annex in Figure F.2 for RRR, Figure F.3 for different initial quench positions and in Figure F.4 for $f_{\rho,\text{eff}}$. In Figure 3.14 the simulated evolutions of the fractions of conductor in normal state, as well as the evolution of the hot-spot temperatures for some selected simulations from Table 4, are shown.

Figure 3.14 illustrates the evolution of the quench throughout the magnet for the different cases. As the quench propagation along the electrical connections into another coil block, not in thermal contact, takes time, the different initial quench positions are largely governing the shape of the evolution. The difference between the selected good and bad fitting simulations is mainly the significant difference in the hot-spot temperature, caused by the higher RRR in simulations 88 and 40. The higher RRR results in lower resistance and thus lower temperatures. This slows down the quench propagation. Hence, in the simulations with higher RRR, the hot-spot temperature increases more slowly at the beginning of the transient due to the lower conductor resistivity. However, at the end of the discharge, a higher hot-spot temperature is reached since the current discharge was much slower due to the slower coil resistance increase.

Thanks to the framework it was possible to set up and perform quickly a large variety of simulations for the MCBYH magnet. Different parameter sets were investigated and, based on the comparison to a measurement from real operation, the best fitting

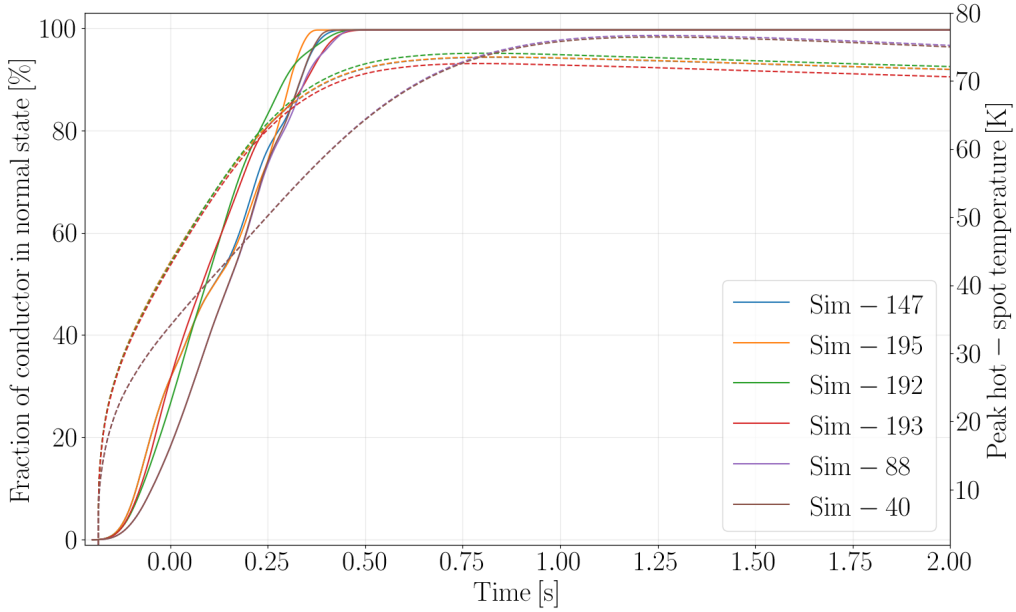


Figure 3.14: Simulated fractions of conductor in the normal state (solid lines) and simulated hot-spot temperatures (dashed lines) for selected simulations from Table 4.

parameters were found. Furthermore, the framework provided additional insights into the sensitivity of the model to the parameters as well as into the general transitory behavior of the magnet.

3.3 Validation of the LHC separation and recombination magnet models

Another family of magnets in the LHC are the separation and recombination dipoles. These magnets are placed before and after each of the four interaction regions of the LHC and are utilized either to bend the magnets onto their combined beamline or to separate the beams after the interaction region again. The magnet family consists of four very similar magnets - MBX, MBRB, MBRC and MBRS. These magnets are also referred to as IPD magnets (Individually Powered Dipoles).

The IPD magnet coils are made of multi-stranded wires and are protected by quench heaters. Thus, the validation of these magnets represents another interesting application case for the framework, as the set of unknown parameters is different.

In the following Chapter 3.3.1, the magnets and their models will be shortly presented. In Sub-chapter 3.3.2 , the validation of the magnet models will be demonstrated and discussed.

3.3.1 The LHC separation and recombination magnet models

The family of IPD magnets consists of four magnets, three of which are composed of two apertures (MBRB/C/S) and one of one aperture (MBX) [1]. The two dipoles MBX and MBRC are used in the experimental insertions as the separation and recombination dipoles, while MBRS and MBRB are used in the radio-frequency insertions. The MBRC and MBRB are magnets with a common iron yoke for both apertures, while MBRS is a twin aperture with two independent, magnetically decoupled iron yokes for each aperture. Thus, the apertures of MBRS are modelled independently. The total length of one magnet is 9.8 m, while the magnetic length is around 9.45 m. The magnet and conductor parameters for the four magnets are summarized in Table 5.

Table 5: Main magnet and conductor parameters of the LHC IPD magnets [1], used in the simulations

| Parameter | MBRB | MBRC | MBRS | MBX |
|---|--------|-------------------|--------|-------|
| Aperture separation | 194 mm | 188 mm | 414 mm | - |
| Inner bore diameter | | 69 mm | | 78 mm |
| Nominal current, I_{nom} | 6050 A | | 5850 A | |
| Nominal field strength at I_{nom} | | 3.8 T | | |
| Peak field in the conductor at I_{nom} | | 4.6 T | | |
| Operating temperature | 4.5 K | | 1.9 K | |
| Differential inductance at I_{nom} | 52 mH | | 26 mH | |
| Maximum stored energy | 951 kJ | 890 kJ | 445 kJ | |
| Number of turns | 128 | | 64 | |
| Number of strands in the cable | | 30 | | |
| Magnetic length, l_{mag} | | 9.45 m | | |
| Conductor width | | 9.7 mm | | |
| Conductor height | | 1.17 mm | | |
| Insulation thickness (width) | | 100 μm | | |
| Insulation thickness (height) | | 180 μm | | |
| Cu/SC Ratio | | 1.8 | | |
| Strand twist-pitch | | 0.074 m | | |
| Filament twist-pitch | | 0.013 m | | |

The magnetic field inside the coils of one aperture of the MBRS magnet is shown in Figure 3.15. Due to the same coil geometry, the magnetic field in the other IPD magnets is very similar.

The electrical circuits that contain the IPD magnets consist only of single magnets, with both apertures in series, if present. The electrical circuit is composed of the magnet, ± 8 V, $\pm 6\text{-}8$ kA power converters with their crowbar in parallel, and the

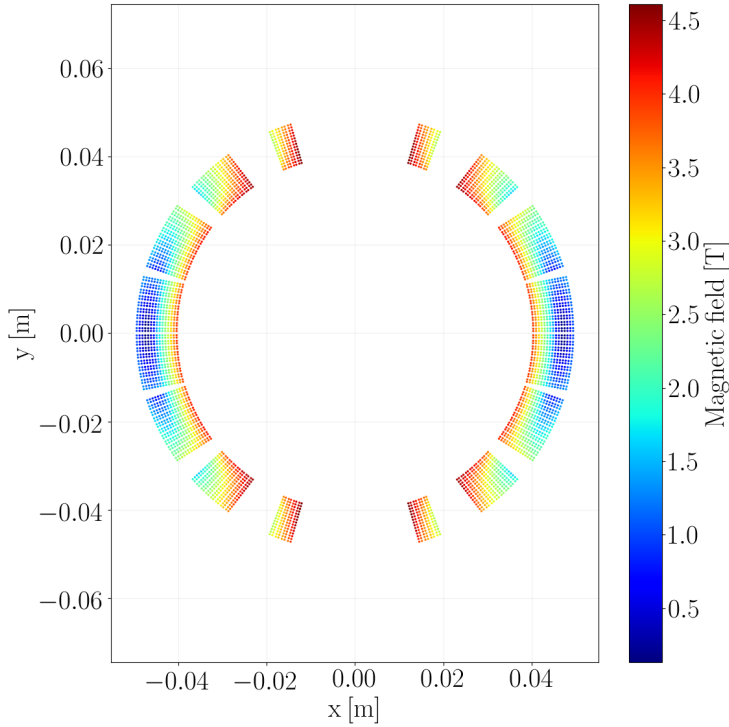


Figure 3.15: Magnetic field in the MBRS coils, calculated using ROXIE [43, 44] and including iron yoke effect

circuit warm resistance [53]. The crowbar of the IPD circuits consists of three redundant branches, each consisting of a $R_{\text{Crowbar}} = 0.056 \text{ m}\Omega$ resistance and a Schottky diode, with a voltage drop $U_{\text{Crowbar}} = 0.34 \text{ V}$. For the sake of simplicity, the redundancy is not taken into consideration in the simulations.

Four quench heater strips are attached to the outside of the magnet coils. One MBRS aperture with the location of its quench heater strips is shown in Figure 3.16. The quench heater strips are 10.16 m long, have a width of 15 mm, a thickness of 25 μm and a stainless-steel to copper ratio of $\frac{l_{\text{QH,SS}}}{l_{\text{QH,Cu}}} = \frac{100 \text{ mm}}{200 \text{ mm}}$. Every 2 strips are connected in series to a unit of 7.05 mF capacitance charged to 900 V, which is triggered in case of quench detection [28]. The expected quench heater peak current $I_{0,\text{QH}}$ [A] can be estimated, following:

$$I_{0,\text{QH}} = \frac{U_{0,\text{QH}}}{R_{\text{Total,QH}}} = 167 \text{ A} \quad (3.6)$$

with $U_{0,\text{QH}}$ [V] the initial charging voltage of the QH capacitors and $R_{\text{Total,QH}}$ [Ω] the total resistance of the strips, including the warm and cold parts. The time constant for the decay of the quench heater current can be calculated with

$$\tau_{\text{QH}} = R_{\text{Total,QH}} \cdot C_{\text{QH}} = 38 \text{ ms} \quad (3.7)$$

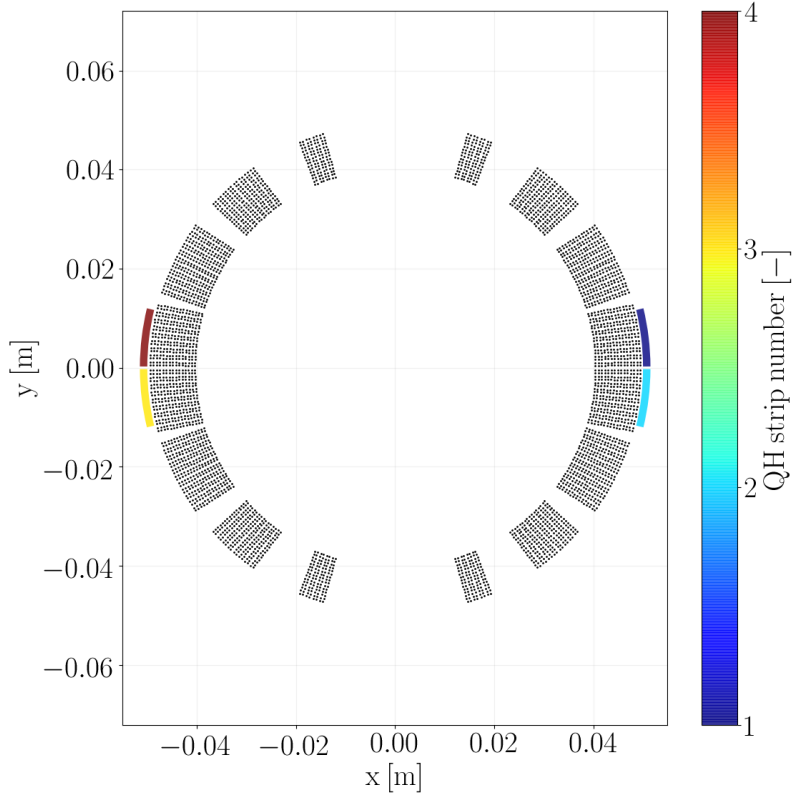


Figure 3.16: Cross-section of one MBRS aperture and the location of their attached quench heater strips. Width of the quench heater strips are increased for the illustration.

As the IPD circuits correspond to the electrical circuit model used in STEAM-LEDET, shown in Figure 2.4 and only contain single magnets, the transients in the magnet and circuit can be simulated simply using STEAM-LEDET. Coupling of an additional electrical circuit model to the electric-magneto-thermal model is not necessary.

3.3.2 Parameter variation and their impact

Similar to the superconducting magnet model of the MCBYH magnet, also the models of the IPD magnets require the determination of unknown parameters during their validation. For this reason, the different IPD magnets will be compared to measurements and evaluated. As all of the magnets were produced by the same manufacturer and use the same type of filaments, strands and cable, it is assumed that the set of parameters has to be equivalent for all magnets of this family. The validation will be conducted with measurements from fast power aborts around nominal current that occurred during LHC operation. At the time $t_{PC} = 0$ s, the power

converter is disconnected from the circuit and the magnet current is discharged. This is mainly achieved by the coil resistance increase due to the transition to the normal state induced by quench heaters, which are fired at $t_{\text{QH}} = 2 \text{ ms}$. However, for the MBX magnet, there is no data around the nominal current available and thus this magnet will be excluded from the validation.

The set of parameters that is investigated with the framework contains the parameters RRR and $f_{\rho,\text{eff}}$. The specification of the fabricator defines a $\text{RRR} > 38$ [21]. Furthermore, as the cables of the IPD magnets are multi-stranded, the effects of the inter-strand coupling currents need to be taken into account. Thus, the cross-contact resistance R_C needs to be investigated. Additionally, the cables of the IPD magnets are not impregnated. Thus they can be infiltrated by the surrounding helium which can significantly influence the cooling. As described in Chapter 2.2.2, the parameter f_{He} will be included in order to model this effect. The first estimation for the helium fraction infiltrating the IPD cables, following the presented equations 2.4-2.8 and using the cable parameter of MBRB, is:

$$f_{\text{He}} = f_{\text{internal Voids}} = \frac{(15 - 1)(2 - 1)}{15 \cdot 2} \cdot \frac{A_{\text{Bare}} - A_{\text{Strands}}}{A_{\text{Ins}}} = 0.044 \approx 4.4\%$$

As the IPD magnets are protected by quench heater, other parameters and factors, such as the initial quench hot-spot and its location, will not be taken into account. In fact, the discharge in the magnet is mostly governed by the quench heater and the impact of the quench propagation between the heating stations of the QH. Thus the initial quench propagation before the quench heater triggering can be neglected. The full set of simulations that was performed for the validation of the magnets MBRB/C/S is shown in Table 6. In total, 1296 simulations per magnet were performed.

Table 6: Simulation summary for the validation of the interaction point dipoles

| Parameter | Number of data points | Range of values | Type |
|--|-----------------------|-----------------------------|-------------|
| RRR | 6 | [35, 200] | Linear |
| $f_{\rho,\text{eff}}$ | 6 | [1, 3] | Linear |
| R_C | 6 | $[10^{-6}, 10^{-3}] \Omega$ | Logarithmic |
| f_{He} | 6 | [0, 6] % | Linear |
| Total number of simulations: 1296 | | | |

All performed simulations for the MBRB magnet and their current transients, compared to a measurement from real-operation, are shown in Figure 3.17.

The selected set of simulations are forming a band around the measurement and are shaping into different branches. These branches are for the faster decays more distinguishable but merge into each other for the slower simulated decays. In general,

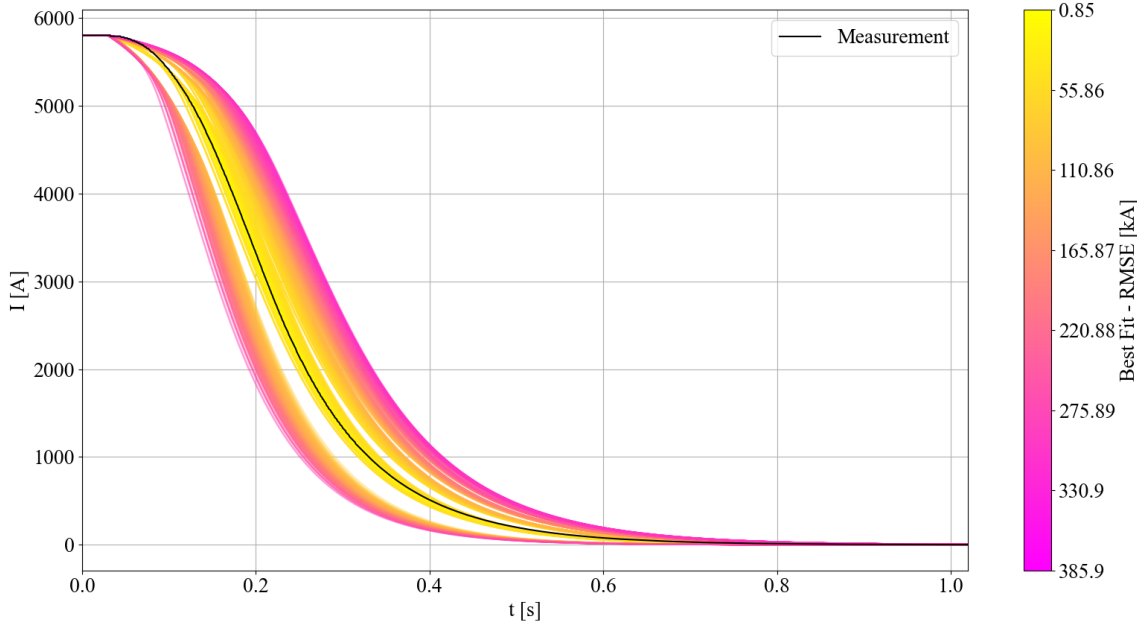


Figure 3.17: Current decay in the MBRB magnet for all performed simulations, compared to measurements, after a fast power abort at $t_{PC} = 0$ s and quench heater firing at $t_{QH} = 2$ ms.

one can observe that multiple simulations show a very good agreement to the measurement. The simulated set of current decays for the other IPD magnets are shown in the Annex, in Figure F.5 for the MBRC and Figure F.6 for the MBRS. Their sets of simulations look very similar to the one of MBRB, shown in Figure 3.17.

In order to obtain better insight into the parameter dependencies of the simulations, the relative quench load error $e_{R,QL}$ is shown for all simulations in Figure 3.18. The color bars indicate the distribution of the parameters across the full set of simulations.

The general relative quench load error is for all simulations below 35%. From Figure 3.18, one can see that the parameter $f_{\rho,\text{eff}}$ does have a rather small effect on the model performance. For the full set (left to right), the error slightly increases. For each set of values for the cross-contact resistance R_C , every 216 simulations, the error does not change and thus the parameter has little to no effect on the simulated transient. However, especially for the parameters f_{He} and RRR one can observe a strong correlation of parameter variation and error. As the parameter set for the IPD magnets is rather large, the first section of 216 simulations from Figure 3.18, is shown enlarged in Figure 3.19.

In general, the error seems to reach a minimum for all simulations, applying a value of $RRR = 68$ or 101 . For larger values, the error significantly increases. Moreover, the error for different values of f_{He} is dependent on the chosen value of RRR. One

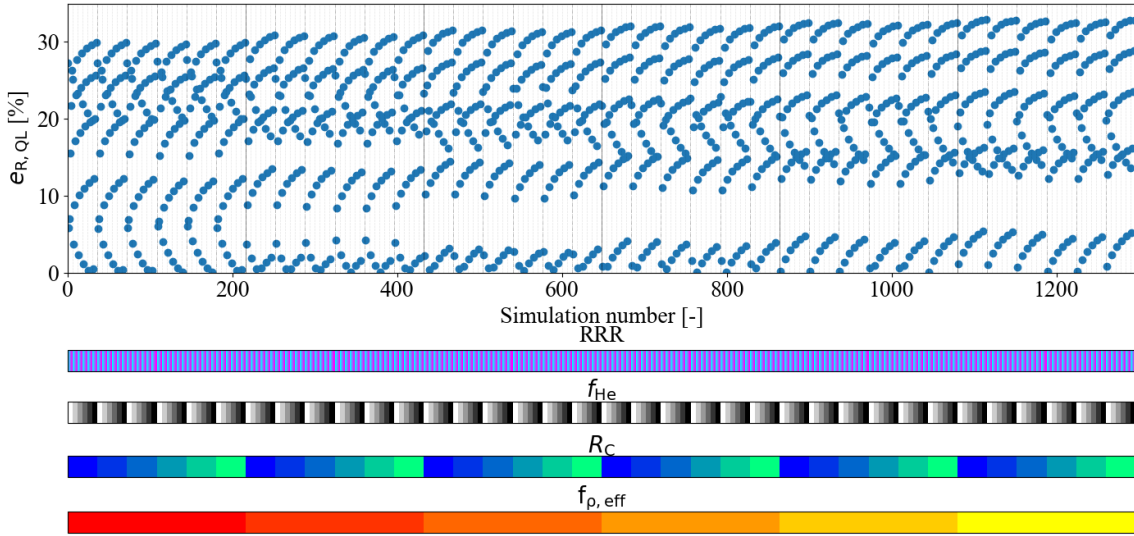


Figure 3.18: Relative difference of the simulated quench loads and measured quench load as a function of simulation numbers for the MBRB magnet

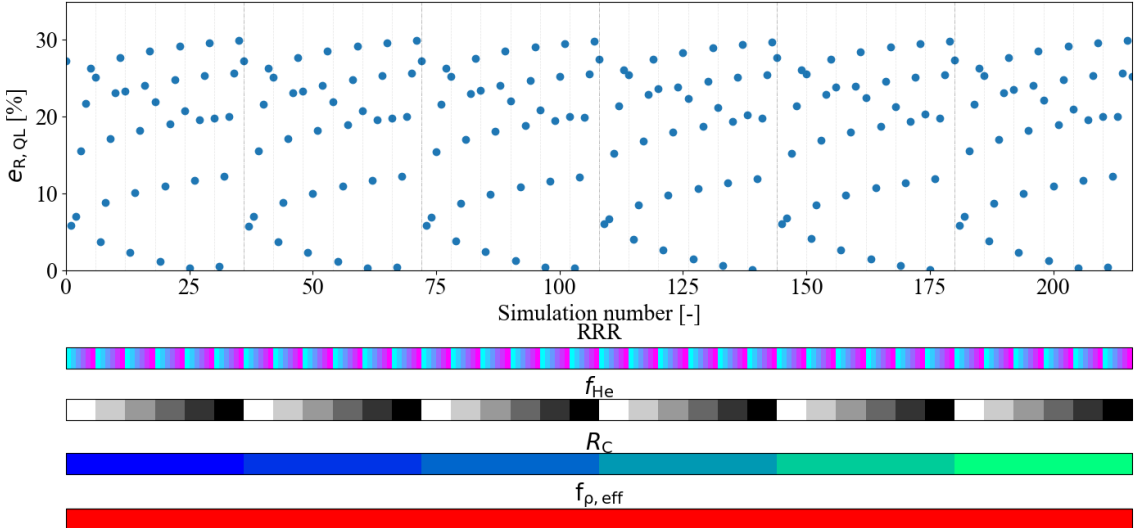


Figure 3.19: Enlarged section of the first 216 simulations and their relative difference of the simulated quench loads and measured quench load for the MBRB magnet

can observe that for the RRR values 35 and 68, the relative quench load difference decreases with increasing value of f_{He} . However, for values of RRR that are larger than 68, the difference is increasing with increasing value of f_{He} . For this magnet family, a variation in the infiltrated helium section can cause a difference in the relative quench load error of up to 10%. The dependencies of the quench load error to the simulation parameters including the parameter distribution for the other two

magnets are shown in the Annex, in Figure F.7 for the MBRC magnet and Figure F.8 for the MBRS.

The best-fitting simulations for all magnets and their error metrics are shown in Table 7. The error metrics are defined in the same way as described in Chapter 3.2.2. The agreement for the best simulations and the measurement is excellent. The relative quench load error is for all selected simulations below $<3\%$ and can even go down for the MBRB magnet to less than 0.1%. Also, the maximum absolute difference between measurement and simulation is below 200 A, which corresponds to a maximum relative error of less than $<3.5\%$ with respect to the initial current. One can observe that the fitting is better for the MBRB magnet. For the MBRB magnet, the maximal relative error with respect to the initial current is even below $<1.5\%$.

Table 7: Obtained errors and quench loads for the selected best and worst simulations in the set of conducted simulations.

| Simulation number | $f_{\rho,\text{eff}}$ | R_C [Ω] | f_{He} [%] | RRR | RMSE [A] | $\max(e)$ [A] | QL [MA^2s] | $e_{\text{R},\text{QL}}$ [%] |
|---|-----------------------|---------------------|---------------------|-----|----------|-----------------|------------------------------|------------------------------|
| MBRB, $QL_{\text{MBRB, Meas}} = 5.926 \text{ MA}^2\text{s}$ | | | | | | | | |
| 265 | 1.4 | $4 \cdot 10^{-6}$ | 1.2 | 68 | 29.1 | 75.2 | 5.89 | 0.51 |
| 1045 | 2.6 | $1 \cdot 10^{-3}$ | 0 | 68 | 31.6 | 79.6 | 5.92 | 0.06 |
| 475 | 1.8 | $4 \cdot 10^{-6}$ | 1.2 | 68 | 30.0 | 83.2 | 5.93 | 0.08 |
| MBRC, $QL_{\text{MBRC, Meas}} = 6.545 \text{ MA}^2\text{s}$ | | | | | | | | |
| 152 | 1 | $6 \cdot 10^{-5}$ | 1.2 | 101 | 70.0 | 171.9 | 6.54 | 0.07 |
| 254 | 1.4 | $4 \cdot 10^{-6}$ | 0 | 101 | 74.7 | 183.7 | 6.54 | 0.01 |
| 182 | 1 | $1 \cdot 10^{-3}$ | 0 | 101 | 64.2 | 140.8 | 6.43 | 1.71 |
| MBRS, $QL_{\text{MBRS, Meas}} = 5.271 \text{ MA}^2\text{s}$ | | | | | | | | |
| 145 | 1 | $2.5 \cdot 10^{-4}$ | 0 | 68 | 44.8 | 112.3 | 5.34 | 1.39 |
| 109 | 1 | $6 \cdot 10^{-5}$ | 0 | 68 | 46.9 | 117.4 | 5.35 | 1.54 |
| 181 | 1 | $1 \cdot 10^{-3}$ | 0 | 68 | 48.9 | 121.8 | 5.36 | 1.75 |

As mentioned, poses the mutual fabrication of the IPD magnets, the restriction, that the same set of parameters has to be applied. The proposed parameter set for the IPD magnets, based on the performed simulations is thus: $\text{RRR} \in [68, 100]$, $f_{\text{He}} \in [0,1] \%$, $f_{\rho,\text{eff}} \in [1,2]$ and $R_C \in [1 \cdot 10^{-3}, 1 \cdot 10^{-5}] \Omega$. However, the last parameter has little effect on the model performance. This parameter set seems to show the best result for all IPD magnets. Furthermore, it also follows the specifications given for the magnets. However, the obtained value for the infiltrated helium fraction seems to be lower than initially expected, when it was assumed that all internal voids are filled with helium. In fact, the best results assume only little to no infiltrated helium. The proposed parameter set is also used to conduct an ablation analysis, assessing the sensitivity of the model towards changes in these parameters. The impact on the

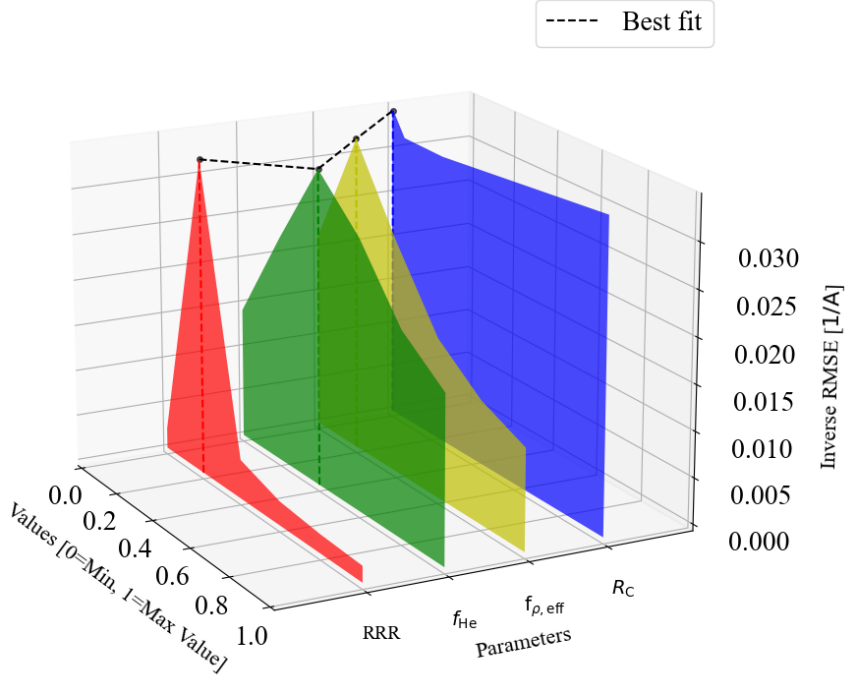


Figure 3.20: Ablation analysis of the MBRB model to the selected parameter. Dependency of the inverse RMSE to changing one parameter at a time. If not changed, values are fixed to $RRR = 68$, $f_{\rho, \text{eff}} = 1.4$, $f_{He} = 1.2\%$ and $R_C = 4 \cdot 10^{-6} \Omega$.

inverse RMSE due to the change of one parameter at a time for the MBRB magnet model is shown in Figure 3.20.

The largest impact on the model can be observed for RRR. Changing the parameter can drastically increase the general error between simulation and measurement. The current transients for the different chosen values of RRR, compared to the measurement, can also be seen in Figure 3.21. Moreover, different values for RRR do impact the full discharge.

Also the parameters f_{He} and $f_{\rho, \text{eff}}$ can impact the current decay in the simulation. From the chosen, best parameters, the error between simulation and measurement can increase by a factor of two. Their effect can be seen in more detail in Figure 3.22 for the infiltrated helium fraction and in Figure 3.23 for the scaling factor of the effective transverse resistivity. Both parameters mostly impact the discharge from $t \approx 100$ ms onwards. At the beginning of the transient, the discharge is mostly governed by the quench heaters, which are not impacted by these parameters. By the time the quench propagation through the insulation, into neighboring turns as well as coupling losses start to develop, these factors become more important. However, as the operating temperature of the three validated IPD magnets is 4.5 K, the impact of the helium is smaller. For a lower operational temperature, this effect becomes

3.3 VALIDATION OF THE LHC SEPARATION AND RECOMBINATION MAGNET MODELS

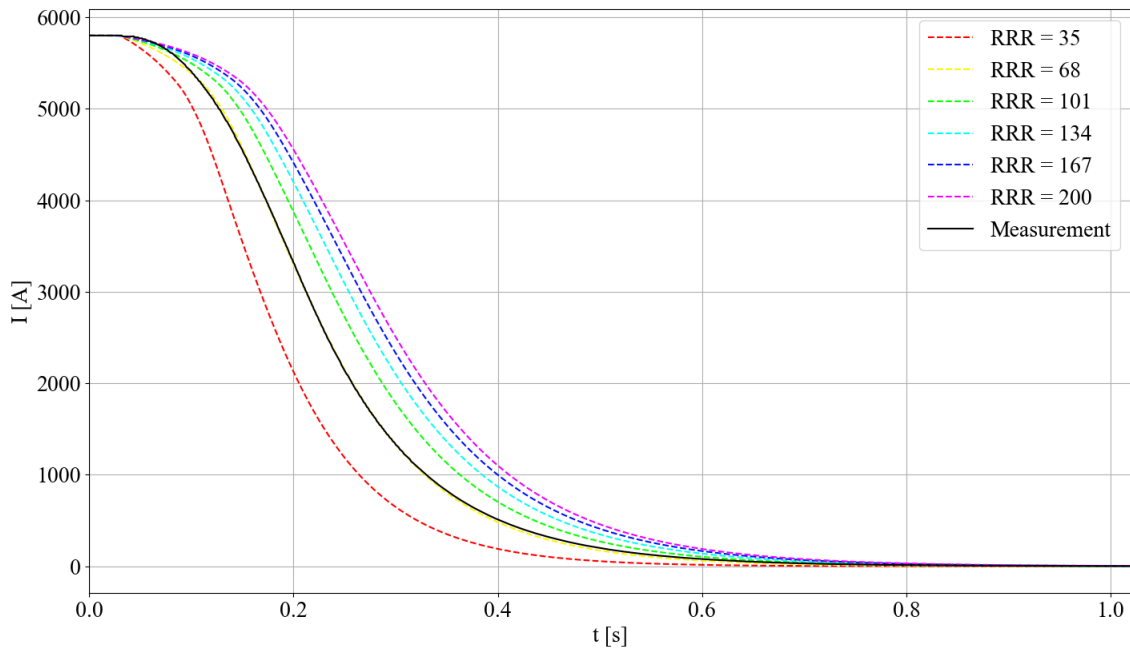


Figure 3.21: Simulated current decays for various values of RRR in the MBRB magnet model, compared to a measurement. $f_{\rho,\text{eff}} = 1.4$, $f_{\text{He}} = 1.2\%$ and $R_C = 4 \cdot 10^{-6} \Omega$ are fixed.

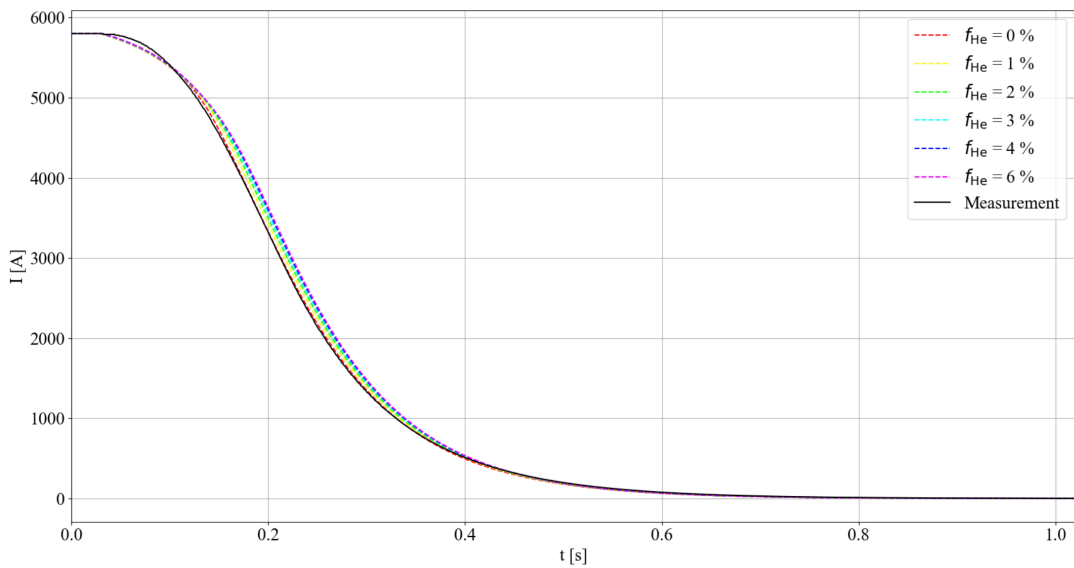


Figure 3.22: Simulated current decays for various values of f_{He} in the MBRB magnet model, compared to a measurement. $f_{\rho,\text{eff}} = 1.4$, $\text{RRR} = 68$ and $R_C = 4 \cdot 10^{-6} \Omega$ are fixed.

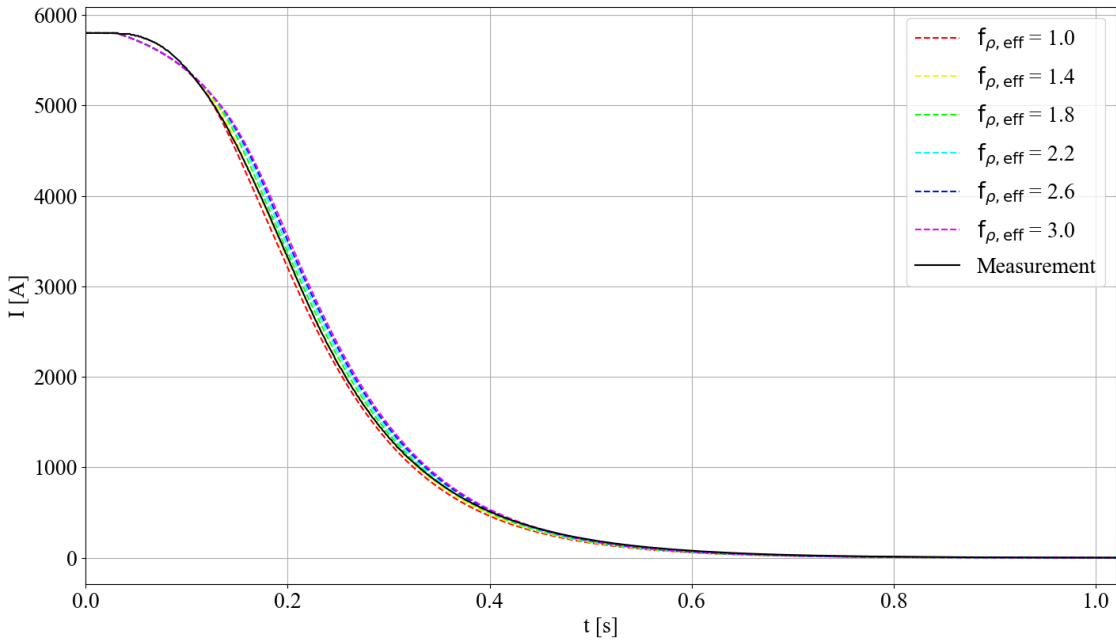


Figure 3.23: Simulated current decays for various values of $f_{\rho,\text{eff}}$ in the MBRB magnet model, compared to a measurement. $f_{\text{He}} = 1.2\%$, $\text{RRR} = 68$ and $R_C = 4 \cdot 10^{-6} \Omega$ are fixed.

more important in the model.

Furthermore, Figure 3.20 shows that varying the cross-contact resistance basically has no effect on the model. This can also be observed in Figure 3.24 which shows the current decays for the different applied values. The inter-strand coupling currents in the discharge of the IPD magnets are still rather small, as the heat propagation from turn to turn as well as inter-filament coupling currents develop faster and thus cause the transition to normal state. However, for other magnets, the cross-contact resistance might impact the discharge more strongly. The ablation analyses for the other two magnets are shown in Figure F.9 (MBRC) and F.10 (MBRS).

Finally, in Figure 3.25 the best fitting simulations in terms of the quench load error are directly compared to the measured current decays (Figure 3.25a) and to the experimental coil-resistance (Figure 3.25b). One can see that the agreement between the simulated and measured currents, using only slightly different parameters, is very good in all cases. Also, the simulated and experimental coil-resistances show good agreement. However, especially for MBRS, there is a small difference at the beginning of the transient. The final values for all three magnets yield a quench load error of less than 5%. The best simulations and the used parameter values are summarized in Table 8.

The framework provides a fast and easy possibility to conduct a large number of simulations, which also makes it possible to rapidly validate a whole family of magnets.

3.3 VALIDATION OF THE LHC SEPARATION AND RECOMBINATION MAGNET MODELS

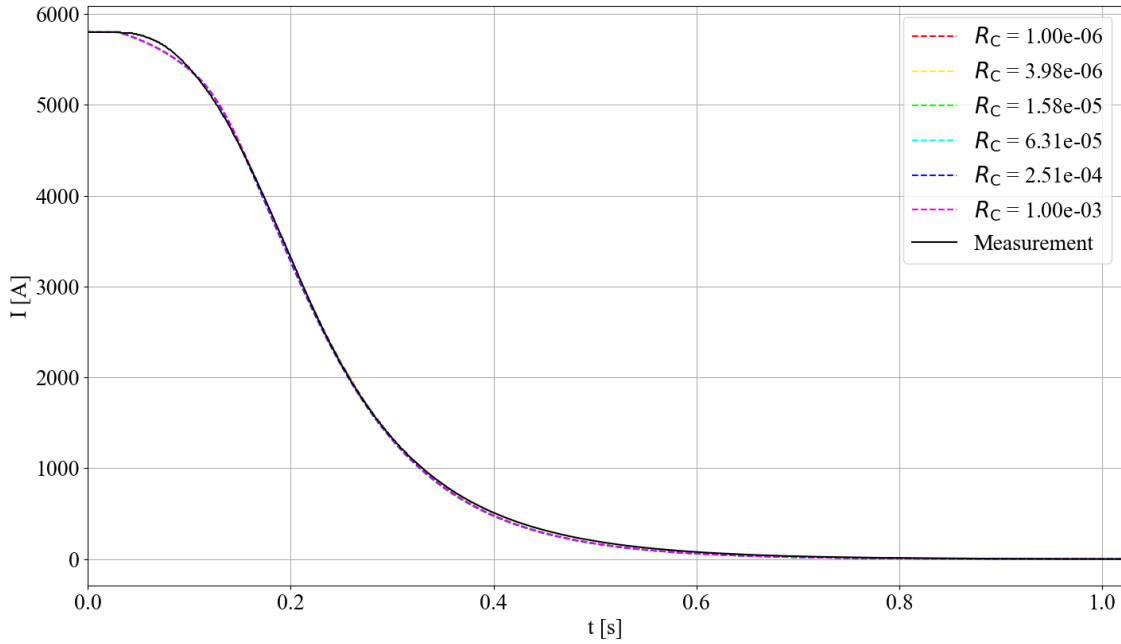
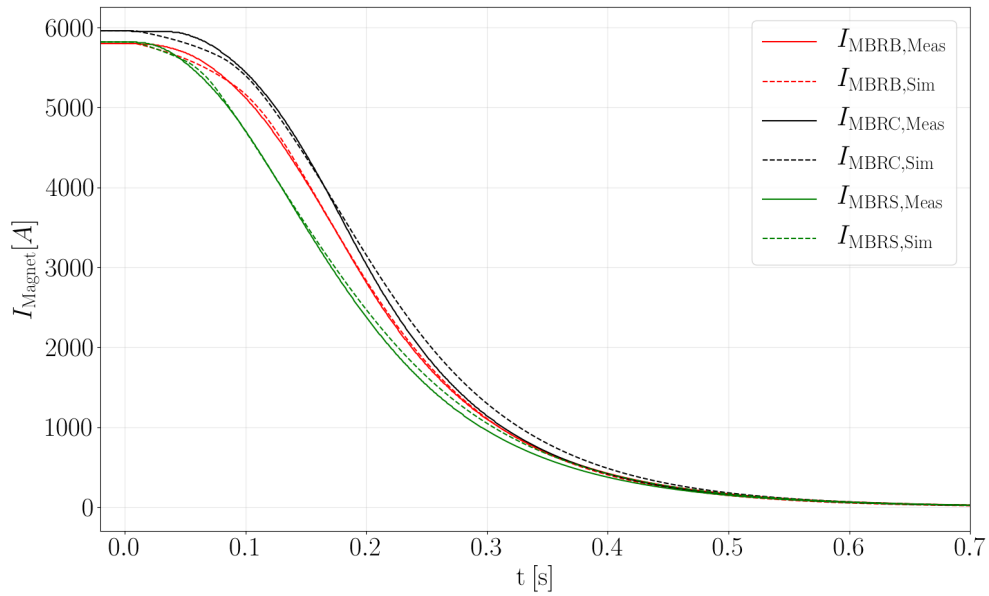


Figure 3.24: Simulated current decays for various values of f_{He} in the MBRB magnet model, compared to a measurement. $f_{\rho,\text{eff}} = 1.4$, $\text{RRR} = 68$ and $f_{\text{He}} = 1.2\%$ are fixed.

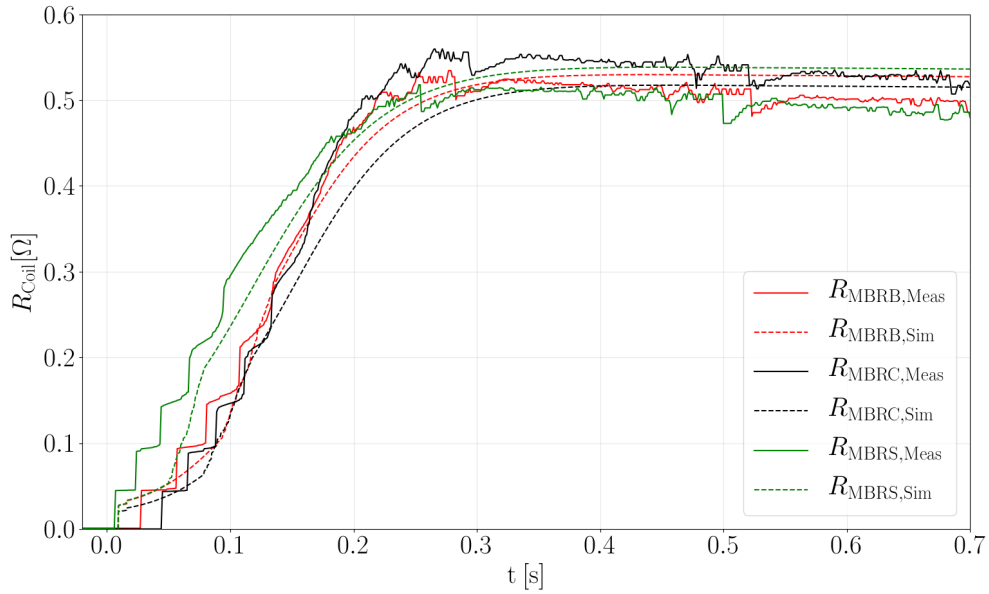
In total, about 5000 simulations were performed. For the IPD magnets, a very good agreement between measurements and simulations was found, while all restrictions and requirements on the parameters were fulfilled.

Table 8: Summary of the best fitting parameter values for the IPD magnets with respect to the quench load error.

| Magnet | $f_{\rho,\text{eff}}$ | $R_C [\Omega]$ | $f_{\text{He}} [\%]$ | RRR |
|--------|-----------------------|-------------------|----------------------|-----|
| MBRB | 1.4 | $6 \cdot 10^{-5}$ | 1.2 | 68 |
| MBRC | 1.4 | $6 \cdot 10^{-5}$ | 0 | 101 |
| MBRS | 1 | $6 \cdot 10^{-5}$ | 0 | 68 |



(a) Comparison of simulated and measured current decay in the IPD magnets MBRB/C/S.



(b) Comparison of simulated and experimental coil-resistance in the IPD magnets MBRB/C/S.

Figure 3.25: Comparison of measurements and best fitting simulations for the current decay (a) and coil resistance (b). Chosen simulations are MBRB (Simulation number 1045), MBRC (254) and MBRS (145).

4 Automatic simulation of future events in LHC superconducting circuits

Once a superconducting magnet model is validated it can be utilized for further analysis, for example, to investigate the behavior regarding physical phenomena or regarding different events or operation scenarios. The newly developed framework is effective for this purpose as some of these analyses require running a large set of simulations.

Two use-cases will be presented. First, the prediction of the so-called quench-back current in the 600 A LHC superconducting circuits is shown in Chapter 4.1. Second, in Chapter 4.2 the prediction of the impact of different initial quench locations in a self-protecting 120 A superconducting magnet, the MCBYH magnet that was also already validated using this framework, is discussed. The implementation of the analyses will be described within each Chapter.

4.1 Predicting the occurrence of quench-back

The phenomenon called quench-back is a quench due to passive effects, such as coupling losses, following a primary natural quench or an energy-extraction. Once a quench starts to evolve in the magnet, the heat and normal zone are propagating throughout the coil winding pack, causing more turns to transfer into normal state and thus also causing an increasing absolute current derivative. As described in Chapter 1.2.3, due to the local field change, coupling currents are induced in the magnet conductors. In some magnets, these losses are so high that they can cause some turns to quench. This is described as quench-back phenomenon. Turns that carry the same current and are exposed to a similar field, also show similar losses. Thus, at some point, not only a single turn, but multiple turns are transferring to the normal state simultaneously, or in rapid succession. Moreover, as the coupling losses are developed nearly uniformly along the direction of the transport current, it can be assumed that the full magnetic length of a turn quenches simultaneously. This sudden transition of coil sections can cause a steep increase in the resistance and hence an increase of the absolute current derivative.

Quench-back can sometimes specially shape the transients in superconducting magnets. The occurrence might indicate if the specific magnet is behaving as supposed or deviates from its expected transient. With respect to the quench-back, the 600 A magnet family is interesting to analyze as not all magnets show quench-back and those that show it do so at different current levels. The initial current above which quench-back occurs during a fast power abort will be here referred to as the 'quench-back current' $I_{\text{Quench-back}}$ [A]. This current is a function of the coils conductor type, the peak field in the coil as well as the discharge time constant.

Without any prior knowledge about this, it is thus not easy to determine if one of the 600 A magnets is supposed to show quench-back at a given current level. Observing

an unexpected quench-back in a magnet could indicate the need for a more detailed analysis of a specific transient event.

In Chapter 4.1.1 the 600 A circuit and magnet family is shortly presented. Afterwards, Chapter 4.1.2 describes how the analysis was performed and discusses the results.

4.1.1 LHC 600 A circuits

The LHC 600 A circuits and their magnets are one of the most numerous circuit families of the LHC. In total, this family consists of 408 circuits which are distinguished into 28 different circuit types. These circuit types contain a different number of magnets, ranging from single magnets in the circuit to 154 series-connected magnets. Moreover, they include 12 different magnet types which range from quadrupoles to decapoles. The generalized electrical circuit schematic is shown in Figure 4.1. Note that not all LHC 600 A circuits include an EE system for protection or parallel resistors across their magnets.

All LHC 600 A circuits and some of their properties are summarized in Table 9. More information about the magnets can be found in Table 18.

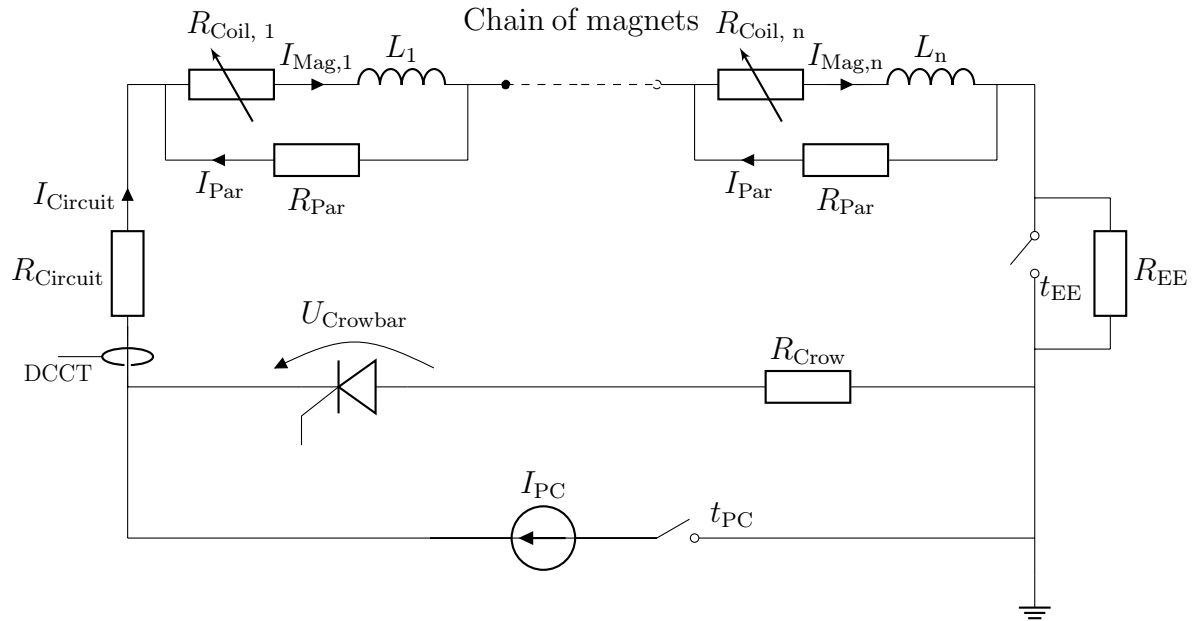


Figure 4.1: Generalized electrical circuit schematic of the LHC 600 A circuits. The parallel resistor R_{Par} and the energy extraction system are not present in all circuits (see Table 9). Nominal current $I_{\text{Nom}} = 550 \text{ A}$ and $R_{\text{Crow}} = 50 \text{ m}\Omega$. Energy extraction system is simplified. Circuit current is measured in the DCCT (Direct current-current transformer)

Table 9: Summary of some properties of the LHC 600 A circuits and their protection [1, 21]. Magnets marked with the same upper indice number are nested into each other. Magnets marked with * include nested magnets, not listed in the LHC 600 A circuits.

| Circuit type name | Magnet | Number of magnets | L_{Circ} [H] | Energy extraction | Parallel resistor R_{Par} [Ω] |
|-------------------|----------------------|-------------------|-----------------------|-------------------|---|
| RCS | MCS | 154 | 0.123 | EE, 0.7 Ω | 0.08 |
| RQ6 | MQTLH | 6 | 0.72 | EE, 0.7 Ω | 0.2 |
| RQS.AxxBxx | MQS | 4 | 0.124 | EE, 0.7 Ω | 0.25 |
| RQTD/F | MQT | 8 | 0.248 | EE, 0.7 Ω | 0.25 |
| RQTL9 | MQTLI | 2 | 0.240 | EE, 0.4 Ω | 0.2 |
| RSD | MS | 12 | 0.432 | EE, 0.7 Ω | 0.15 |
| RSD | MS | 11 | 0.396 | EE, 0.7 Ω | 0.15 |
| RSF | MS | 10 | 0.360 | EE, 0.7 Ω | 0.15 |
| RSF | MS | 9 | 0.324 | EE, 0.7 Ω | 0.15 |
| RCD | MCD* | 77 | 0.031 | EE, 0.7 Ω | - |
| ROD | MO | 13 | 0.021 | EE, 0.7 Ω | - |
| ROD | MO | 8 | 0.013 | EE, 0.7 Ω | - |
| ROF | MO | 13 | 0.021 | EE, 0.7 Ω | - |
| ROF | MO | 8 | 0.013 | EE, 0.7 Ω | - |
| RSS | MSS | 4 | 0.144 | not present | 0.15 |
| RQS.L/RxBx | MQS | 2 | 0.062 | not present | 0.25 |
| RQT12 | MQT | 1 | 0.031 | not present | 0.25 |
| RQT13 | MQT | 1 | 0.031 | not present | 0.25 |
| RQTL7 | MQTLI | 1 | 0.120 | not present | 0.2 |
| RQTL8 | MQTLI | 1 | 0.120 | not present | 0.2 |
| RQTL10 | MQTLI | 1 | 0.120 | not present | 0.2 |
| RQTL11 | MQTLI | 1 | 0.120 | not present | 0.2 |
| RCBXH1/2 | MCBXH ¹ | 1 | 0.287 | not present | - |
| RCBXV1/2 | MCBXV ¹ | 1 | 0.175 | not present | - |
| RCBXH3 | MCBXH ^{2,*} | 1 | 0.287 | not present | - |
| RCBXV3 | MCBXV ^{2,*} | 1 | 0.175 | not present | - |
| RQSX | MQSX | 1 | 0.014 | not present | - |

The nominal current for all 600 A circuits is $I_{\text{Nom}} = 550$ A with an ultimate current of $I_{\text{ultimate}} = 600$ A. One characteristic of some 600 A circuits is the resistor R_{Par} in parallel to each magnet of the chain. These parallel resistors cause two drops in the circuit current I_{Circuit} , which is measured before the chain of magnets with a direct

current-current transformer (DCCT). First, when the power supply is disconnected from the circuit, the current starts to flow through the crowbar. Second, when the energy extraction switch is opened (if present). In both cases, the resistance in the path of the DCCT (and hence through the crowbar and EE) increases and thus the current, which is pushed backwards through these parallel resistances, increases too. These parallel resistors are, among other purposes, used as additional protection to limit the peak temperatures in the magnets.

For analysis, the factor f_{\parallel} [-] is defined, describing the fraction of the magnet current flowing through the DCCT:

$$f_{\parallel} = \frac{I_{\text{Circuit}}}{I_{\text{Mag}}} = \frac{\sum R_{\text{par}}}{\sum R_{\text{par}} + R_{\text{EE}} + R_{\text{Crow}}} \quad (4.1)$$

If an energy extraction is present in the circuit, the EE switches open with a slight delay of usually about 8 ms. The current discharge afterwards is largely defined by the EE resistance. In the cases where no EE system is present, the stored energy is discharged in the magnet coils, in the parallel resistors (if present), in the power-converter crowbar, and in the warm circuit resistance.

The parallel resistors in the circuits have a significant impact on the current in the magnets and are not included in STEAM-LEDET. Hence, the 600 A circuits with a parallel resistor require to be simulated with a more complex simulation. In this study, the analysis was performed with the STEAM-COSIM tool, coupling the electrical circuit PSPICE[©] model and the electrical magneto-thermal STEAM-LEDET magnet model in a co-operative simulation. The models that were used for these simulations were previously validated and showed good agreement with measurements. As the simulations for some of the 600 A circuits require the set-up of STEAM-COSIM models, the implementation needs to be adjusted. Another dedicated notebook was used to prepare and set up the simulations. First, an Excel file was set up containing all required information about all 600 A circuits, such as all values for the electrical components, shown in Figure 4.1, as well as which type of simulation to set up (LEDET stand-alone or COSIM). The STEAM-LEDET stand-alone simulations are set up in the same manner described in Chapter 3.1. Instead, the COSIM models require more steps. First, the structure of the directories for the co-operative simulations is set up, followed by the writing of all port- and configuration files. These files include the user-specific paths for the solvers (e.g. STEAM-LEDET and PSPICE[©]) as well as all ports, names and coupling parameters. User-specific information needs to be provided in a .yaml file. Afterwards, the reference simulation files for the electrical circuit and the magnet model are tailored so they include all the provided information for the specific circuit. Furthermore, also the stimuli for the power supply and other circuit components are written in a PSPICE[©] .stl file. If additional stimuli (for example for EE) need to be included, they can be provided in the set-up. In the end, all the files are combined in the prepared folder structure and a batch file is written, which includes the execution commands for all simulations.

In this way, the user can execute the whole set of simulations with 'one-click'. A short coding example is given in the Annex in Listing 2.

4.1.2 Prediction of quench-back current in LHC 600 A circuit

The general approach to predict the quench-back current in the 600 A circuits is overall relatively simple. The model of each circuit is run at different current levels between 100 A and their ultimate current of 600 A and the results are analyzed with particular focus on the eventual occurrence of quench-back. The current levels are pre-defined as follows:

$$100 \text{ A}, 200 \text{ A}, 300 \text{ A}, 350 \text{ A}, 400 \text{ A}, 450 \text{ A}, 500 \text{ A}, 550 \text{ A}, 600 \text{ A}$$

These are arranged in 100 A steps, redefined from 300 A in 50 A steps, as it is expected to have a quench-back current of $I_{\text{Quench-back}} \geq 300 \text{ A}$. Furthermore, in order to also analyze the impact of an occurring quench, all simulations were performed twice, i.e. with or without an initial quench.

Within the framework, the model of each circuit is adjusted such that the correct values for the circuit warm resistance R_{Circuit} , parallel resistor R_{Par} and energy extraction R_{EE} are applied. The model is then prepared, depending on which tools need to be used and the simulations are run assuming the different described current levels.

Due to a large number of different circuit types within the 600 A circuit family, only a selected number of them will be shown in more detail within this thesis. However, the prediction results of all circuit types are shown in Table 10. Table 10 shows the stored energy in each circuit, the coil volume of a single magnet in the circuit as well as the time discharge constant $\tau_{\text{Discharge}}$ [ms], f_{\parallel} and the expected quench-back current. Furthermore, also the significance of the quench-back is evaluated by comparing the simulated quench loads with and without occurring quench-back. Some circuits show lower quench-back significance as the current discharge of these circuits is almost not affected. On the contrary, in circuits with a higher quench-back significance, the moment of the occurrence of quench-back is clearly visible and the quench load is significantly reduced, compared to a discharge without quench-back. Both, the quench-back current and the reduction of the quench load due to quench-back, are with respect to the simulations without an initial quench. This results in a total of 504 performed simulations.

In order to have a closer look at the simulations, Figure 4.2 shows the current discharge for the different current levels, for the simulations with and without an initial quench, in an RSD circuit (compare Table 10).

Table 10: Quench-back prediction results for the different 600 A circuit types, including further information about the discharge and circuits [1].

| Circuit type name | Stored energy [kJ] | Coil volume [m ³] | Discharge time constant $\tau_{\text{Discharge}}$ [ms] | f_{\parallel} | $I_{\text{Quench-back}}$ [A] | Reduction of quench load |
|-------------------|--------------------|-------------------------------|--|-----------------|------------------------------|--------------------------|
| RCS | 22.1 | 0.05 | 40 | 0.94 | Not expected | |
| RQ6 | 86.4 | 1.7 | 960 | 0.62 | 300-350 | 30 - 75 % |
| RQS. AxxBxx | 22.3 | 0.47 | 170 | 0.57 | 300-350 | 10 - 35 % |
| RQT-D/F | 44.6 | 0.47 | 330 | 0.73 | 450-500 | 50 - 75 % |
| RQTL9 | 43.2 | 1.7 | 530 | 0.47 | 450-500 | 50 - 75 % |
| RSD | 77.8 | 0.75 | 580 | 0.71 | 350-400 | 50 - 80 % |
| RSD | 71.3 | 0.75 | 530 | 0.69 | 350-400 | 50 - 80 % |
| RSF | 64.8 | 0.75 | 480 | 0.67 | 350-400 | 50 - 80 % |
| RSF | 58.3 | 0.75 | 430 | 0.64 | 350-400 | 50 - 80 % |
| RCD | 5.6 | 0.05 | 40 | 1 | 100-200 | 0 - 5 % |
| ROD/F | 3.6 | 0.18 | 30 | 1 | 100-200 | 0 - 5 % |
| ROD/F | 3.1 | 0.18 | 20 | 1 | 100-200 | 0 - 5 % |
| RSS | 25.9 | 0.75 | 2880 | 0.92 | Not expected | |
| RQS. L/RxBx | 11.2 | 0.47 | 1240 | 0.91 | 450-500 | 50 - 75 % |
| RQT12 | 5.6 | 0.47 | 620 | 0.83 | 350-400 | 60 - 80 % |
| RQT13 | 5.6 | 0.47 | 620 | 0.83 | 350-400 | 60 - 80 % |
| RQTL7 | 21.6 | 1.7 | 2400 | 0.8 | Not expected | |
| RQTL8 | 21.6 | 1.7 | 2400 | 0.8 | Not expected | |
| RQTL10 | 21.6 | 1.7 | 2400 | 0.8 | Not expected | |
| RQTL11 | 21.6 | 1.7 | 2400 | 0.8 | Not expected | |
| RCBXH | 31.5 | 1.17 | 5740 | 1 | 400-450 | 50 - 75 % |
| RCBXV | 2.5 | 0.95 | 3500 | 1 | 300-350 | 30 - 60 % |
| RQSX | 51.7 | 0.28 | 280 | 1 | 200-300 | 25 - 50 % |

At the beginning of the fast transients, the discharges at all current levels show the characteristic behavior of the 600 A circuits with parallel resistors. After the power supply is disconnected from the circuit and the current is forced through the crowbar, one can observe a small step in the currents at all current levels. Due to the small resistance in the crowbar, some of the current is pushed backwards through the parallel resistors and thus can not be measured by the DCCT, which is effectively

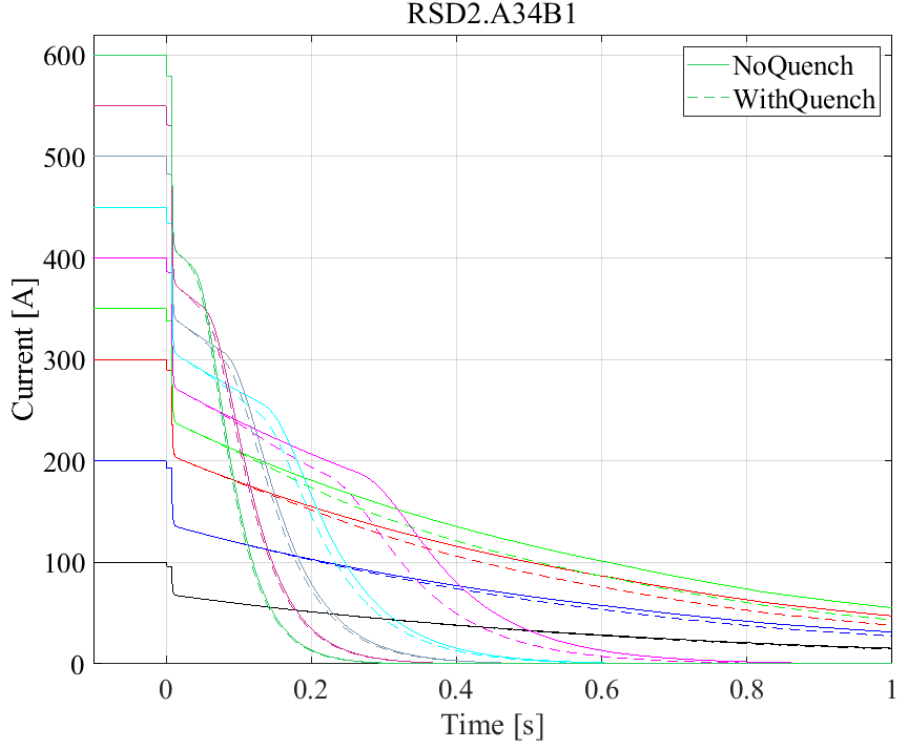


Figure 4.2: Simulated current discharge on different level in the RSD2.A34B1 circuit, after the power supply is switched off at $t_{PC} = 0$ s, for the simulations with and without an initial quench, representing a case with 'high' quench-back significance.

in series to the crowbar. The second, larger step comes shortly after $t_{EE} = 0.008$ s, when the energy extraction triggering suddenly includes 0.7Ω into the discharge path, i.e. effectively in series to the crowbar. Afterwards, a fraction f_{\parallel} of the magnet current flows through the crowbar and EE resistances, while the remaining $(1 - f_{\parallel})$ fraction flows through the parallel resistor. For the lower current level in Figure 4.2 this decay is very similar to an exponential decay. Instead, for current levels larger or equal to 400 A, one can observe that after some time the decay suddenly accelerates. For a current of 400 A, the quench-back starts at about 280 ms. For higher currents, this gradually shifts earlier. A fast power abort at ultimate current of 600 A causes a quench-back at about 50 ms. The quench-back thus decreases the total time of the discharge significantly. The quench load in this circuit is reduced by 50 - 80%, depending on the current level.

Moreover, one can inspect the impact of an initial quench before t_{PC} in the simulation. For the lower current levels, the effect of an initial quench is rather negligible. The effect of the initial quench increases with the current, as the temperatures and resistances rise more quickly. Once the quench-back occurs earlier (e.g. from a current level of about 500 A), the turns in the magnet are mostly quenched because of

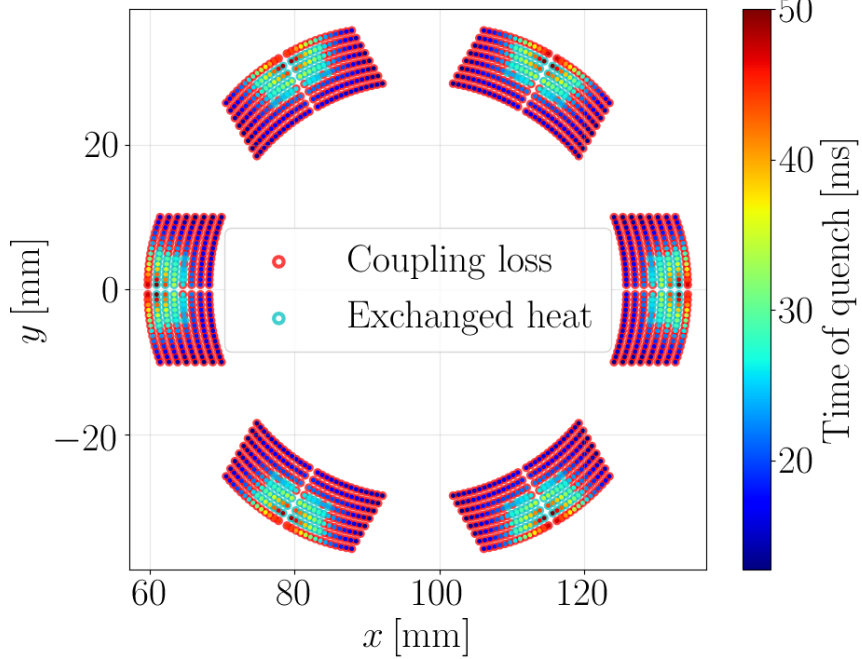


Figure 4.3: Time and cause of quench in each half-turn of one MS magnet aperture in the RSD circuit during a fast power abort transient at $t_{PC} = 0$ s from $I_{PC} = 550$ A. Causes refer to turns, either quenched by coupling losses or to turns, quenched by heat diffusion through insulation or electrical connections.

the quench-back and less because of thermal heat propagation. Thus, the difference between the simulation with and without an initial quench becomes small again. The largest impact of an initial quench in the simulation can be observed for a current level of 400 A.

In the transients in Figure 4.2 it is clearly visible at which moment most of the magnets coil-turns transfer into normal state due to coupling loss, as the current decay changes abruptly. The impact of the quench-back is thus assessed as high, as the discharge is significantly impacted and the quench-load highly reduced. However, for other circuits, quench-back can have a much smaller influence and the quench-load is much less reduced. Examples of circuits with a 'medium' (Figure G.11) and 'low' quench-back influence (Figure G.12) are shown in the Annex. In the case of a low quench-back significance, the occurrence is almost not visible from the current discharge and the quench load is only reduced by about 0-5%. Only a closer inspection of the causes of quench indicate an occurring quench-back.

Moreover, in Figure G.13 in the Annex, a case of no-expected quench-back is shown. In the simulations without an initial quench, the current simply decays pseudo-exponentially and no turns are quenched by coupling losses. However, for this circuit quench-back does occur if a quench is assumed before t_{PC} . This can be

explained by the developed resistance in the quenching coil which is sufficient to induce a current change, and hence magnetic-field change, causing quench-back.

In Figure 4.3 one aperture of one MS magnet in the RSD circuit and the time and causes of quench of all half-turns during an FPA are shown. The circles in Figure 4.3 indicate the cause of quench. For the MS magnet, they are either quenched due to inter-filament coupling loss (i.e. quench-back) or due to heat diffusion from other quenched turns. One can see that in the MS magnet in this FPA most of the turns are quenched by coupling loss. These are first the turns at a higher field. The magnetic field in one aperture of the MS magnet can be seen in the Annex in Figure G.14. Only a few turns in the midplane, between the poles, that show a lower magnetic field and thus are subject to lower coupling loss and have a larger margin to quench, are quenched by the diffused heat from their neighboring turns.

Furthermore, one can observe that the turns in the higher field areas of the magnet aperture are all quenching almost at the same time, at around 15-20 ms. Afterwards, the temperature in these turns starts to rise quickly and thus their resistance too.

This Chapter provides information about the quench-back in the various LHC 600 A circuits and can assist in the assessment of transients by comparing the validated reference transients from the simulations with new measurements.

4.2 Analyzing the impact of different quench locations in the example of self-protecting magnets

Another interesting use case for the developed framework is the prediction of the impact of different quench locations on the quench transients. In most LHC magnets, quenches in the superconducting magnets are detected by measuring the voltage across the magnets and/or comparing the voltage across apertures. These so-called voltage taps allow detecting a quench once the voltage exceeds a pre-defined threshold. However, as the voltage is measured across the whole magnet, it is not possible to deduce in which part of the magnet the quench occurred and whether the measured transient actually belongs to a 'healthy' magnet or might show signs of faults. The initial quench location does not impact significantly the transient in some types of LHC magnets. This is the case of magnets that are protected by QH which quickly quench a significant number of turns or magnets whose turns are quickly quenched by coupling losses (see Chapter 4.1.2 for some examples of quench-back). On the contrary, the class of self-protecting superconducting magnets is impacted significantly by the initial quench location, as these magnets largely depend on the heat diffusion within the coil winding pack for their protection. One example of such a magnet is the MCBYH magnet presented in Chapter 3.2.

In order to assess and investigate the impact of different quench locations, the framework is utilized to perform a series of simulations with initial quench locations throughout the coil. In Chapter 3.2, in the scope of the validation of the MCBYH magnet, 8 different locations were taken into account. However, these were

concentrated solely in the high-field area in one quadrant. For a more detailed analysis in this Chapter, a set of 96 half-turns was chosen. The locations are shown in Figure 4.4. As justified in Chapter 3.2, the simulations of the MCBYH magnet and its circuit can be performed with a stand-alone simulation in STEAM-LEDET. The simulations for this analysis are set up the same way as presented in the validation Chapter 3.2. A short coding example is given in the Annex in Listing 3.

The set of locations consists of all corners of all coil blocks within the MCBYH magnet as well as half-turns centered within each coil block. Thus, it contains turns exposed to various different magnetic field strengths, turns with a different number of adjacent turns as well as turns in different positions within the electrical connections, which are shown in the Annex in Figure F.1.

Figure 4.5 shows the development of the hot-spot temperature for all 96 simulated quench positions. The colors indicate the magnetic field strength in the initial quench

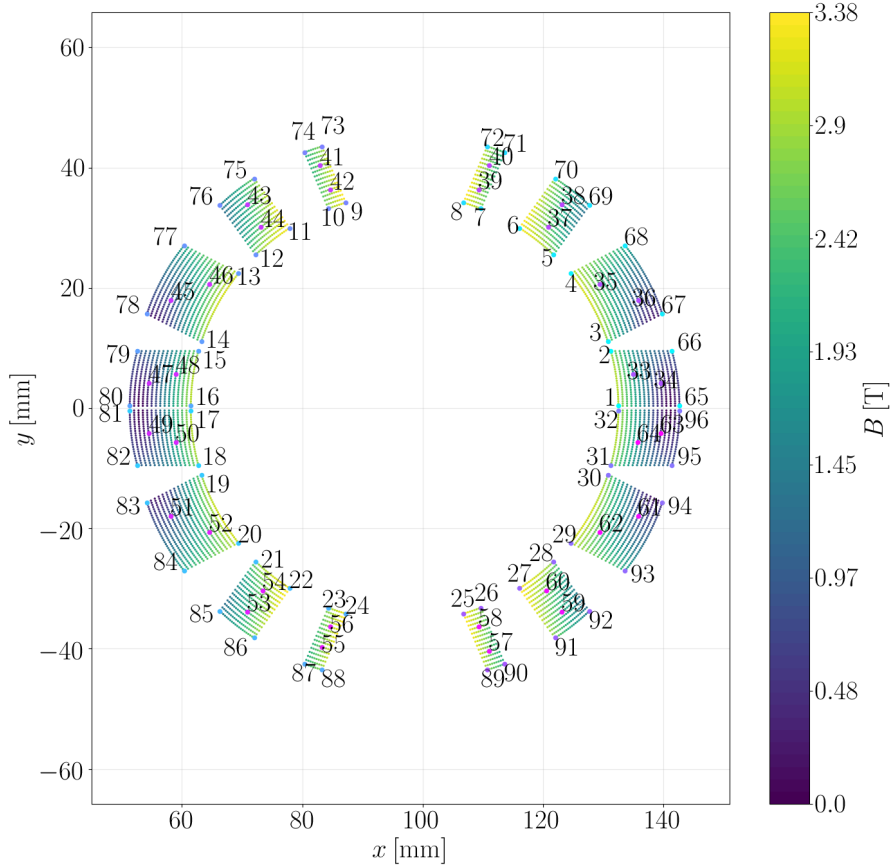


Figure 4.4: Magnetic field in the MCBYH coil turns and indicating the positions of the selected initial quench locations

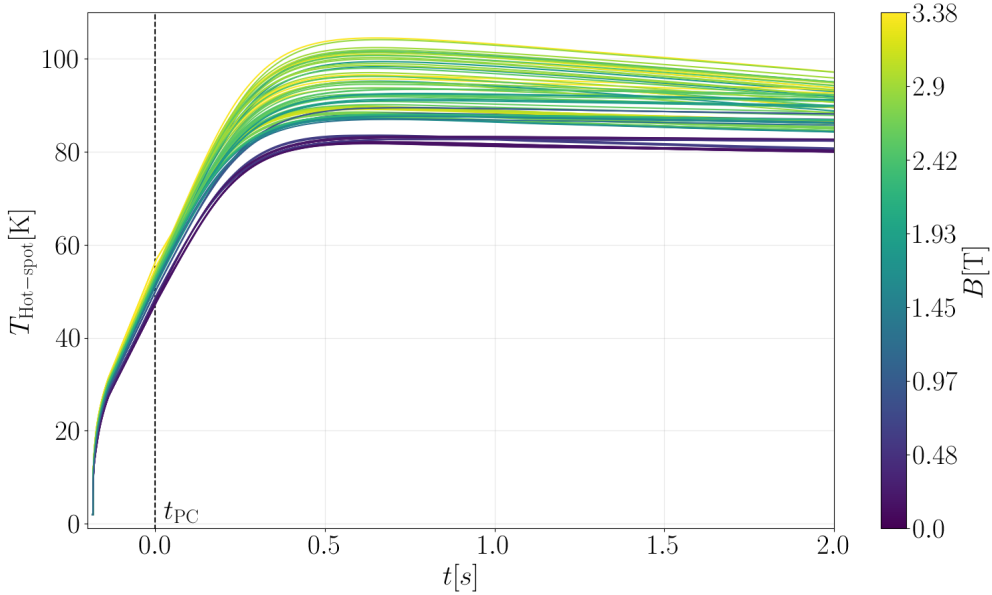


Figure 4.5: Evolution of the hot-spot temperature in the MCBYH turns in an FPA at $t_{PC} = 0$ s for all selected initial quench positions from nominal current. Colors indicate the number of turns in the coil-block of the first quenching turn.

location, as shown in Figure 4.4. In Figure 4.5 one can observe the dependency of the hot-spot temperature on the local magnetic field. The stronger the field in the initial quench position, the faster and higher the hot-spot temperature rises. For turns in the low field areas of the MCBYH, the peak hot-spot temperature reaches about 80 K. For the high-field turns this peak temperature can reach up to about 105 K. This corresponds to a temperature difference of about 25% of the low to high field quench locations. The field dependency is especially strongly visible at the beginning of the discharge until about 100-200 ms. However, afterwards, the dependency becomes less strong, as the temperature in the surrounding turns impacts the temperature in the initially quenched turn.

Other physical quantities are less impacted by the field dependency of the initially quenching turn but more by, for example, the number of turns that are in close vicinity and thus will be quenched due to heat propagation soon after. In Figure 4.6 the evolution of the coil-resistance for all initial quench locations is shown in dependency of the number of turns in the coil-block of the initial quenched turns.

The difference in the peak resistance for all simulations is only about 2.5%, while the difference in the final resistance is about 9%. Moreover, Figure 4.6 illustrates two properties of the quench propagation in the MCBYH magnet. First, the initial evolution of the coil resistance is governed by the size of the coil-block, which includes the quench location. The higher the number of turns in the coil block where the quench starts, the faster the resistance rises. This can be simply explained by the

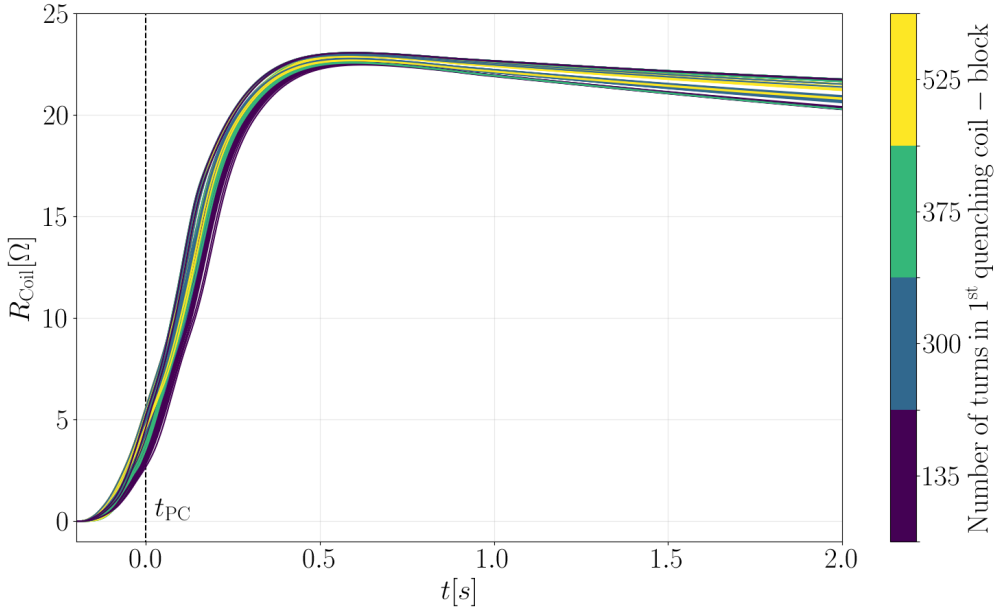


Figure 4.6: Development of the coil resistance in an FPA at $t_{PC} = 0$ s for all selected initial quench positions from nominal current.

heat propagation, which is much faster through the insulation into their neighboring turns than longitudinally along the electrical connections. The quench locations that are centered in the coil blocks lead to a faster quench propagation as these turns are thermally connected to four turns, instead of two as the corner turns. The coil resistance in dependency of the number of adjacent turns to the initially quenching turn is shown in the Annex in Figure G.15. Second, the final resistance is governed by the speed with which the quench is propagating through the coil-winding pack. Even though the coil blocks in the mid-plane and pole blocks consists of fewer turns than the largest coil block with 525 turns, the final resistance of the simulations starting in the smaller blocks sometimes still show a higher final resistance. These blocks are electrically connected to the respective other half of the magnet (compare Figure F.1) and thus spread the normal zone faster into all four quadrants of the magnet. This results in a generally higher resistance.

The discussed behavior can also be observed in the evolution of the fraction of conductor that transferred to the normal state, which is shown in Figure 4.7. Initially, the simulations with a quench starting in a large coil block generally cause a faster transition of conductor to the normal zone. Furthermore, the simulations with a quench starting in the turns centered in the smaller coil blocks also lead to a faster transition of conductor to the normal state as the initially generated heat is diffusing faster from the hot-spot. The evolution of the transferred amount of conductor in dependency of the magnetic field strength in the quench hot-spot is shown in the Annex in Figure G.16. The magnetic field impacts the speed of the

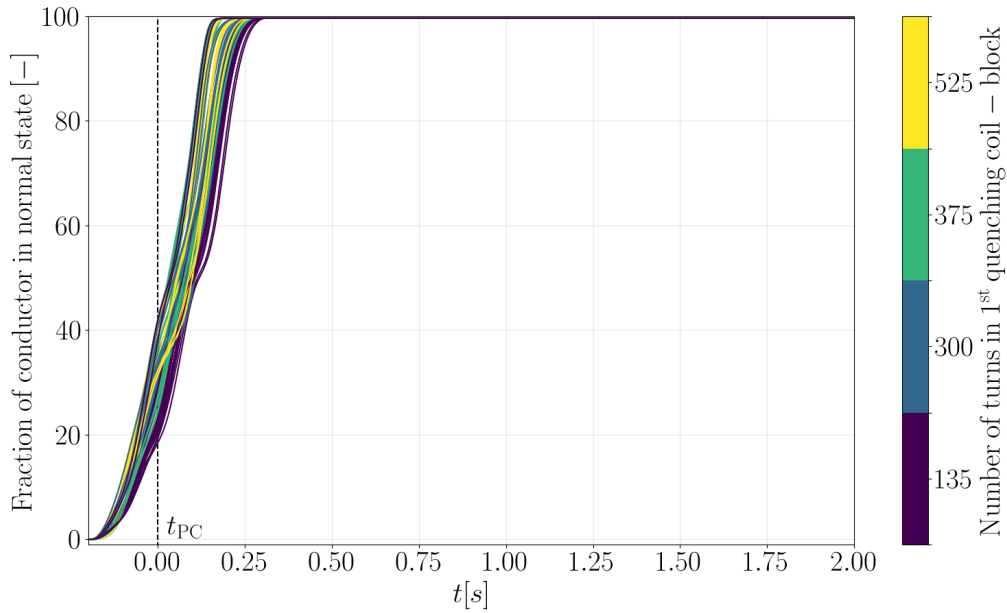


Figure 4.7: Development of the amount of conductor in normal state in an FPA at $t_{PC} = 0$ s for all selected initial quench positions from nominal current.

quench propagation twofold, i.e. causes a lower margin to quench as well as increases the longitudinal quench propagation velocity (compare Equation 2.11). In general, there can be a time difference of up to 130 ms between the simulations in the time required to propagate the quench to all turns. For all simulations, the full amount of conductor transferred to the normal state.

Figure 4.8 shows the voltages across the magnet. Once the first turn starts quenching, also the voltage across the magnet starts to rise until the power supply can not keep up the power load and the current starts dropping. At $t_{PC} = 0$ s the power supply disconnects and the voltage suddenly drops to about -14 V, which is the voltage drop across the crowbar and cable resistance of the warm parts. Afterwards, some voltage waves occur until at about 250 ms all of the conductors quenched and the voltage starts to decay pseudo exponentially. The difference between the simulations shows mainly in a slightly different shape and magnitude of the voltage waves after t_{PC} . It can be explained by the differing quench propagation through the magnet and electrical connections of the turns, affecting the voltage across the magnet. One can observe a dependency on the magnetic field strength in the first quenching turn at the beginning of the transient. The voltage across the magnet depending on the electrical position of the quench hot-spot is shown in the Annex in Figure G.17.

Finally, Figure 4.9 shows the current decay in all simulations for all assumed positions. The shape of the current decay is in general for all simulations the same. However, the initial rate of current discharge shortly before t_{PC} is different and thus results in a timing difference of about 60 ms and 15 - 20% difference in the current.

4.2 ANALYZING THE IMPACT OF DIFFERENT QUENCH LOCATIONS IN THE EXAMPLE OF SELF-PROTECTING MAGNETS

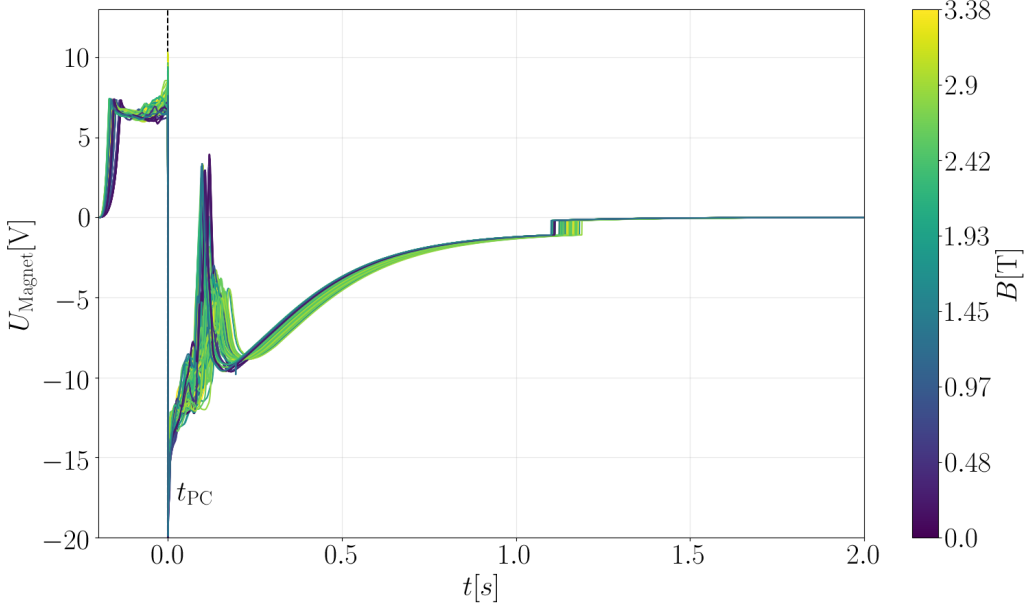


Figure 4.8: Voltage across the MCBYH dipole in an FPA at $t_{PC} = 0$ s for all selected initial quench positions from nominal current. Colors indicate the initial magnetic field in the first quenching turn.

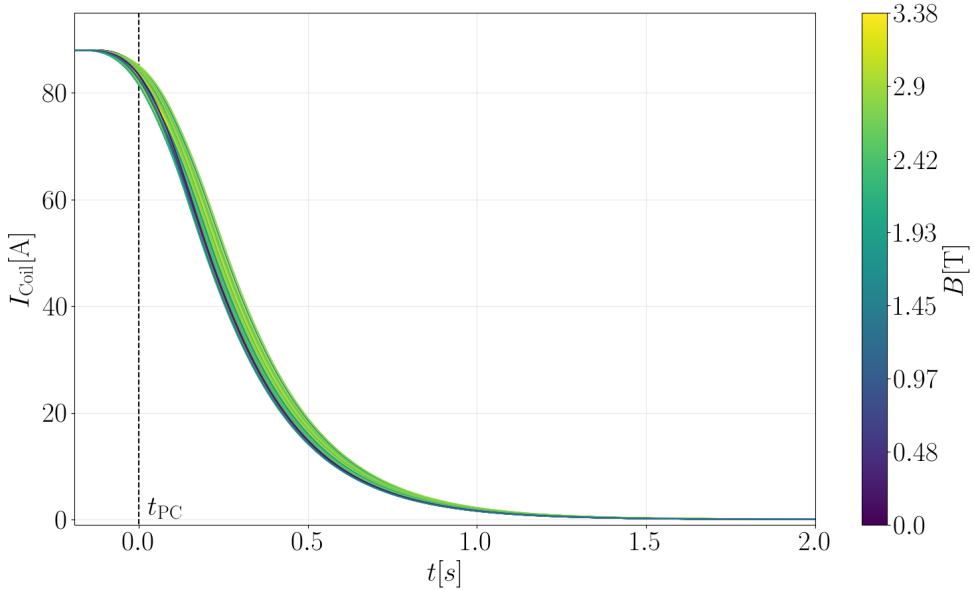


Figure 4.9: Decay of the magnet current in an FPA at $t_{PC} = 0$ s for all selected initial quench positions from nominal current. Colors indicate the initial magnetic field in the first quenching turn.

4.2 ANALYZING THE IMPACT OF DIFFERENT QUENCH LOCATIONS IN THE EXAMPLE OF SELF-PROTECTING MAGNETS

The fastest current decay can be observed for the quench hot-spots centered in the pole coil blocks. The current decays showing the number of neighboring turns to the initial quench hot-spot is shown in Figure G.18 in the Annex.

The framework opened up the possibility to conveniently set up simulations with different quench locations throughout the whole coil in order to analyze and predict the behavior of the magnet. This Chapter analyzed the differences occurring in the transients in the MCBYH magnet for the various initial quench locations. Comparing measured transients to these predictions might provide information about the position or the condition of the magnet. However, this analysis does not take the uncertainty of the initial moment of quench into account. A larger set of simulations or a direct comparison of measured and simulated detection voltage could decrease the uncertainty and thus provide even more accurate data for a specific event.

Furthermore, utilizing the framework to investigate the impact of different quench locations was in the scope of this thesis only applied on the self-protecting magnet MCBYH. However, this concept can be also applied to other LHC and HL-LHC magnets whose STEAM-LEDET or STEAM-COSIM models are validated. Prototype magnets are sometimes equipped with more voltage taps, which allow measuring voltages across parts of the coils or even single turns. Thus, comparing the simulated voltages, assuming different quench locations, to the measured signals might provide even further information. This investigation might lead to a more accurate prediction of the initial quench position, as more signals can be compared. Future research could use this framework to simulate a variety of locations, or even extend the framework such that also quench locations into the longitudinal dimension can be investigated.

5 Automatic generation of LHC main dipole events

The LHC ring, with its 27 km circumference, is split up into 8 different sectors. Each sector contains one main bending dipole circuit (RB circuit). Only these main dipole circuits already account for almost 2/3 of the total circumference of the LHC, as each of these circuits consists of a chain of 154 magnets with each a length of about 15.18 m [1]. Moreover, with a nominal current of 11850 A and a complex electrical circuit for powering and protection of the magnet circuit, the RB circuits are also among the most challenging LHC circuits to be modelled.

Analyzing the quench events in the RB circuits is thus of special importance, as faults need to be detected as early as possible to avoid damage and to keep the availability of the LHC as high as possible. Hence, each event in an RB circuit is analyzed by experts with dedicated notebooks, that gather and pre-process the measured data. The signals are usually compared to reference measurements. However, in the past years of operation, faults in the main bending dipole circuits were rare and thus the available data for specific faults is sparse. Additional simulations of the events for faults and reference cases can help understanding the dynamics of observed unexpected events and support the detection of pre-cursors of faults [54].

In Chapter 5.1 a typical quench event in the RB circuits will be described in more detail. An approach to simulate each of these events in an automatic way, while still trying to keep the required computational effort as low as possible, will be presented in Chapter 5.2. In Chapter 5.3 some of the simulation results will be shown. Moreover, in Chapter 5.4 multiple approaches will be presented, which attempt to reduce the required simulation time.

All plots of measurements in this Chapter are deduced from the Hardware Commissioning (HWC) notebooks [55], which are used to analyze events, occurring in the RB circuits.

5.1 Typical quench event in the LHC main dipole circuit

The RB circuit consists of various electrical components for powering and protection. An illustration of the circuit can be seen in Figure 5.1.

Part of the RB circuit is at room temperature (warm part), and part is at cryogenic temperature (cold part). The warm part includes the power converter and the energy extraction system composed of two modules located in the middle (also called EE-odd) and at the end of the chain (called EE-even). Each EE module consists of four breaker paths, with each three redundant switches, which open in case of a power abort in the system. The current is then forced through the four resistive paths with an effective resistance of approximately $R_{EE} = 73 \text{ m}\Omega$. The transition of the warm part to the cold parts of the circuit is realized with current leads. These are a Copper to High-Temperature Superconductor (HTS) transition. The cold parts of the circuits are placed within the cryogenic environment. This mainly consists of the

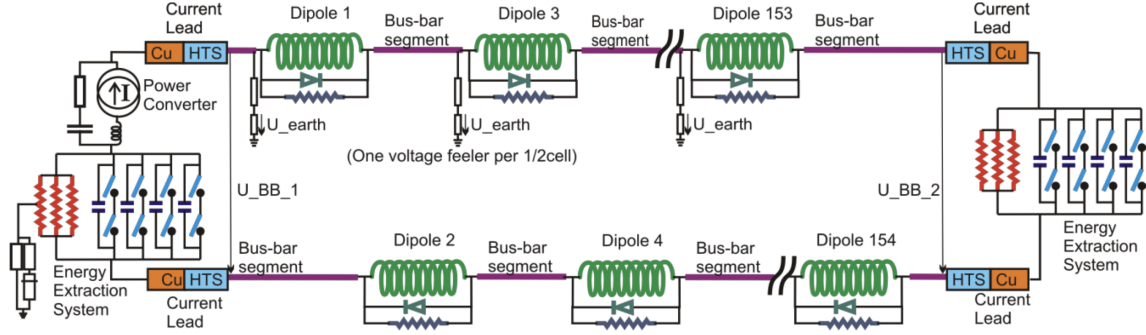


Figure 5.1: Illustration of the RB circuit in the LHC [56]. Numbering of the magnets shows the physical order in the chain, differing from the electrical order.

dipole magnets (MB magnet) and the cold by-pass diodes across them. All magnets are connected in series by superconducting bus-bars.

Once a quench is induced in one of the magnets, its coil resistance starts to quickly rise. The developed resistive voltage in the magnet is detected by the QDS which constantly monitors the voltage difference between the two apertures of a magnet but also differences between voltages across different magnets [57, 58]. The power converter is switched off at t_{PC} and the quench heaters of the quenching MB magnet are triggered. This drastically speeds up the development of the coil resistance. Due to the resistive voltage build-up, the opening voltage of the cold by-pass diode of about $U_{Th} = 6$ V is reached shortly after and the current starts to bypass the magnet. The energy of the quenched magnet is mostly dissipated in its coil, while the energy of the other magnets is extracted by the EE system. In order to limit peak voltages and electromagnetic disturbances, the two EE switches are opened shortly after each other, usually, with a delay of about 500 ms [59]. The opening times of the two EE switches will be denoted with $t_{EE,1}$ and $t_{EE,2}$, for the EE module in the middle of the chain and at the end of the chain, respectively. As the current by-passes the quenched magnets through the diodes, the discharge of the circuit is governed by the energy extraction with the time constant of about $\tau_{EE} = 102$ s, calculated as presented in Chapter 1.2.4. Thus, a full discharge of an RB circuit from nominal current takes about 300 to 350 s. In Figure 5.2 an example discharge of an RB circuit, compared to reference measurements, is shown. In this event, the power supply was switched off at $t_{PC} = 0$ s, while the circuit current was ramping up.

Usually, a quench in one of the magnets leads to so-called secondary quenches. These are quenches of magnets in close proximity to the original quenching magnet, i.e. either electrically series-connected or physically adjacent. One cause of secondary quenches is gaseous helium propagation. Each magnet is placed within a separate cryostat, while each three cryostats are combined into a cryogenic cell. Once one magnet starts to quench and its energy is deposited into its cryostat, the pressure

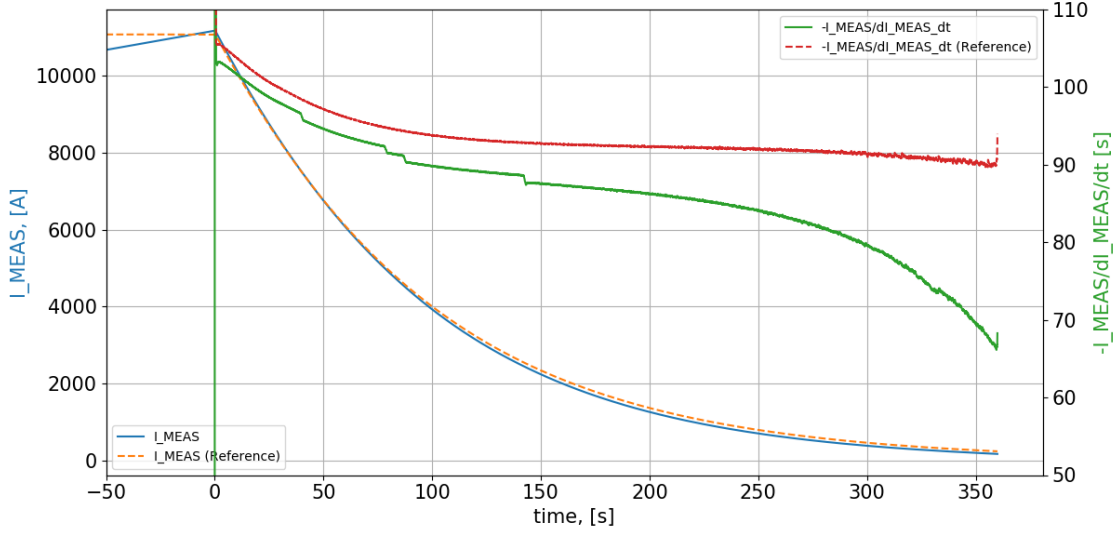


Figure 5.2: Measured discharge in one RB circuit, showing the measured circuit current I_{Meas} and current-to-current derivative ratio $-I_{\text{Meas}} \cdot \left(\frac{dI_{\text{Meas}}}{dt}\right)^{-1}$ compared to a reference, measured current [55]. RB.A78 circuit, 28.03.2021-22h09.

within the cryostat increases and leads to the boiling off of the helium II. However, the pressure increase in the first cryostats also affects the others in the same cryogenic cell and thus, it can affect the cooling of other magnets that are in close proximity and possibly lead to quenches in these magnets. Furthermore, also electromagnetic disturbances might lead to quenches in a magnet or to the spurious triggering of the QPS system of one magnet. In the event shown in Figure 5.2 these secondary quenches can be observed by the sudden jumps in the current-to-current derivative ratio. This occurs because after the quench of each magnet the circuit current bypasses one magnet, which means that its effective inductance decreases and one additional voltage drop occurs across the by-pass diode. In Table 11 the original quench, as well as all secondary quenches for the shown event, are listed. Note that all magnets with secondary quenches are in close, spatial proximity to the first quenching magnet, even though in the electrical order of the magnet chain they are far apart. This is due to the fact that all magnets with odd physical numbers are electrically connected in the first half, while all magnets with even physical numbers are electrically connected reversely in the second half (compare Figure 5.1).

In Figure 5.3 the voltages across the cold protection diodes are shown. After the power converter is switched off, the voltage across the power converter drops to -10 V. Afterwards, the voltage decays following the current in the circuit. At the moment of each secondary quench, the voltage across the respective protection diode quickly rises to its opening voltage. The cold diodes show a non-linear relationship between their temperature and their opening voltages and are placed in the same

Table 11: RB event - Original quench and all secondary quenches, showing the time of quench t_q and current at the moment of the quench I_q . RB.A78 circuit, 28.03.2021-22h09.

| Quench order | t_q [s] | I_q [A] | Physical position | Electrical order | Cause of quench |
|--------------|-----------|-----------|-------------------|------------------|----------------------------|
| 1 | -0.01 | 11177 | 59 | 30 | Training |
| 2 | 40.09 | 7500 | 56 | 126 | Gaseous helium propagation |
| 3 | 78.73 | 4967 | 57 | 29 | Gaseous helium propagation |
| 4 | 87.34 | 4521 | 58 | 125 | Gaseous helium propagation |
| 5 | 142.55 | 2438 | 61 | 31 | Gaseous helium propagation |

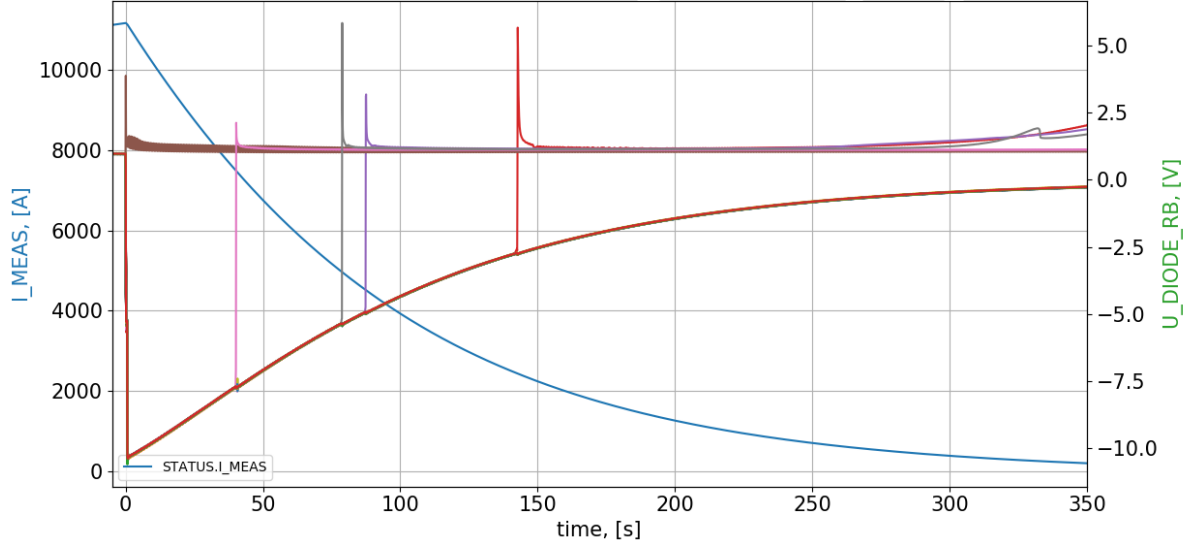


Figure 5.3: Measured discharge in one RB circuit, showing the current discharge (blue) and the measured voltages across the cold by-pass diodes $U_{\text{Diode, RB}}$ in different colors [55]. RB.A78 circuit, 28.03.2021-22h09.

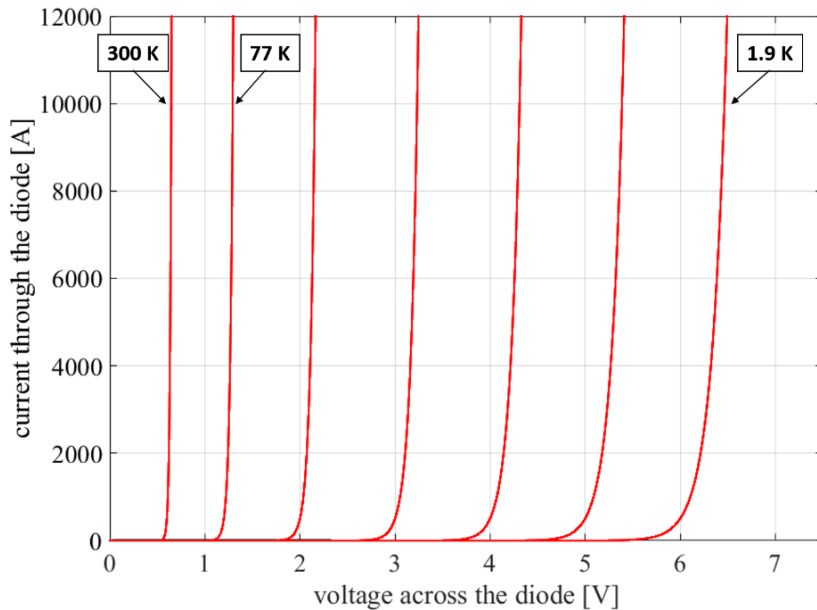


Figure 5.4: Qualitative forward characteristics of the protection diode of MB magnets at different temperatures [27]

cryostat of the magnet to protect. Hence, due to the thermal propagation within the cryostat, the opening voltage of the diode is quickly reduced, as it can be observed for the quenches 1,2 and 4 in Figure 5.3. The qualitative relationship of the forward characteristics of the cold diodes is plotted in Figure 5.4. As a consequence, the voltage across the diode can become as low as about 1.2 V. This can be also observed in the voltages in Figure 5.3. Once the diode is conducting, power is dissipated within the diode and thus leads to heating. The opening voltage thus represents the peak voltage across the diode as it starts to quickly drop, once conducting.

Furthermore, the RB circuits contain an electrical system monitoring the current to ground during the transient. During an analysis of an event in the RB circuit, these currents are observed and evaluated in order to identify a potential fault in the circuit. The amplitude of currents to ground through the earthing system is in the range of a few milliamperes to amperes.

Moreover, also the voltages between the apertures and across the magnets are of special interest, as these might indicate a possible short-to-ground or inter-turn short. Investigating and evaluating the electro-magnetic perturbations that might lead to the spurious triggering of the QDS can also lead to interesting insights.

5.2 Hierarchical co-operative simulation

The simulation of events in an RB circuit represents a complex challenge, as multiple scales are involved. While the discharge of the whole magnet takes about 300 to

350 s, a single magnet in the chain is discharged in a few hundreds of milliseconds. Furthermore, during the full transient, the density of events is sparse, so that for time windows of hundreds of seconds no complex transients occur, but the circuit just follows a rather simple pseudo-exponential decay. Meanwhile, around the moments of secondary quenches, complex transients are occurring, that require a finer time stepping. Moreover, the required computational power and simulation time shall be as low as possible, while still maintaining an acceptable accuracy.

One technique to simulate events like this is a hierarchical co-simulation. In this approach, the full discharge is split up into several parts that are independently simulated and re-combined for one final simulation. Around the first and all secondary quenches, the full physical model, including the electro-magnetic thermal model in STEAM-LEDET as well as the electrical model in PSPICE[©], will be co-operatively simulated for a pre-defined period. These co-operative simulations capture the transients occurring during the discharge of each quenching magnet. The duration of each of these simulations thus needs to be adjusted to the expected length of the discharge. In the RB circuit, usually, this time value is below 1 s for quenches at current levels above 7 kA, below 2 s and 3 s for quenches occurring below 7 and 3 kA, respectively. After each of these events was simulated independently, the evolution of the coil resistances of the quenching magnets is used and combined together to one long, purely electric simulation with more sparse time-stepping. An illustration of this concept is shown in Figure 5.5.

This approach can be justified for two reasons. First, all magnets, besides the quenching magnet, stay superconductive as their QDS is not triggered and they do not develop any resistance. Modelling them with an equivalent electrical circuit model is thus sufficient to capture the behavior [60]. Second, the transients in the quenching magnet are almost fully included in the proposed simulation length. Once the resistance in the quenching magnet is large enough such that the current is close to fully bypassing through the diode, the thermal transients within the coil winding pack do not influence the circuit current and thus can be neglected.

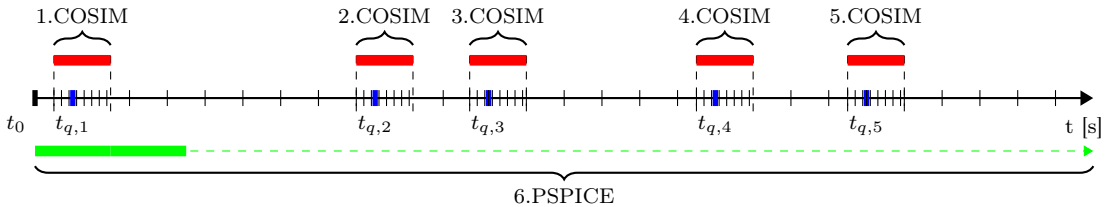


Figure 5.5: Hierarchical co-operative approach to simulate multiple quench events in RB circuits. Blue indicates moments of quench in magnets of the chain, red the time window for full co-operative simulations and green the time window for the PSPICE[©] simulation. Numbers show the simulation order.

| | A | B | C | D | E | F | G |
|----|--------------|----------|------------|-----------------|----------------|----------------|---------------|
| 1 | Circuit Name | Period | Date | Timestamp | t_EE,1 [ms] | t_EE,2 [ms] | |
| 2 | RB.A78 | HWC 2021 | 28/03/2021 | 09:34.4 | 591 | 93 | |
| 3 | RB.A78 | HWC 2021 | 28/03/2021 | 09:34.4 | 591 | 93 | |
| 4 | RB.A78 | HWC 2021 | 28/03/2021 | 09:34.4 | 591 | 93 | |
| 5 | RB.A78 | HWC 2021 | 28/03/2021 | 09:34.4 | 591 | 93 | |
| 6 | RB.A78 | HWC 2021 | 28/03/2021 | 09:34.4 | 591 | 93 | |
| 7 | | | | | | | |
| 8 | Position | I_q [A] | t_q [ms] | Type of Quench | U_EE_max_1 [V] | U_EE_max_2 [V] | Quench origin |
| 9 | C28L8 | 11177 | -10 | Training | 789.0374135 | 785.1671779 | INT |
| 10 | B28L8 | 7500 | 40089 | GHe propagation | 789.0374135 | 785.1671779 | EXT |
| 11 | A28L8 | 4967 | 78731 | GHe propagation | 789.0374135 | 785.1671779 | EXT |
| 12 | A29L8 | 4521 | 87345 | GHe propagation | 789.0374135 | 785.1671779 | EXT |
| 13 | B29L8 | 2438 | 142522 | GHe propagation | 789.0374135 | 785.1671779 | EXT |

Figure 5.6: Simplified and slightly edited output file of the HWC notebook, analyzing an RB event

The set-up of these simulations is realized in a fully automatic way, partly utilizing the already described features of the framework. As an input for the set-up, the summary file from the hardware commissioning notebook is used. An example of this file, slightly edited for the purpose of this thesis, is shown in Figure 5.6. This file includes the information already described in Table 11 as well as further electrical and timing information, for example about the EE system.

The framework reads this csv-file and performs the following steps in order to adjust the simulation to the real event:

1. Calculation of the equivalent electrical position

The position of the quenching magnet, which was deduced by the QDS system, is only provided as the name of the assembly unit. The framework accesses a simplified version of the assembly database and deduces the electrical position of the assembly unit in the chain of magnets. The positions corresponding to the shown assembly units can be seen in Table 11. Based on the electrical position, the purely electrical representation of the respective quenching magnet as a series of inductances and resistances is replaced with the equivalent magnet model used for co-operative simulations shown in Figure 2.7.

2. Setting of the quench in the electro-magnetic thermal model

In Figure 5.6 it can be seen that the QDS in the RB circuits also gives an approximation of the quench origin. This can be either the internal (INT) or external (EXT) aperture of the magnet. However, based on the deduced location, the definition of this changes from left and right aperture. The quench is artificially initiated in STEAM-LEDET in a high-field turn of the respective aperture at the given time. In Figure 5.7 the magnetic field map of the MB

magnet, calculated using ROXIE [61], and the assumed quench origins are shown.

3. Calculation of the energy extraction resistances

The components of the LHC circuits also show some uncertainty. In order to make the simulation as accurate as possible, the measured voltage across the EE system modules is used to determine more precise values of their resistances. The calculation simply follows Ohm's law.

4. Generation of the electrical circuit

Given the acquired information, the electrical circuit model with the correctly positioned, pre-defined co-simulated magnet models (compare Chapter 2.6) as well as all electrical and timing information is generated.

5. Generation of the COSIM folder structure and port definitions

Following the COSIM specific structure, all required directories and files are generated, which include also the user-dependent locations of executables for the software.

6. Generation of executable batch file

All quench events that shall be executed are combined to a single batch file, inheriting the consecutive commands for the software. The user can therefore start the full simulation with "one-click".

Furthermore, the user can define the simulation options. The standard options, which are assumed to perform well for most cases, are shown in Table 12.

As described, the end time of the final time window depends on the current level. Note that due to convenience reasons, $t_{PC} = 0.1$ s was chosen, as PSPICE[©] does not support negative time. The simulations are all shifted by this offset in the post-processing.

Table 12: Simulation options for the co-operative simulations, including time stepping and convergence tolerances

| Time window | 1 | 2 | 3 | 4 | 5 |
|-----------------------|---------|---------|--------|--------|---------------|
| t_{Start} | 0 s | 0.12 s | 0.2 s | 0.3 s | 0.5 s |
| t_{End} | 0.12 s | 0.2 s | 0.3 s | 0.5 s | 1.1 / 2 / 3 s |
| $t_{Step, PSPICE}$ | 0.1 ms | 0.1 ms | 0.1 ms | 0.1 ms | 0.1 ms |
| $t_{Step, LEDET}$ | 0.01 ms | 0.05 ms | 0.1 ms | 0.1 ms | 0.1 ms |
| $\epsilon_{Relative}$ | 8e-4 | 8e-4 | 8e-4 | 8e-4 | 8e-4 |
| $\epsilon_{Absolute}$ | 5 | 5 | 5 | 5 | 5 |

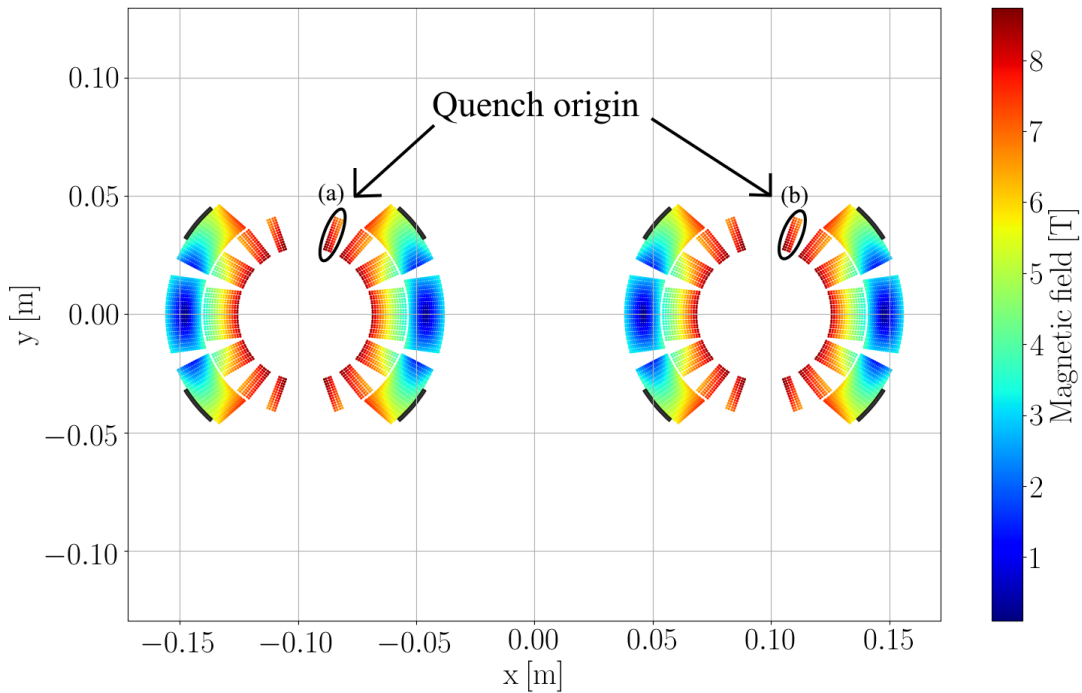


Figure 5.7: Magnetic field in the MB coils, calculated using ROXIE [61] and including iron yoke effects, showing the two assumed quench positions (a) and (b) in the two apertures. Positions of quench heater strips on the coil are indicated in black. Width of heater strips is increased for illustration.

After the simulations are completed, the framework reads the final development of the coil resistances of each quenching magnet, and shifts these by the correct time, such that each simulation is placed at its correct time. For each magnet, a corresponding stimulus file is written, which controls the resistance value of Equation 2.13 for a voltage source within the electrical magnet model. Finally, the electrical model of the combined simulation is generated. This includes the purely electrical circuit model in PSPICE[©] that was already used in the co-operative simulations. Only the resistive voltage will be externally defined for the PSPICE[©] simulation this time.

5.3 Results of hierarchical co-operative simulation of a multiple quench-event

In this Chapter, the simulation results of one exemplary event in one LHC RB circuit using the hierarchical co-operative simulation approach, including multiple quenches, will be shown in more detail. However, within the scope of this thesis, the simulations are not compared to measurements. The performance of the model in a co-operative simulation for a single quench event was already investigated extensively in the past and achieved good agreement [54, 59, 60, 62].

In Figure 5.8 the current for the full discharge of the circuit as well as the current through the quenching magnets and their protection diodes are shown.

The circuit discharge is mainly governed by the energy extraction systems. To illustrate this, the RB circuit current in Figure 5.8 is compared to an exponential decay with the time constant calculated using Equation 1.10. The difference of both curves is very small, with a maximum difference of about 80 A. This can be explained by the small-time delay of the opening times of the EE systems ($\tau_{EE,1} = 93$ ms, $\tau_{EE,2} = 593$ ms) as well as small remaining currents in the magnet coils and internal resistances of the diodes. Furthermore, the firing of the quench heater does not lead to an immediate quench in the connected turns. First, the heating stations on the strips heat up and the heat diffuses through the insulation into the magnets coil turns. Once these turns exceed their critical temperature, they transition into normal state and electrical resistance is developed. In Figure 5.9 the zoomed time windows around each of the quenches in the event are shown.

In Figure 5.9a this can be seen for the first quenching magnet. The voltage threshold for quench detection is reached at about $t_{q,1} = -0.01$ s, leading to a fast power

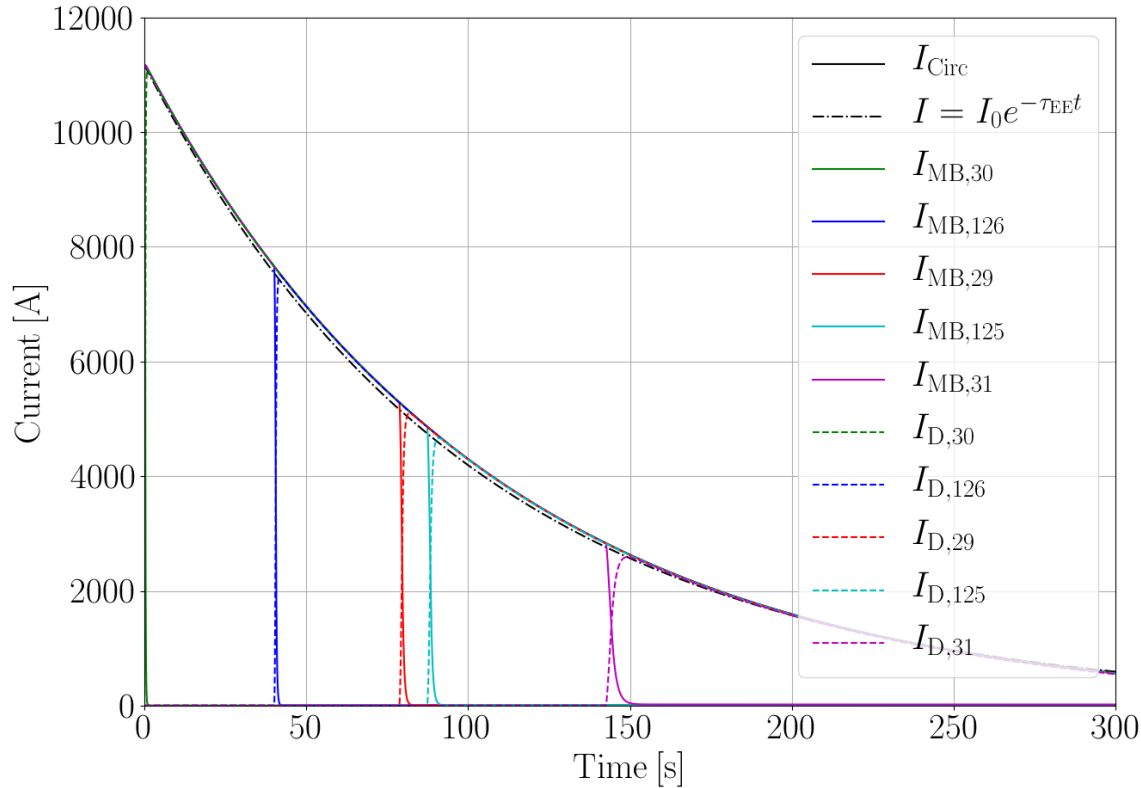


Figure 5.8: Simulated current discharge in the RB circuit, compared to a purely exponential decay with $\tau_{EE} = 102$ s, as well as all currents in the quenching magnets and their protection diodes

abort at $t_{PC} = 0$ s, where the power converters of the circuit are switched off and disconnected from the chain of magnets. After a short delay, the quench heater are fired as well at $t_{QH} = 2$ ms. In Figure 5.9a the current in the magnet still does not drop until about 30 ms, when the turns touched by the quench heater transition to the normal state. Shortly after, at around 120 ms, the current discharge in the magnet speeds up even further. This can be explained by the described quench-back phenomenon (see Chapter 4.1.1).

The peak inter-filament coupling loss and the inter-strand coupling loss deposited in the first 500 ms of the transient are shown in Figure 5.10a and Figure 5.10b, respectively. These coupling losses are mostly induced in the inner, higher field region of the coil, as in that coil part the total magnetic field change is the largest. Furthermore, as ISCL and IFCL are not developed in already quenched turns, the initial quench hot-spot and the turns touched by quench heater show zero or only

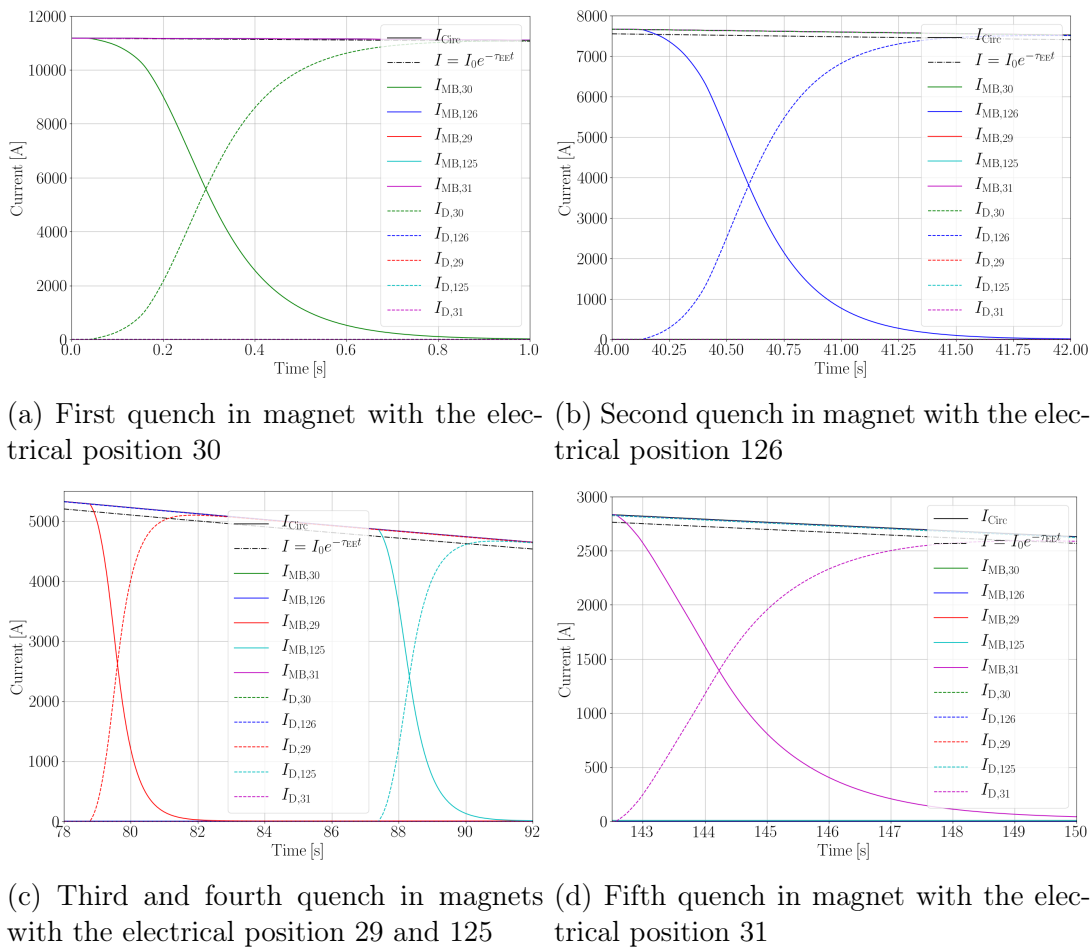
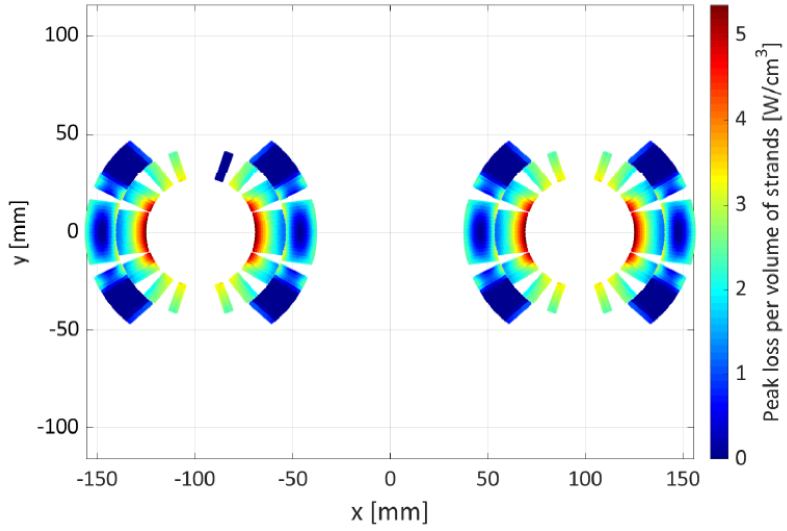
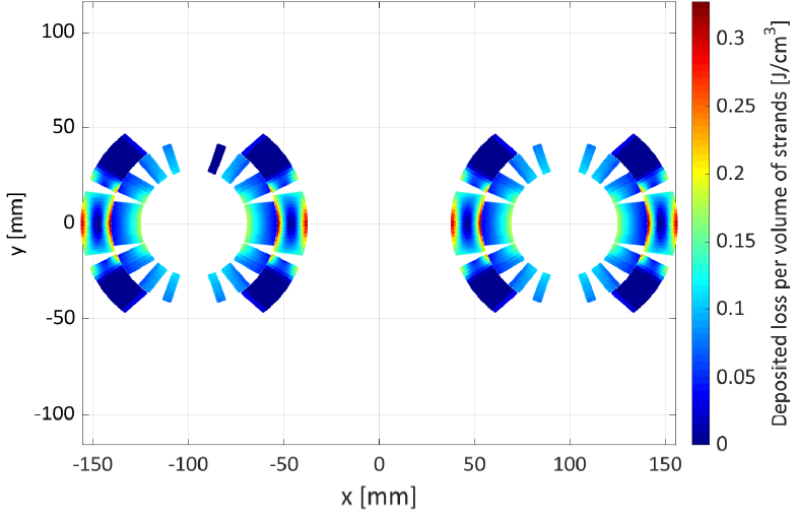


Figure 5.9: Current discharge in the RB circuits as well as in all quenching magnets and their diodes. a)-d) show the respective zoom for the different quenches

little deposited loss. Thus, the highest loss is deposited in the conductors of the inner layer turns. Also, note that the ISCL in the magnet are significantly smaller than the IFCL. This is mainly due to the larger time constant of ISCL and the relatively fast discharge of the MB magnet. In the first quenching magnet, the inner pole turns are quenched by coupling loss after about 120 ms, while the remaining turns in the inner layer quench around 150 ms. The turns in the outer MB layer not touched by the heaters quench mostly due to coupling loss after around 200 to 300 ms.



(a) Peak inter-filament-coupling-loss per unit volume of strand in the conductors



(b) Deposited inter-strand-coupling-loss per unit volume of strand in the conductors

Figure 5.10: Coupling current losses in the first quenching MB magnet in the first 500 ms of the transient

One can observe this as well in the Annex, in Figure H.19, which shows the cause of quench for all turns during the discharge, as well as in Figure H.20, showing the respective times of quench. The full discharge of the first quenching magnet takes in total about 800 ms. The current is then almost completely flowing through the diode. As this diode also shows some resistance, a very small fraction of the current remains in the magnet. For the first quenching magnet, about 2 A, representing about 0.02% of the initial current, remain in the magnet.

In Figure 5.11 the peak temperatures in the coil turns, obtained during the discharge, are shown. The peak temperature obtained during the discharge from almost nominal current is less than 160 K and thus far below the recommended maximum temperatures for superconducting cables [19]. It is interesting to notice, that these temperatures are reached in the turns touched by the quench heaters and not in the initial quench hot-spot, only reaching about 120 K. First, these turns are heated up by the quench heater strips, which reach temperatures of about 140 K. In fact, the heating in these conductors becomes so high during the discharge, that heat diffuses back onto the quench heater strips. Second, these turns are also quenched at the very beginning of the discharge and the stabilizer matrix is thus exposed to a high current for a longer period than most of the other turns. The peak temperature is thus substantially higher. The remaining turns in the MB magnet show temperatures between 23 and 70 K, mainly depending on the deposited loss and their time of quench.

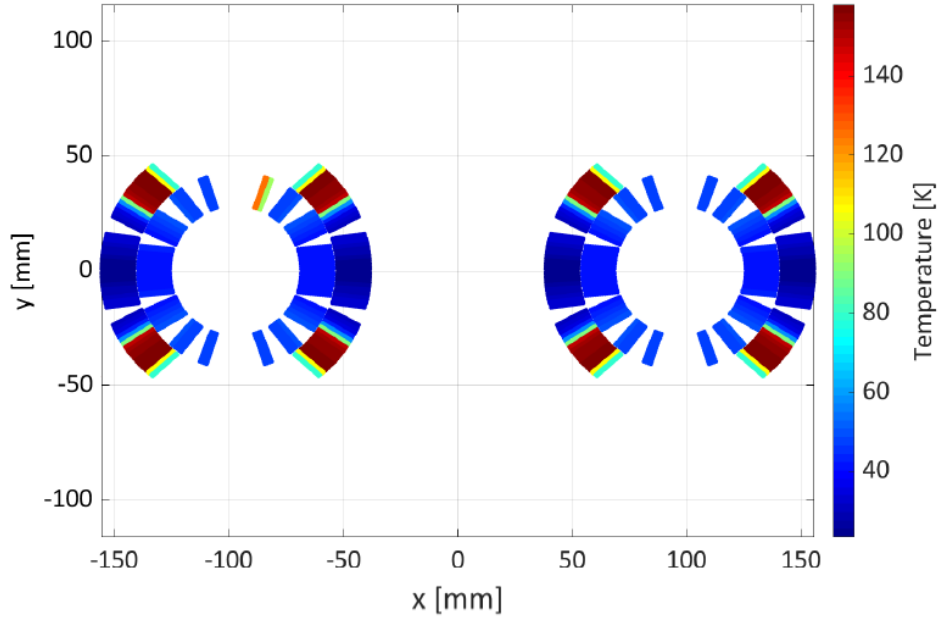


Figure 5.11: Peak-temperatures in the strands of the first quenching MB magnet, with an initial current of $I_q = 11177$ A

5.3 RESULTS OF HIERARCHICAL CO-OPERATIVE SIMULATION OF A MULTIPLE QUENCH-EVENT

In Figures 5.9b-5.9d the currents in the circuit, in the other quenching magnets and in their diodes are shown. One can observe that the speed of the discharge in the magnets decreases with the current level. While the discharge of the current in the second quenching magnet at about 7.7 kA takes about 1.5 s, the last magnet which quenches at about 2.8 kA takes about 9 s. The effect of the lower current level on the time of the discharge is threefold. First, the lower current level leads to less Joule heating in the quenched parts of the conductor, following Equation 1.1. Thus, the peak temperature in the conductor is lower, resulting in a lower resistance of the quenched turns. Second, due to the lower magnetic field and current density, the margin to quench is larger. Hence, the quench heater induced quenches occur with a longer delay. Third, the lower resistance in the magnets turns leads to a lower initial current change and as well to a lower change of the local magnetic field. This influences the amplitude of the coupling currents and respective losses. In fact, the change of the magnetic field in the last quenching magnet is not sufficient to induce coupling currents high enough to quench any of the turns. The resistance in the quenching magnet on lower current level is thus solely defined by the developed resistance of the turns quenched by the quench heater as well as turns in close proximity which were quenched because of transversal heat propagation.

The development of the coil resistances of the different quenching magnets is shown in Figure 5.12. In the evolution of the resistance of the first quenching magnet $R_{MB,30}$

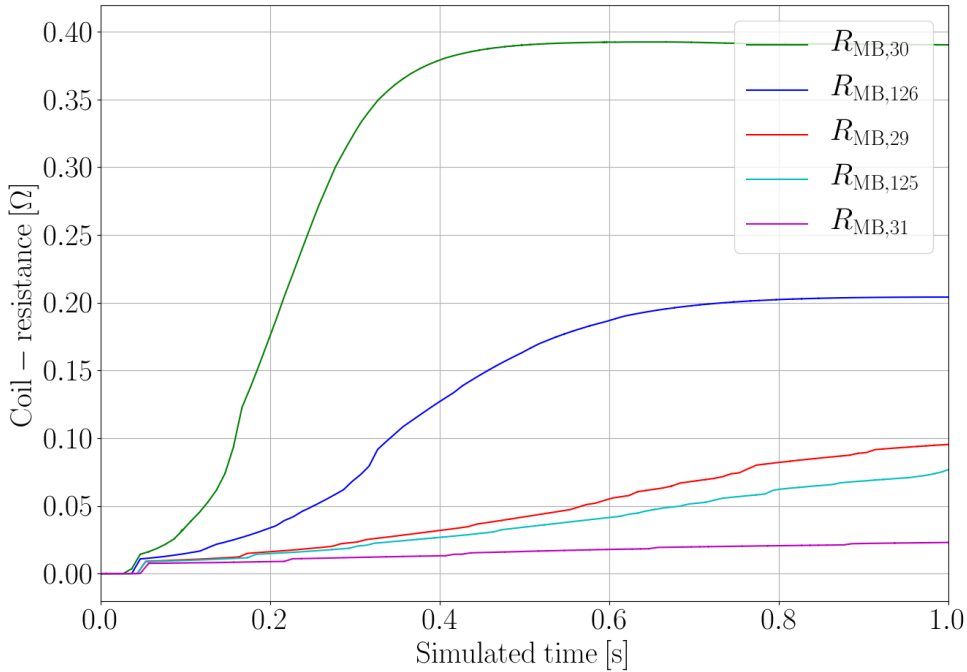


Figure 5.12: Development of the MB coil resistance during the simulation. $t = 0$ s corresponds to the start of each simulation.

one can observe that the resistance suddenly starts rising at about 32 ms when multiple turns are quenched at the same time due to the QH. After about 120 ms, the resistance starts growing faster, as a result of the turns that quench due to coupling loss. At about 500 ms the peak resistance is reached and is slowly decreasing from there. This is due to the fact that the discharged magnet, now only carrying a very small current, is slightly cooled down. For the other cases, the resistance starts to rise slightly later due to the larger margin to quench. In the resistance development of the second quenching magnet $R_{MB,126}$, the effect of quench back can still be observed around 180 ms, while for the cases at current levels lower than 5 kA this effect does not play an important role anymore and thus can not be directly observed in the resistance. In general, the final developed resistance in the different cases is directly dependent on the initial current level at the moment of quench. While both apertures of the MB magnet reach a resistance of about 0.4Ω , when quenching at high current, this decreases to less than 0.05Ω for the case at about 2.5 kA. The difference in the resistance results from the fact, that for cases at smaller current not all turns are transferred to the normal state, and those that are in the normal state heat up significantly less. In the Annex, in Figure H.21 the evolution of the amount of coil volume transferred into normal state is shown. The final amount of coil volume in normal state $\max(f_{con, normal}) [\%]$, at the end of each simulation, the duration of the discharge to reach 5 % of the initial current $\tau_{mag} [s]$, the maximum coil resistance $\max(R_{Coil})$ and peak- and average- coil-temperature $\max(T_{Coil})$ and $\text{avg}(T_{Coil}) [K]$ and the remaining magnet current $I_{mag,end} [A]$ are summarized in Table 13 for all magnet quenches at current levels $I_q [A]$.

The developed resistance in the magnet also determines the remaining current flow in the magnet. While the first magnet with a peak temperature of about 158 K only carries about 2.3 A, the relatively cold magnet that quenches last, only reaching 40 K, carries almost ten times the amount of about 20.5 A. A zoom of Figure 5.8 showing the remaining current in the magnets, is shown in the Annex in Figure H.22. Another signal of special interest for the detection of faults in the RB circuits are the voltages across each magnet and each of their apertures. In Figure 5.13 the voltages across each magnet for the full discharge are shown.

Table 13: Summary of discharge characteristics of the different quench simulations

| | Quench 1 | Quench 2 | Quench 3 | Quench 4 | Quench 5 |
|-------------------------|-----------------|-----------------|-----------------|-----------------|-----------------|
| I_q | 11177 A | 7500 A | 4967 A | 4521 A | 2438 A |
| τ_{mag} | 0.58 s | 1.11 s | 2.02 s | 2.36 s | 5.30 s |
| $\max(f_{con, normal})$ | 100 % | 92 % | 78 % | 72 % | 60 % |
| $\max(R_{Coil})$ | 0.39Ω | 0.21Ω | 0.10Ω | 0.09Ω | 0.03Ω |
| $\max(T_{Coil})$ | 158 K | 103 K | 70 K | 65 K | 40 K |
| $\text{avg}(T_{Coil})$ | 66 K | 44 K | 27 K | 24 K | 13 K |
| $I_{mag,end}$ | 2.3 A | 3.6 A | 7.3 A | 8.4 A | 20.5 A |

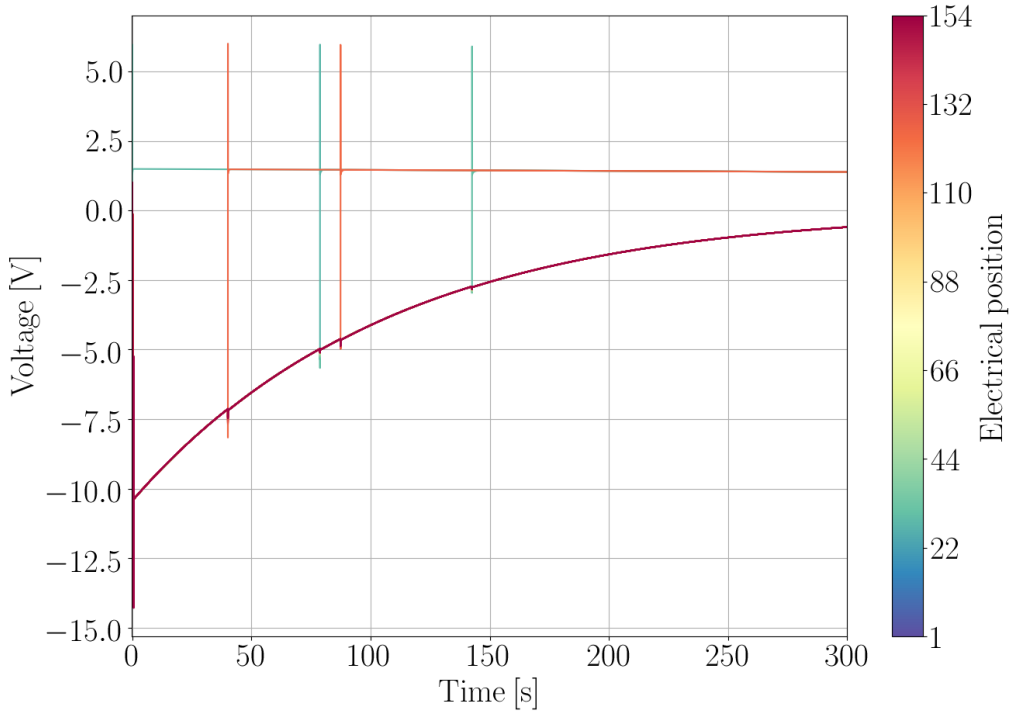
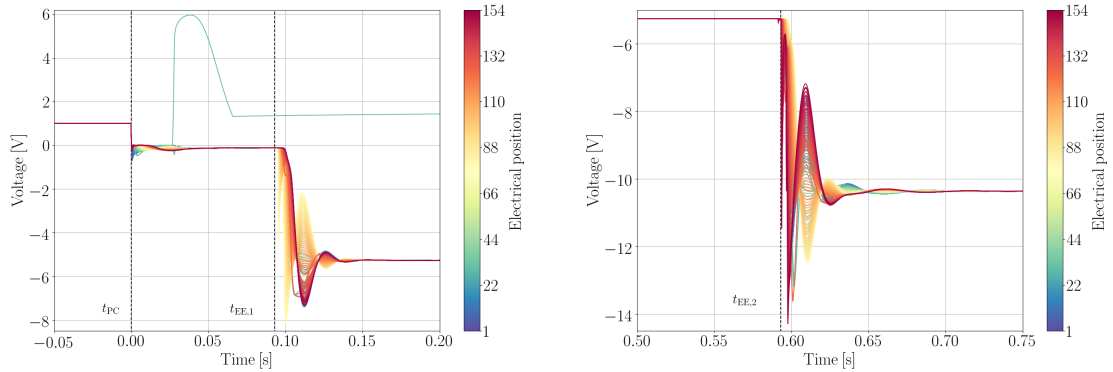


Figure 5.13: Voltages across each magnet for the full discharge in the RB circuit. Color grading describes the electrical position in the chain of magnets.

The voltages across each magnet in the circuit first increase step-wise with the openings of the energy extraction. Thus, after the first opening, the voltage across each magnet is:

$$U_{\text{mag}} = -\frac{R_{\text{EE}} I_{\text{Circ}}}{n_{\text{mag}}} = -\frac{73 \text{ m}\Omega \cdot 11177 \text{ A}}{154} = -5.1 \text{ V}$$

and respectively $U_{\text{mag}} = -10.2 \text{ V}$, after the opening of the second energy extraction. From there, the voltages are decaying, following the circuit current. At each moment of quench of one of the magnets, the voltage across this magnet quickly rises to the opening voltage of the cold-protection diodes of about 6 V, and subsequently it drops to about 1.6 V due to the heating effect. Comparing the simulated voltages in Figure 5.13 and the measured voltages across the diodes in Figure 5.3, one can see that the opening voltages of the different diodes vary, as the gaseous helium propagation and resulting pre-heating of the protection diodes is not included in the model. Furthermore, also the re-cooling of the diodes towards the end of the discharge is not included.



(a) Zoomed voltages after the power supply is switched off and the first EE system is opened
(b) Zoomed voltages after the second EE system is opened

Figure 5.14: Voltages across each magnet in the RB circuit, zoomed around power abort at t_{PC} and the opening voltages of the energy extraction systems $t_{EE,1}, t_{EE,2}$

In Figure 5.14 the voltages across each magnet, zoomed around the opening of the two energy extractions, are shown. When the power supply is switched off, the voltage waves mainly show voltage differences along the chain of magnets, following the electrical ordering. This results in a color grading from dark blue to dark red. The frequency of the waves corresponds to the natural resonating frequency of the circuit.

On the other hand, at the opening time of the first EE switch, centered in the chain of magnets, the voltage wave looks different. The voltage waves after opening the EE switches are introduced by the formation of an LC transmission line, consisting of the magnet inductances and the distributed parasitic capacitances across the circuit. From the EE module in the center of the chain, the voltage wave propagates along the two branches towards the first and, respectively, last magnets in the electrical connections. Thus, the voltages in the magnets closest to the EE module (e.g. 74 in the first half and 75 in the second) drop first. From there the voltage wave travels further in both branches. This results in a color grading in Figure 5.14a of yellow towards dark red. Note that the voltage wave in the first half with a color grading of yellow towards dark blue (corresponding to the magnets in physical positions with odd numbers, compare Figure 5.1), is overlapped by the second half (corresponding to the magnets in physical positions with even numbers). Moreover, in Figure 5.14a the rising voltage across the first quenching magnet after about 30 ms and the heating effects can be seen in light blue (electrical position 30).

The voltage wave in Figure 5.14b then shows the induced voltages after the opening of the second EE system. Similar to the voltage waves after the first opening, the wave is just turned, as the second EE system is connected to the end (or start

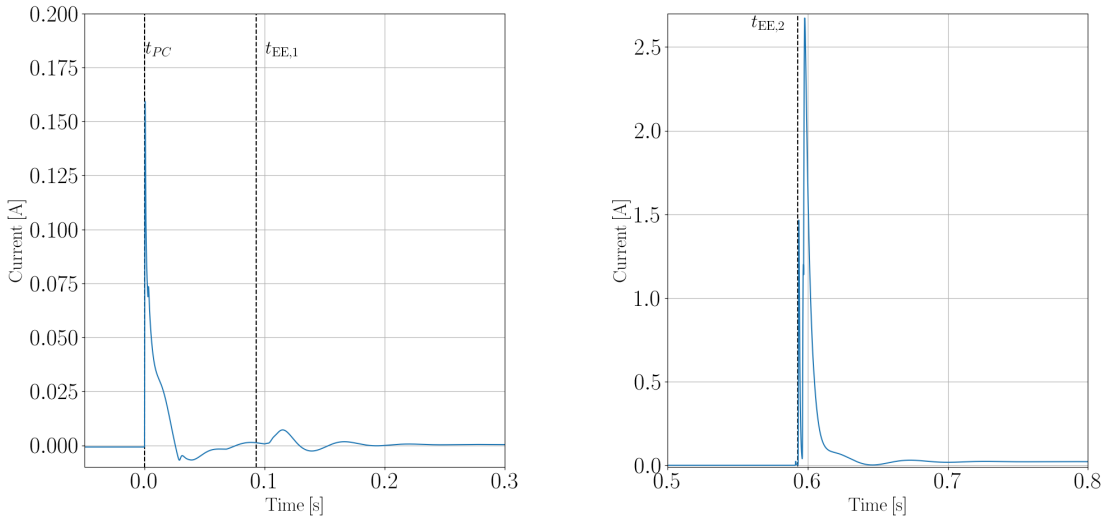
5.3 RESULTS OF HIERARCHICAL CO-OPERATIVE SIMULATION OF A MULTIPLE QUENCH-EVENT

respectively) of the magnet chain. Hence, the magnets in the electrical positions 1 and 154 are dropping first. From there the voltage wave travels further in both branches, resulting in a color grading in Figure 5.14b of dark red towards yellow. One can observe that some of the magnets do not align with the color grading. These differences are induced by the different impedances of the magnets in the chain. The different impedances in the chain of magnets were studied in the past [60, 62] and were measured in the tunnel, such that the electrical model can take these into account.

In the Annex in Figure H.23 the voltages across the magnets after the second quench event are shown. The voltages after the second quench first occur at the end of the chain, where the second quenching magnet is located. From there, they travel along the reverse direction of the electrical order.

Furthermore, during the discharge a significant current is generated multiple times in the earthing system of the circuit, ranging from a few mA to a few A. The earthing circuit is connected to the second energy extraction system at the end of the chain of magnets. In Figure 5.15 the current through the grounding resistor in the earthing system is shown.

In Figure 5.15a and 5.15b the leakage current through the grounding system after t_{PC} , $t_{EE,1}$ and $t_{EE,2}$ is shown. Directly after the power supply is switched off and disconnected, a current of about 150 mA occurs in the grounding system. However,



- (a) Leakage current to ground after the power abort and opening of the first EE system
 (b) Leakage current to ground after the opening of the second EE system

Figure 5.15: Leakage currents to ground in the grounding system of the RB circuit, zoomed around the power abort and the opening times of the two EE systems

after the opening of the first EE system, only a very small oscillation in the EE system occurs. In Figure 5.15b the zoomed time frame around the opening of the second EE system, which is directly connected to the earthing system, is shown. Here, a leakage current of up to 2.6 A occurs in the grounding system, followed by some small oscillations. This corresponds to about 0.023 % of the total current. The opening of the second EE switch also lifts the grounding current to about 20 mA, which then decays together with the circuit current. After each quench in one magnet, additional oscillations in the grounding current occur. The current in the grounding system in the RB circuit is a complex phenomenon, caused by multiple effects in the circuit. Furthermore, as the sampling frequency in the measurements is not sufficiently high to capture the behavior on very small timescales, some features of the earthing current are not fully validated yet and need to be investigated more closely in the future.

However, the simulations of the physical properties in the RB circuit can be used by experts to qualitatively compare the simulated signals to measurements, in case there are no prior measurements of a similar event available. Clear deviations of the measurements from the simulations may indicate pre-cursors or even already occurring faults. Furthermore, the simulations can support the investigation of the behavior of a circuit and quench events with signals, which are not measured but are still of interest for an expert.

Faults may be indicated by pre-cursors or differences in:

- Voltages across magnets which differ from their electrical neighbors, especially during the fast transients in the voltage waves
- Voltage ripples or waves at unexpected times
- Amplitude, frequency and the damping of the occurring voltage waves
- Currents to ground
- Voltages to ground (measured by the so-called voltage feelers, shown in Figure 5.1)
- Voltage differences between apertures in the same magnet

In the future it could be tried, for example, to use machine learning algorithms trained on faulty measurements and simulations of faults, in order to detect precursor of faults. As the amount of data for fault events in the LHC is rather low, the framework of this thesis could help to function as a basis to produce artificial simulation data.

Furthermore, the framework and notebook setting up the simulations can be relatively easily altered by an expert, such that special failure cases are simulated. These could be for example inter-turn shorts in one of the magnets or shorts to ground of

a magnet or one of the components. Moreover, also failure scenarios, such as the failure of a quench heater or failed opening of one energy extraction switch, can be simulated. These simulations then can be used to compare to the measurements to investigate whether a fault or pre-cursor of one might have occurred in the quench event. The framework represents a fast way to generate a model of any RB quench event in a standard configuration. Future work could provide additional functions in the framework to simulate pre-defined fault scenarios.

5.4 Alternative simulation approaches

So far, all shown transients in this Chapter were simulated using the hierarchical co-operative approach. Even though this approach already drastically reduces the required computational effort with respect to a full, co-operative simulation along the entire discharge, the simulation time can still exceed practical feasibility. On a rather average machine, e.g. Intel[©] Core i7 CPU with 3.4 GHz processor and 32 GB of RAM, a simulation of one secondary quench can take around 1-2 hours. A typical quench in an RB circuit results in about 5 to 10 secondary quenches. A full simulation with the described approach can thus take up to 20 hours of computational time. However, most of the occurring events in the RB circuits of the LHC do not show special transients, which deviate strongly from reference simulations. Therefore, it was considered to reduce the physical complexity of the model in favor of a drastically reduced simulation time.

The first approach to reduce the required computational effort drops part of the electrical complexity in the simulations of the sub-events. Instead of the co-operative simulations for each secondary quench, only the electro-magnetic thermal model in STEAM-LEDET is simulated, in order to obtain the resistance development for the final, combined electrical simulation. The simulation of the sub-events thus does only use the simplified electrical circuit, presented in Chapter 2.3.2. As only STEAM-LEDET is used, there is no need for multiple iterations in each time window, as no convergence needs to be reached. Thus, instead of an average of ten iterations per time window, only one simulation is required and the simulation time is greatly reduced. The major limitation of this approach is that the effect of the cold-diodes and their non-linear behavior is neglected and not taken into consideration during the simulation of the coil resistance evolution. However, the final simulation of the full circuit discharge in PSPICE[©] includes this behavior again. This might still lead to unexpected behavior. In the remaining Chapter, this approach will be referred to as "LEDET-only". The difference of obtained transients using "LEDET-only" and the co-operative approach will be discussed later on in this Chapter. The full simulation of a standard RB event with 5 to 10 secondary quenches on an average machine takes about 2 hours (about 20 minutes per secondary quench) in total and thus can reduce the required computational time already by 90%.

A second approach is proposed, which aims at decreasing the computational time

even further by simply interpolating the coil resistance from reference simulations. For this, a total of 16 simulations, using the hierarchical co-operative approach, at different current levels ranging from 0.1 to 12 kA were simulated. The resulting developments of the coil resistances are then used to interpolate linearly for the desired current level. These current levels represent the range of almost zero to above operational current level. In Figure 5.16 the coil-resistances, as well as one example interpolation at a current of 11177 A, are shown. The interpolated coil resistance is then used in the same way as in the previous approaches.

The interpolation of the coil resistance is done by using a simple linear interpolation of all data points for each time step. During the development of this approach also other interpolation schemes, such as polynomial and spline interpolation, were tried. However, these yielded unsatisfactory results, especially for lower current values.

The third approach, applying only an interpolated coil resistance, clearly requires the least computational effort as it only simulates the final, combined PSPICE[©] model with the calculated resistances. As the interpolation only requires a few seconds, the full model is simulated within a few minutes on an average machine. Compared to the hierarchical co-operative approach, this cuts down the required computational time by about 98%.

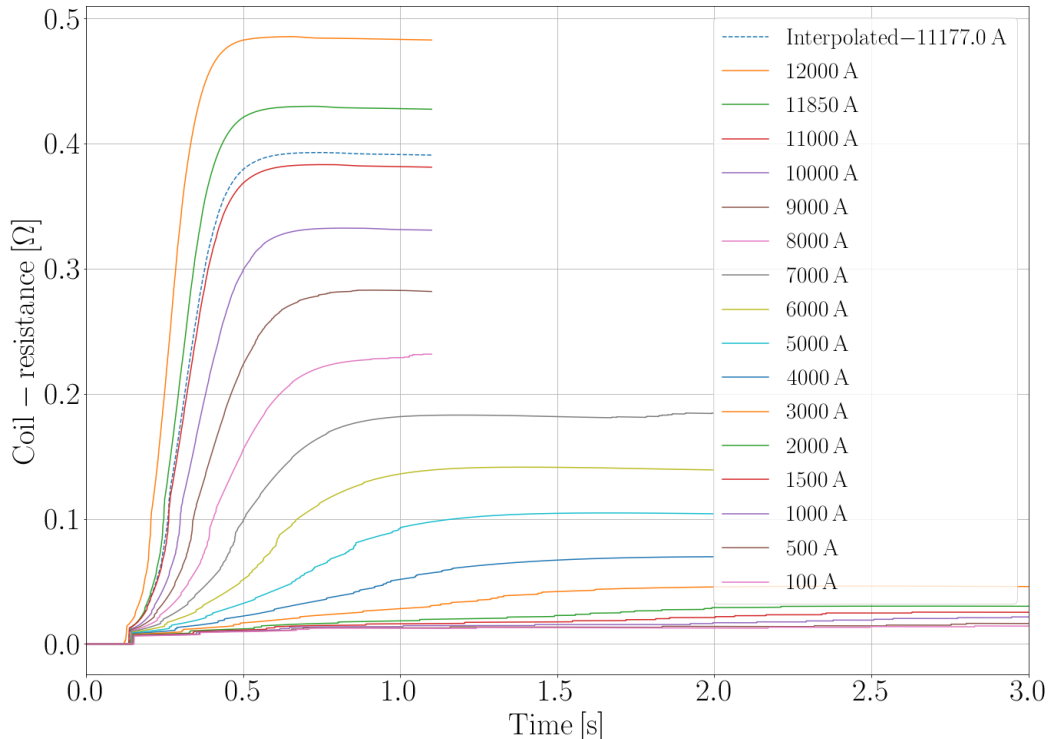
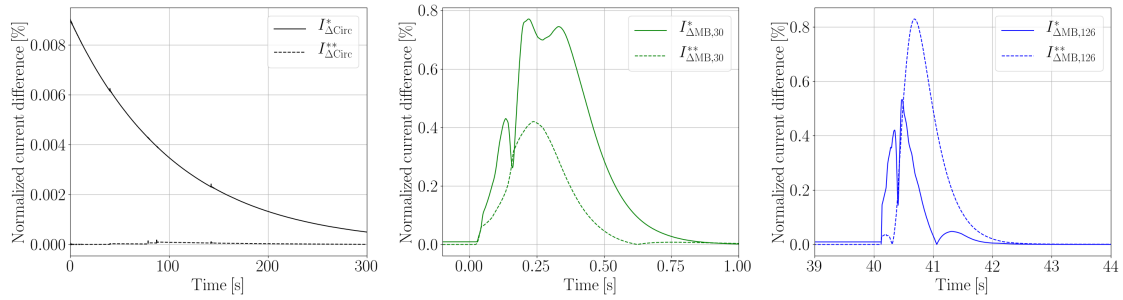


Figure 5.16: Pre-simulated coil-resistances on different current level and the interpolated coil-resistance, used for the final simulation

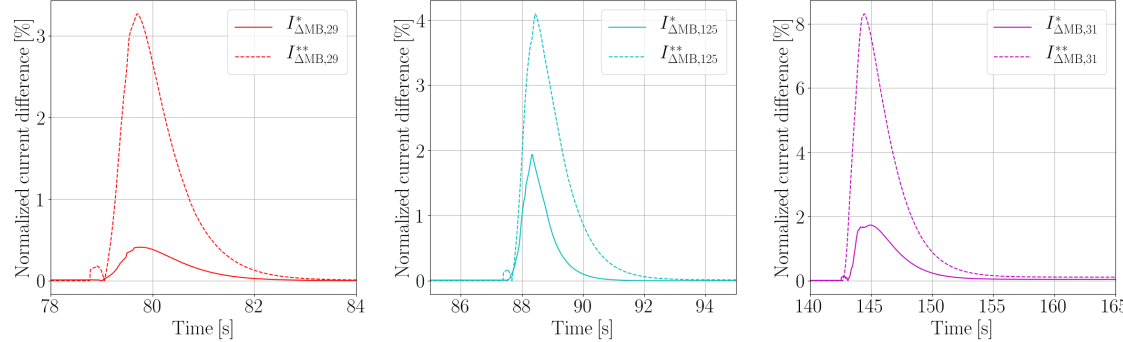
However, the major drawback of this approach is thus, that it neglects the effects of the discharge of the circuit on the magnet discharge. Hence, special events that require the simulation to capture these effects as well as special discharges in the magnets, can not be reproduced by this approach. Nevertheless, most of the RB events during the operation are very similar to the pre-simulated reference simulations, hence this approach can be seen as a fair approximation.

The significant reduction of required time enables the possibility to simulate events in almost real-time. During the investigation of the event by an expert, the simulation of the event using the interpolated coil resistances can run in the background. This way, the user can access the simulated data straight after, for further analysis.

In Figure 5.17 the differences between the two faster proposed approaches and the



(a) Normalized differences in the circuit current (left), current in the magnet with electrical position 30 (first quenching magnet, middle) and electrical position 126 (second quench, right)



(b) Normalized differences in the current in the magnet with electrical position 29 (third quenching magnet, left), electrical position 125 (fourth quench, middle) and with electrical position 31 (fifth quench, right)

Figure 5.17: Normalized differences of the different simulation approaches for the currents in the RB circuit. I_{Δ}^* indicates the difference between the full COSIM simulation and the interpolation approach, I_{Δ}^{**} the difference between full COSIM and the LEDET-only approach.

hierarchical co-operative approach used as a reference are shown. The difference is shown as the normalized, absolute difference of two approaches, given in percentage of the current at the moment of quench.

One can observe that the interpolation approach is closer to the hierarchical co-simulation model than the LEDET-only approach. For the circuit current, the differences between the various approaches are negligible, as they range far below 0.1%. The circuit current is mainly governed by the discharge in the EE system which is included in all models in the same way. For the differences around each quench event, the differences gradually increase, with a spike, usually shortly after the time of quench. While the differences for the quench events at current levels above 7 kA range between 0.1% and 0.8%, they increase for the quench events at current levels below 5 kA to up to 8%. Especially for the lower current case, the difference between "LEDET-only" and the hierarchical co-simulation becomes more significant. However, the difference of the interpolation approach to the co-operative approach is always below 2% and thus in an acceptable range.

Furthermore, in Figure 5.18 the coil resistances for all quench events, calculated with the three approaches are shown. One can observe that the resistances simulated by the hierarchical co-operative approach and calculated by the interpolated approach are almost similar. For the higher current cases, this is also true for the "LEDET-only" approach. The "LEDET-only" starts to diverge from the reference simulation for the lower current cases.

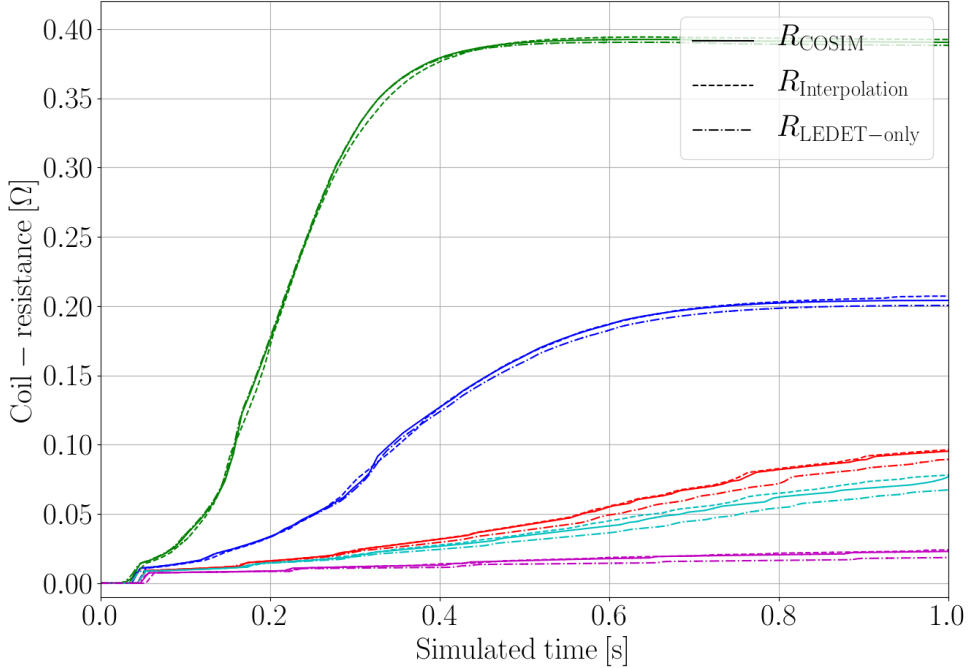


Figure 5.18: Development of the coil-resistances for the different quenching magnets (colors follow Figure 5.12) for the three presented simulation approaches

The third approach, i.e. simulating RB events only based on interpolated coil resistances, is thus recommended for practical use during the investigation of events. These events can be simulated very quickly and only show an acceptable error, compared to the full hierarchical co-operative approach. However, for special transients that deviate from the reference simulations or for simulations of special fault scenarios, the hierarchical co-operative approach is recommended. This approach combines and includes the most physical domains and phenomena. The approach of only using LEDET in combination with a combined PSPICE[©] model is not recommended, as it showed significant deviations from the co-hierarchical simulation for lower current cases.

6 Conclusion and Outlook

Superconducting magnet circuits are one of the key components of the Large Hadron Collider at the European Organization for Nuclear Research. Increasing their availability, ensuring their safe operation as well as simulating and understanding their behavior are some of the main responsibilities of the Performance Assessment and Electrical Quality Assurance section at CERN. For these reasons, the STEAM (Simulation of Transient Effects in Accelerator Magnets) project, consisting of various in-house developed software and a framework supporting in-house and commercial simulation tools, was initiated. STEAM allows tackling the multi-scale, multi-physics and multi-rate challenge of modelling and simulating superconducting magnets. One goal of this project is a general magnet library, containing all magnets used in LHC operation as well as prototypes and R&D magnets. One challenge of such a library is the validation of the models, hence ensuring their reliability and resilience. The validation includes, among other tasks, the determination of unknown model parameters, which are difficult to measure or estimate. Previously, this was a time-consuming and laborious task.

The main goal of this thesis was thus to develop and test a framework capable of speeding up and simplifying this validation process. Moreover, it should provide the possibility to simulate and investigate the behavior and effects occurring in superconducting magnets and circuits with automatic simulations. The newly developed framework of this thesis is embedded into the programming interface of the STEAM Jupyter notebooks used for the generation of the models. It provides functions and algorithms to automatically generate large sets of simulations, applying different parameter values and thus simulating all unknown parameter combinations within a pre-defined physical range. The best parameter combination can be found by automatically comparing the results of the simulations to measurements from LHC operation or magnet testing. The framework provides extensive plots and calculates error metrics. Moreover, in the same manner, larger sets of simulations of already validated magnet or circuit models can be generated and can simulate and predict the impact of various events, operation scenarios, or failure cases.

After introducing the general topic of superconductivity, CERN accelerator magnets and quench protection in Chapter 1, the general modelling and simulation approach, developed in the STEAM framework and applied in this thesis, was described in Chapter 2. In the scope of this thesis, mostly the software STEAM-LEDET, simulating electro-thermal magnetic magnet models as well as STEAM-COSIM, co-operatively simulating the STEAM-LEDET models and electrical circuit models in PSPICE[©], were described and used. Chapter 3 then shows the application of the framework in two use-cases.

First, the model of a self-protecting superconducting MCBYH magnet, powered on current levels up to 120 A, was validated by simulating a set of 288 simulations. The general agreement of simulation and measurement for the best found unknown

model parameter values is very good and the quench load error ranges below 1.5%. It was shown that the residual resistivity ratio (RRR) has a significant impact on the simulated quench transients in the magnet. The scaling factor for the effective transverse resistivity $f_{\rho,\text{eff}}$, governing inter-filament coupling losses, on the contrary, has a smaller impact. The proposed best found parameter set is $RRR \in [75, 100]$ and $f_{\rho,\text{eff}} \in [2.1, 2.5]$.

Second, the group of LHC separation and recombination dipoles was validated. For each of the three validated magnets from this group, a set of 1296 simulations was performed. It was shown that varying the conductor RRR has the most significant impact on the transients in the magnet. However, also the infiltrated helium fraction f_{He} and $f_{\rho,\text{eff}}$ have a not negligible impact. As the best parameter set, the parameter values $RRR \in [68, 100]$, $f_{\text{He}} \in [0, 1] \%$, $f_{\rho,\text{eff}} \in [1, 2]$ and for the strand cross-contact resistance $R_C \in [1 \cdot 10^{-3}, 1 \cdot 10^{-5}] \Omega$ are proposed. The agreement between measurement and the simulations was very good and the quench load error ranged below 2%.

The models of these magnets are now part of the STEAM LHC superconducting circuit library and can be used to simulate operation scenarios, failure cases or to investigate their behavior in more detail. For example, the validated models can be used in a co-operative simulation to simulate such events. Furthermore, the validation procedure can be applied similarly to other magnets, for example from LHC, High Luminosity-LHC or the Future Circular Collider.

Moreover, in Chapter 4, two more cases were discussed, showing the application of the framework in order to predict, assess, and investigate the impact of different quench scenarios as well as the occurrence of quench-back.

For the latter, various current levels were simulated for the 28 circuit types in the family of 600 A LHC circuits. Each simulated transient was analyzed with a particular focus on the occurrence of quench-back. For each 600 A LHC circuit the expected quench-back current level was proposed and some transients were analyzed in more detail. This information can potentially help deducing precursors of faulty magnets if the measured behavior deviates from the expected transients.

Furthermore, the validated magnet and circuit models of the self-protecting MCBYH magnet from Chapter 3.2 was used to investigate the impact of different quench locations. In total, 96 different locations throughout the coil were simulated and compared. It was shown that these can significantly change the transients in the MCBY magnet. Differences of up to 25% in the hot-spot temperature were observed. Hence, the automated simulations performed with the framework gave more insights into the behavior of the model regarding the initial quench location, which for LHC magnets is usually unknown.

Future work could enhance the potential of the newly developed framework towards predicting and simulating magnet and circuit behavior. For example, by comparing the simulations and turn-wise voltages to multi-channel voltage data obtained during magnet prototype testing, one could deduce the initial quench location more

precisely. Moreover, enhancing the framework to simulate automatically straight after the model generation relevant electrical failure cases, such as coil-to-ground or coil internal short circuits could be interesting and provide helpful insights. In addition, simulating other failure scenarios, such as failing quench protection systems including failing switches or quench heater strips represents future work that can be based on the now existing framework.

Chapter 5 discussed the possibility to include and extend the proposed framework to simulate multiple quench events of the LHC main bending dipoles in almost real-time. The applied concept of hierarchical co-operative simulations was discussed and various results from the transients during a multiple quench-event were shown. Moreover, also different simulation approaches were shown, which drop some modelling accuracy in favor of a reduced simulation time. It was shown that interpolating the evolution of the coil resistance from reference simulations, without simulating each event independently, can greatly decrease the simulation time by about 98%, while still preserving good agreement with the full co-operative simulations. Future work could use this proof-of-concept to realize an automatic real-time simulation solution to generate and run models of occurring events in the LHC main bending dipoles fully automatically in real-time.

This thesis shows with different use cases that the newly developed framework can simplify and speed up the validation of a superconducting magnet model within the STEAM framework. Furthermore, the general concept could be applied in the same way to other simulation frameworks. The validated magnet models show excellent agreement with measurements. Moreover, additional insights into the magnets can be easily obtained. This framework thus can help and ease the validation of future magnet and circuit models and can speed up the process significantly. It can also be used to simulate failure cases, worst-cases or unusual events in order to examine their behavior and impact. It has assisted and will assist the analysis of events in LHC circuits during hardware commissioning campaigns and LHC operation.

Appendices

A Superconductors

Table 14: Superconducting materials and their properties

| Name of material | Class | Chemical formula | Critical temperature @ 0T | Upper Critical field @ 0K |
|---|-----------------------|--|---------------------------|---------------------------|
| Titanium [63] | Element - Type I SC | Ti | 0.39 K | 0.01 T |
| Niobium [63] | Element - Type I SC | Nb | 9.26 K | 0.82 T |
| Tin [63] | Element - Type I SC | Sn | 3.72 K | 0.09 T |
| Niobium-Titanium [63] | Compound - Type II SC | Nb-Ti | 9.2 K | 14.5 T |
| Niobium-Tin [64] | Compound - Type II SC | Nb ₃ Sn | 18 K | 28 T |
| Magnesium diboride [65] | Compound - Type II SC | MgB ₂ | 39 K | 74 T |
| Yttrium barium copper oxide (YBCO) [10] | Cuprate - Type II SC | YBa ₂ Cu ₃ O _{7-x} | around 100 K | 120-250 T |
| Bismuth strontium calcium copper oxide (BSCCO) [10] | Cuprate - Type II SC | Bi ₂ Sr ₂ CuO _{6+x} | around 100 K | > 200 T |
| Hydrogen sulfide at 160 GPa pressure [66] | Compound - Type II SC | H ₃ S | 260 K | 65 T |

B Strand characteristics

Table 15: Characteristics of strands, used in LHC magnets [1, 21]

| Strand name | Super conductor | Strand diameter | Stabilizer/SC ratio | Number of filaments | Filament diameter | Filament twist pitch |
|-------------|-----------------|-----------------|---------------------|---------------------|-------------------|----------------------|
| 01 | Nb-Ti | 0.825 mm | 1.65 | 8735 | 6 μm | 18 mm |
| 02 | Nb-Ti | 1.065 mm | 1.95 | 6409 | 7 μm | 15 mm |
| 05 | Nb-Ti | 0.480 mm | 1.75 | 2327 | 6 μm | 15 mm |
| 06 | Nb-Ti | 0.735 mm | 1.25 | 6669 | 6 μm | 15 mm |

C Cable characteristics

Table 16: Characteristics of multi-stranded cables in LHC magnets [1]

| Cable name | Number of strands | Strand-type | Bare cross-section | Insulated cross-section | Strand twist pitch | Insulation material |
|------------|-------------------|-------------|------------------------|-------------------------|--------------------|---------------------|
| 01 | 28 | 01 | 22.348 mm ² | 24.825 mm ² | 0.100 m | Kapton |
| 02 | 36 | 02 | 28.691 mm ² | 31.201 mm ² | 0.115 m | Kapton |
| 03 | 36 | 02 | 22.348 mm ² | 24.488 mm ² | 0.100 m | Kapton |
| 04 | 36 | 05 | 7.436 mm ² | 8.214 mm ² | 0.066 m | Kapton |
| 05 | 34 | 05 | 6.985 mm ² | 7.720 mm ² | 0.066 m | Kapton |
| 06 | 22 | 06 | 10.540 mm ² | 11.309 mm ² | 0.066 m | Kapton |
| 07 | 34 | 05 | 6.985 mm ² | 7.720 mm ² | 0.066 m | Kapton |

Table 17: Characteristics of single-stranded cables, used in LHC magnets [1], guess values are indicated with (*)

| Cable name | Bare cross-section | Insulated cross-section | Stabilizer/SC ratio | Filament twist pitch | Insulation material |
|------------|----------------------|-------------------------|---------------------|----------------------|---------------------|
| Corr-01 | 0.13 mm ² | 0.16 mm ² | 4.4 | 0.015 m(*) | Kapton |
| Corr-02 | 0.21 mm ² | 0.24 mm ² | 4.4 | 0.015 m(*) | Kapton |
| Corr-03 | 0.69 mm ² | 0.79 mm ² | 1.75 | 0.015 m(*) | Kapton |
| Corr-04 | 1.30 mm ² | 1.45 mm ² | 1.75 | 0.015 m(*) | Kapton |

D LHC magnets

Table 18: Characteristics of LHC magnets [1, 11]

| Magnet name | Number of magnets | Number of apertures | Number of poles | Operating temperature T_0 | Nominal current I_{nom} | Magnetic length l_{mag} | Inductance L_{mag} |
|---|-------------------|---------------------|-----------------|-----------------------------|----------------------------------|----------------------------------|-----------------------------|
| Main magnets in the arc | | | | | | | |
| MB | 1232 | 2 | 2 | 1.9 K | 11850 A | 14.3 m | 0.102 H |
| MQ | 392 | 2 | 4 | 1.9 K | 11870 A | 3.1 m | 0.0056 H |
| Separation & recombination dipoles | | | | | | | |
| MBX | 4 | 1 | 2 | 1.9 K | 5800 A | 9.45 m | 0.0026 H |
| MBRS | 4 | 1 | 2 | 4.5 K | 5520 A | 9.45 m | 0.0026 H |
| MBRC | 8 | 2 | 2 | 4.5 K | 6000 A | 9.45 m | 0.0052 H |
| MBRB | 2 | 2 | 2 | 4.5 K | 5520 A | 9.45 m | 0.0052 H |
| Lattice corrector | | | | | | | |
| MCBCH/V | 168 | 1 | 2 | 1.9/4.5 K | 100 A | 0.904 m | 2.84 H |
| MCOSX | 8 | 1 | 8 | 1.9 K | 100 A | 0.138 m | 0.0032 H |
| MCOX | 8 | 1 | 8 | 1.9 K | 100 A | 0.137 m | 0.0044 H |

Table 18: Characteristics of LHC magnets [1, 11]

| Continuation of Table 18 | | | | | | | |
|---|-------------------|---------------------|-----------------|-----------------------------|----------------------------------|----------------------------------|-----------------------------|
| Magnet name | Number of magnets | Number of apertures | Number of poles | Operating temperature T_0 | Nominal current I_{nom} | Magnetic length l_{mag} | Inductance L_{mag} |
| Spool piece corrector | | | | | | | |
| MCS | 2464 | 1 | 6 | 1.9 K | 550 A | 0.11 m | 0.0008 H |
| MCD | 1232 | 1 | 10 | 1.9 K | 550 A | 0.066 m | 0.0004 H |
| MCO | 1232 | 1 | 8 | 1.9 K | 100 A | 0.066 m | 0.0004 H |
| MCSSX | 8 | 1 | 6 | 1.9 K | 100 A | 0.132 m | 0.0078 H |
| MCSX | 8 | 1 | 6 | 1.9 K | 100 A | 0.576 m | 0.0047 H |
| MCTX | 8 | 1 | 12 | 1.9 K | 80 A | 0.615 m | 0.0292 H |
| Insertion quadrupoles & correctors | | | | | | | |
| MQM | 38 | 2 | 4 | 1.9/4.5 K | 5390 A | 3.4 m | 0.0151 H |
| MQMC | 12 | 2 | 4 | 1.9/4.5 K | 5390 A | 2.4 m | 0.0107 H |
| MQML | 36 | 2 | 4 | 1.9/4.5 K | 5390 A | 4.8 m | 0.0213 H |
| MQY | 24 | 2 | 4 | 4.5 K | 3610 A | 3.4 m | 0.074 H |
| MQTLH | 24 | 2 | 4 | 4.5 K | 400 A | 1.3 m | 0.120 H |
| MQTLI | 36 | 2 | 4 | 1.9 K | 550 A | 1.3 m | 0.120 H |

Table 18: Characteristics of LHC magnets [1, 11]

| Continuation of Table 18 | | | | | | | |
|--------------------------------------|-------------------|---------------------|-----------------|-----------------------------|----------------------------------|----------------------------------|-----------------------------|
| Magnet name | Number of magnets | Number of apertures | Number of poles | Operating temperature T_0 | Nominal current I_{nom} | Magnetic length l_{mag} | Inductance L_{mag} |
| Inner triplets and correctors | | | | | | | |
| MQXA | 16 | 1 | 4 | 1.9 K | 6450 A | 6.37 m | 0.09 H |
| MQXB | 16 | 1 | 4 | 1.9 K | 11950 A | 5.5 m | 0.019 H |
| MCBXH | 24 | 1 | 2 | 1.9 K | 550 A | 0.45 m | 0.287 H |
| MCBXV | 24 | 1 | 2 | 1.9 K | 550 A | 0.48 m | 0.175 H |
| MQSX | 8 | 1 | 4 | 1.9 K | 550 A | 0.223 m | 0.014 H |
| Lattice correctors | | | | | | | |
| MCBH/V | 752 | 1 | 2 | 1.9 K | 55 A | 0.647 m | 6.02 H |
| MCBYH/V | 76 | 1 | 2 | 1.9 K | 88 A | 0.9 m | 5.27 H |
| MQS | 32 | 2 | 4 | 1.9 K | 550 A | 0.32 m | 0.031 H |
| MQT | 160 | 2 | 4 | 1.9 K | 550 A | 0.32 m | 0.031 H |
| MS | 688 | 1 | 6 | 1.9 K | 550 A | 0.369 m | 0.036 H |
| MSS | 64 | 1 | 6 | 1.9 K | 550 A | 0.369 m | 0.036 H |
| MO | 168 | 2 | 8 | 1.9 K | 550 A | 0.32 m | 0.00015 H |

E LHC circuits

Table 19: List of LHC circuits and their specifications [1, 11]

| Circuit family | Circuit name | Magnet name | Number of magnets | Cable type | Strand type | Protection type | Nominal current | Function |
|----------------|--------------|-----------------|-------------------------|-------------------|-------------|-----------------------------|-----------------|--|
| RB | RB | MB | 154 | 01/02 | 01/02 | QH, cold by-pass diode & EE | 11850 A | Main bending dipole |
| RQ | RQF | MQ | 47/51 | 03 | 02 | QH & EE | 11850 A | Main focusing quadrupole |
| RQ | RQD | MQ | 47/51 | 03 | 02 | QH & EE | 11850 A | Main de-focusing quadrupole |
| RQX | RQX | MQXA & MQXB | 4 | Special | | QH | 7180 A | Inner triplet correctors |
| IPD | RD | MBX/ MBRC/ MBRB | 1 | Special | | QH | 5800 A | Separation and recombination dipoles |
| IPQ | RQ | MQY/ MQM | 2 / 4 | 04/ 05/ 06/ 07 | 05/ 06 | QH | 3600- 5400 A | Matching of insertion optics |
| 600 A | various | various | various, see Table 9 | Corr-03 | - | self-protection / EE | 550 A | Various functions, mainly correctors & tuning magnets, see Table 9 |
| 80-120 A | various | various | 1 | Corr-01/2 | - | self-protection | 55-110 A | Various functions, mainly correctors & tuning magnets |

F Annex to Chapter 3

Listing 1: Coding example to prepare parts of the parameter sweep for the IPD magnet MBRB (more detailed explanation in Chapter 3.3)

```

# Import necessary packages
from steam_nb_api.ledet.ParameterSweep import *
from steam_nb_api.ledet.ParametersLEDET import ParametersLEDET
from steam_nb_api.ledet.Simulation import RunSimulations
from steam_nb_api.ledet.SimulationEvaluation import EvaluateSimulations

# Provide location of the magnets reference LEDET Excel-File
testfile = "C:\\\\Users\\\\steam-notebooks\\\\steam-ledet-input\\\\MBRB\\\\
MBRB_0.xlsx"
# Create an ParameterLEDET object, containing all magnet informations
a = ParametersLEDET()
a.readLEDETExcel(testfile)
# Create a Sweep object and standard value for amount of data points
## (obj ParametersLEDET, int data-points)
Sw = MinMaxSweep(a, 6)

# Set the parameter to sweep and their ranges
## Setting f_rho_eff in [1,3]
Sw.addParameterToSweep('f_rho_eff_inGroup', 1, 3)
## Setting f_He in [0, 6] %
## special function as f_internal and f_external need to be set
Sw.addHeliumCrossSection(0, 6)
## Setting Rc in [10e-6, 10e-3]
Sw.addParameterToSweep('R_c_inGroup', -6, -3, type='logarithmic')
## Setting RRR in [35,200]
Sw.addParameterToSweep('RRR_Cu_inGroup', 35, 200)
## Setting quenches in different positions at different times
## ('VariableToSweep', [Affected Turns], [Times])
Sw.addQuenchSweep("tStartQuench",[1,2,3,4,5,6],
[-0.15, -0.16, -0.17, -0.18, -0.19, -0.2])
## Add different current level to the combinations
## (int nominalCurrent, int data-points)
Sw.addCurrentSweep(6650, 30)

## Add customized vector to the sweep matrix
values = np.linspace(0,100,12)
Sw.addParameterToSweep_Vector("RRR_Cu_inGroup",values)

```

```
# Generate all combinations
Sw.generatePermutations()

# To print out all parameters and all combinations
print(Sw.ParametersToSweep)
print(Sw.SweepMatrix)

# Prepare all simulations files
## (MagnetName, Simulation-directory)
Sw.prepareSimulation('MBRB', 'C:\\\\Users\\\\STEAM\\\\LEDET\\\\')

# Run all simulations
## (Simulation-directory, LEDET version, MagnetName)
RunSimulations('C:\\\\Users\\\\STEAM\\\\LEDET\\\\', 'LEDET_v2', 'MBRB')

# Evaluate all simulations and compare to measurement
## (Output-directory, MagnetName, Measured data, obj ParametersLEDET)
EvaluateSimulations("C:\\\\Users\\\\STEAM\\\\LEDET\\\\Output","MBRB",
'C:\\\\Users\\\\MeasData\\\\MBRB_Data.csv', Sw)
```

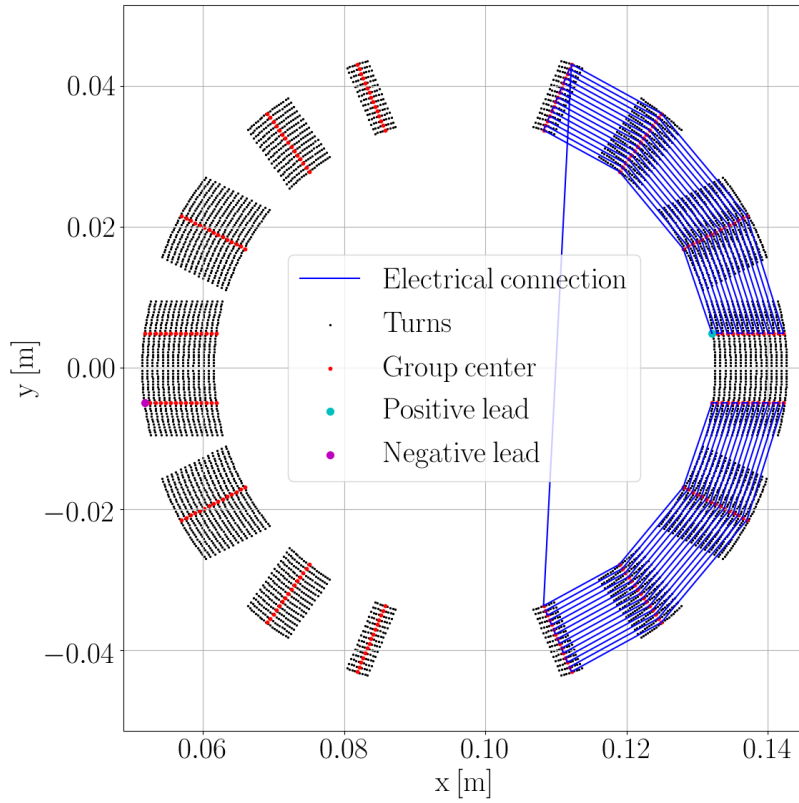


Figure F.1: Electrical connections of the different groups of conductor (here: layers) in the MCBYH magnet. Only the Go-lines are shown, the return lines are in the respective other pole.

Calculation of minimal required quench energy

The minimal required energy to quench a turn E_q [J] can be calculated by the formula:

$$E_q = V_q \cdot \Delta H_{2K,7K} \quad (\text{F.1})$$

where V_q [m^{-3}] is the minimal required quenched volume, following [15]:

$$V_q = A_{\text{Cable}} \cdot l_q \quad (\text{F.2})$$

$$l_q = \sqrt{\frac{2\kappa_{\text{Cu}}(T)(T_c - T_{\text{op}})}{J_{\text{op}}^2 \rho_{\text{Cu}}(T, B, RRR)}} \quad (\text{F.3})$$

with A_{Cable} [m^2] the cable cross-section, l_q [m] minimal required normal zone, T_{op} [K] operational temperature, $\kappa_{\text{Cu}}(T)$ [$\text{W m}^{-1} \text{K}^{-1}$] electrical conductivity of copper, $\rho_{\text{Cu}}(T, B, RRR)$ [Ωm] electrical resistivity and J_{op}^2 [$\frac{\text{A}}{\text{m}^2}$] the operational current density. Furthermore, $\Delta H_{2K,7K}$ [$\frac{\text{kJ}}{\text{m}^{-3}}$] represents the difference of thermal enthalpy of

copper for 2 K (operational temperature) and 7 K (approximated critical temperature at nominal current). The values for enthalpy, electrical conductivity and resistivity were taken from fits, provided by NIST [51]. The minimal required normal zone refers to the border between cryogenic stability and quench development. A normal zone which is longer than l_q will grow because the heat generation exceeds the cooling, while a shorter normal zone will collapse and recover full superconductivity.

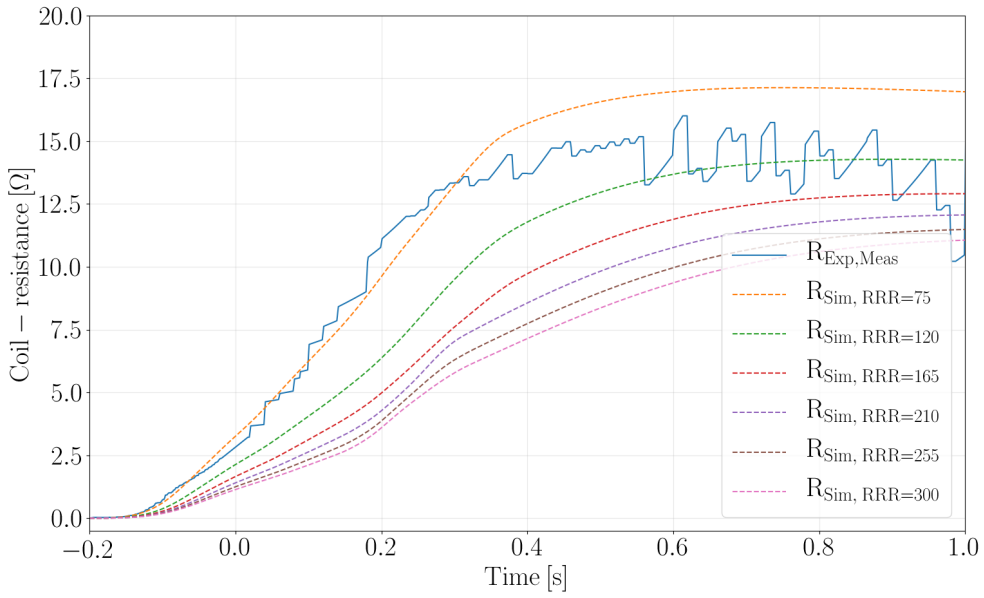


Figure F.2: Evolution of the simulated coil resistance compared to experimental coil-resistance for the different applied values for RRR. $f_{\rho, \text{eff}} = 2.1$ and quench position 4 are fixed.

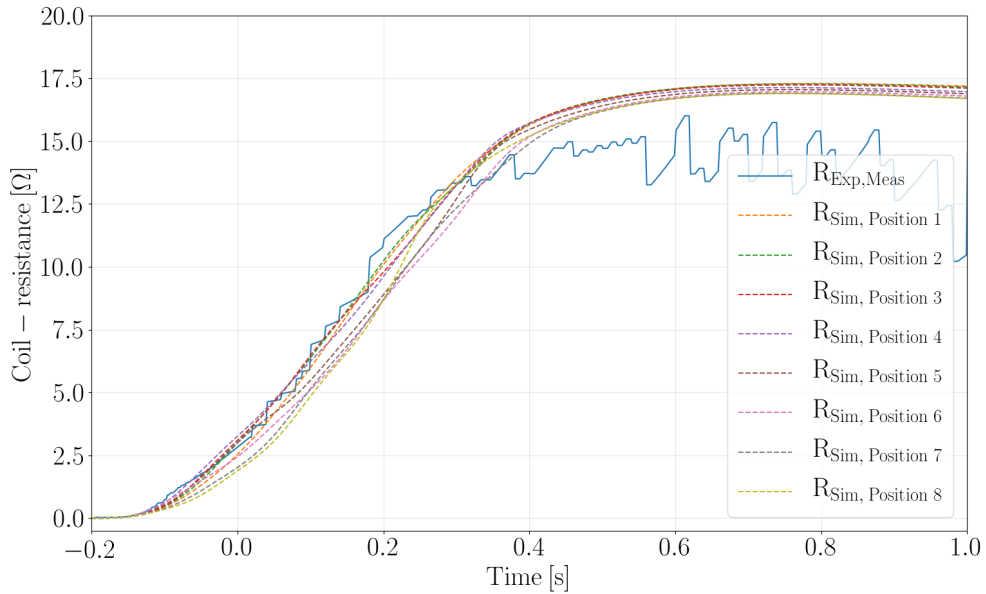


Figure F.3: Evolution of the simulated coil resistance compared to experimental coil-resistance for the different investigated quench positions. $\text{RRR}=75$ and $f_{\rho,\text{eff}} = 2.1$ are fixed.

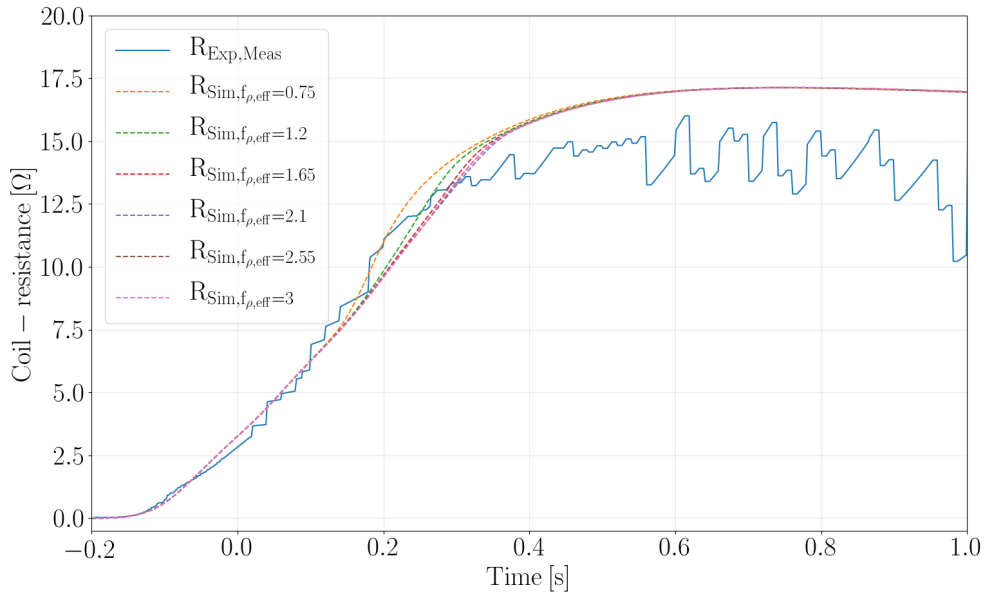


Figure F.4: Evolution of the simulated coil resistance compared to experimental coil-resistance for the different applied values for $f_{\rho,\text{eff}}$. $\text{RRR} = 75$ and quench position 4 are fixed.

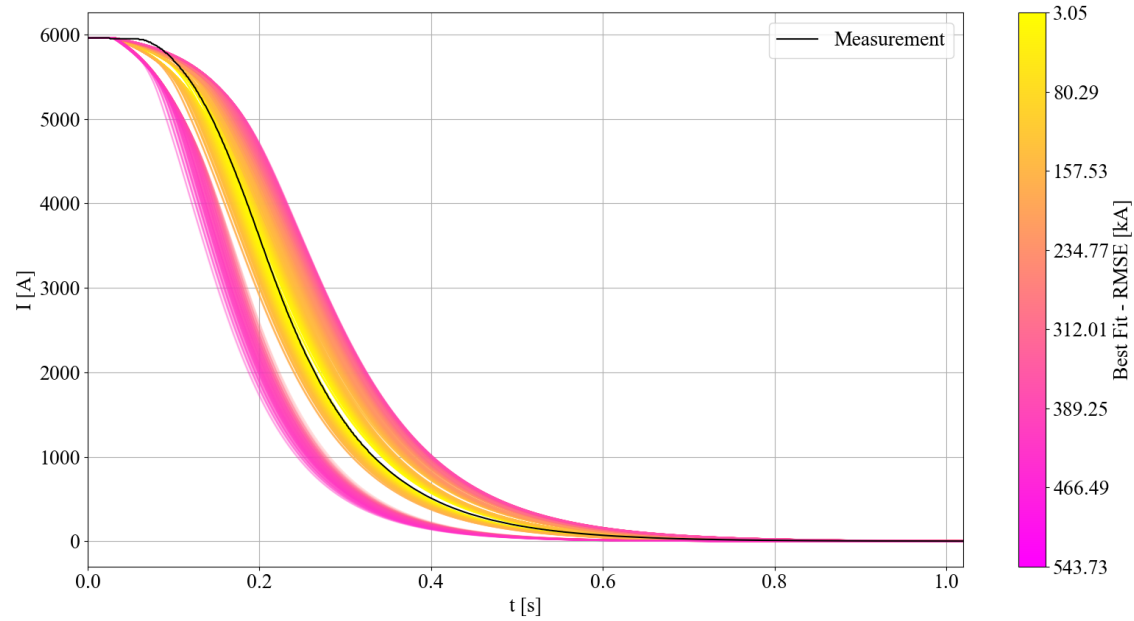


Figure F.5: Current decay in the MBRC magnet for all performed simulations, compared to measurements, after a fast power abort at $t_{PC} = 0$ s and quench heater firing at $t_{QH} = 2$ ms.

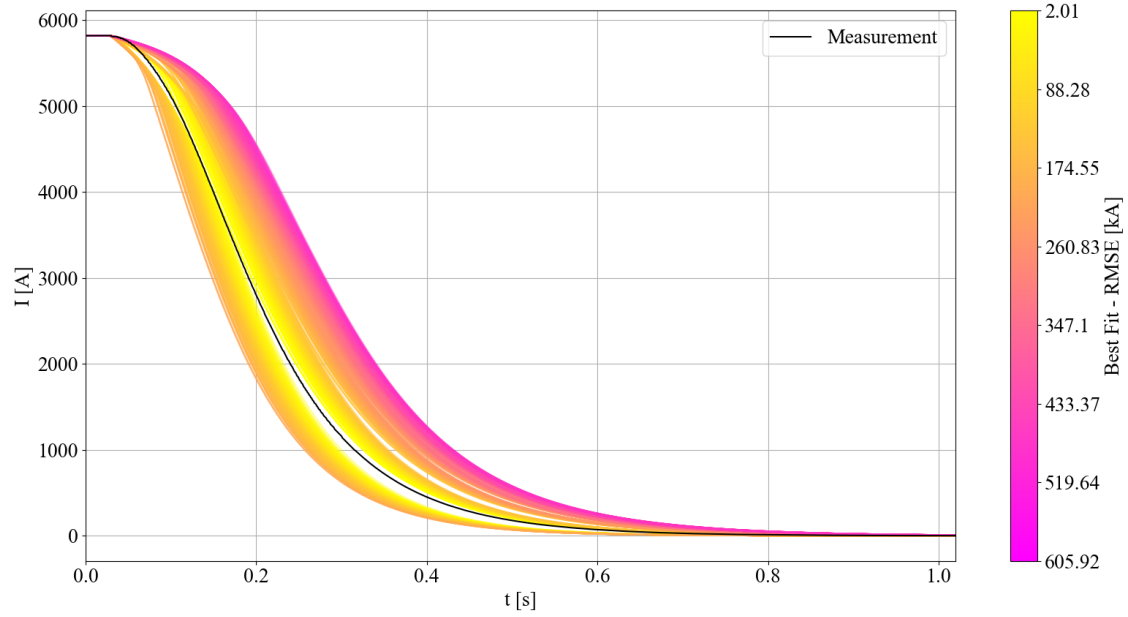
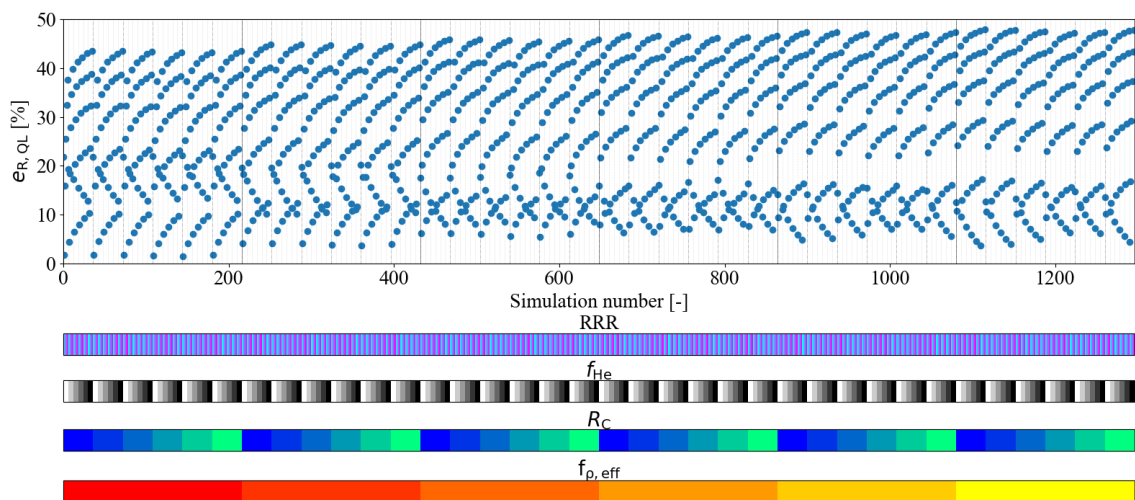
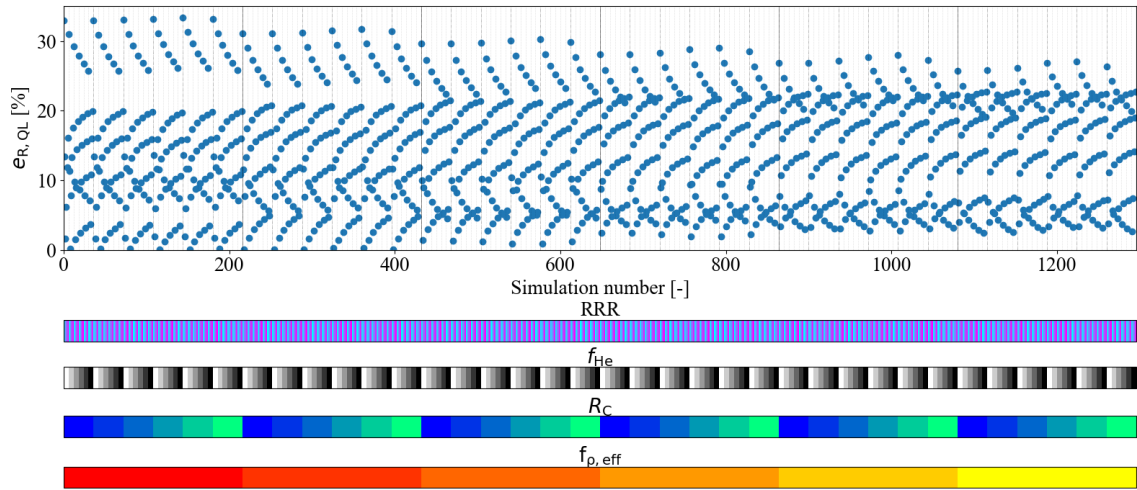


Figure F.6: Current decay in the MBRS magnet for all performed simulations, compared to measurements, after a fast power abort at $t_{PC} = 0$ s and quench heater firing at $t_{QH} = 2$ ms.



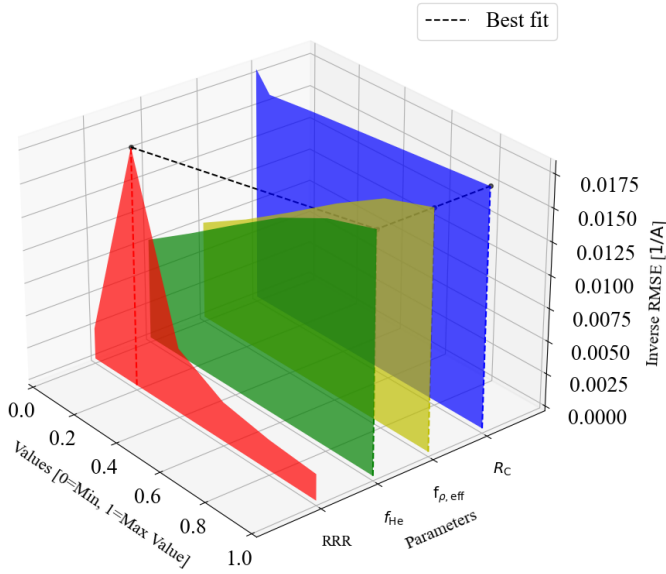


Figure F.9: Ablation analysis of the MBRC model to the selected parameter. Dependency of the inverse RMSE to changing one parameter at a time. If not changed, values are fixed to $\text{RRR} = 101$, $f_{\rho, \text{eff}} = 1.4$, $f_{He} = 1\%$ and $R_C = 4 \cdot 10^{-6} \Omega$.

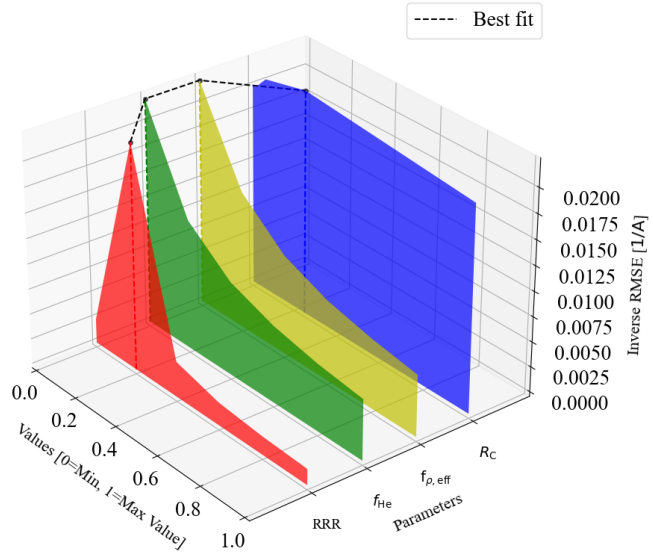


Figure F.10: Ablation analysis of the MBRS model to the selected parameter. Dependency of the inverse RMSE to changing one parameter at a time. If not changed, values are fixed to $\text{RRR} = 68$, $f_{\rho, \text{eff}} = 1$, $f_{He} = 0\%$ and $R_C = 2.5 \cdot 10^{-4} \Omega$.

G Annex to Chapter 4

Listing 2: Coding example to prepare all of the 600 A quench-back simulations

```
# Import necessary packages
from steam_nb_api.utils.STEAMLib_simulations import *

# Import parameter file, containing all informations
ParameterFile = "600A_Circuit_Param_Table.csv"
# Define current level to be simulated
currents = [100,200,300,350,400,450,500,550,600]
# Define which specific circuits to simulate
circuit = ["RCS.A45B2","RQ6.L7B1","RQS.A45B1"]

# Loop through all circuits and set-up for each circuit all current-level
for i in range(len(circuit)):
    # Load parameter file
    LSS = LibSim_setup(circuit[i], ParameterFile)
    # Load all user-specific directories
    # In CERN environment: '' chooses the username, to look for the "username.
    # yaml" file
    LSS.load_config('')
    # Set-up all simulations
    # LSS.SetUpSimulation ('Type', 'CurrentLevel', 'Additional Stimuli', 'Append,
    # if all combined in a single batch file ')
    LSS.SetUpSimulation('FPA', currents, AppendStimuli = '600A/EESTimuli.stl',
    Append = True)
```

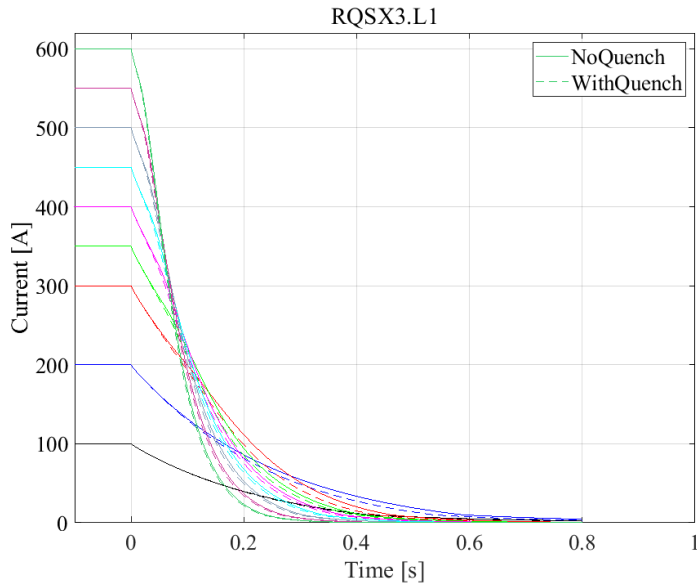


Figure G.11: Simulated current discharge on different current level in the RQSX3.L1 circuit, after the power supply is switched off at $t_{PC} = 0$ s, for the simulations with and without an initial quench, representing a case with 'medium' quench-back significance

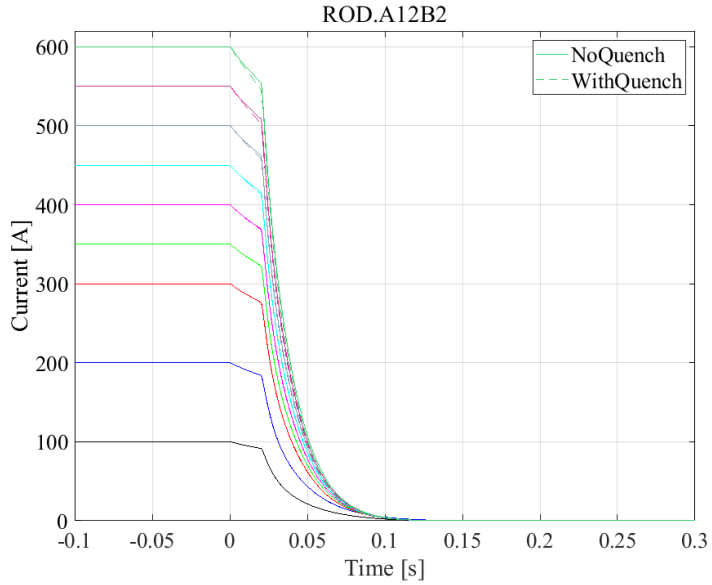


Figure G.12: Simulated current discharge on different current level in the ROD.A12B2 circuit, after the power supply is switched off at $t_{PC} = 0$ s, for the simulations with and without an initial quench, representing a case with 'low' quench-back significance

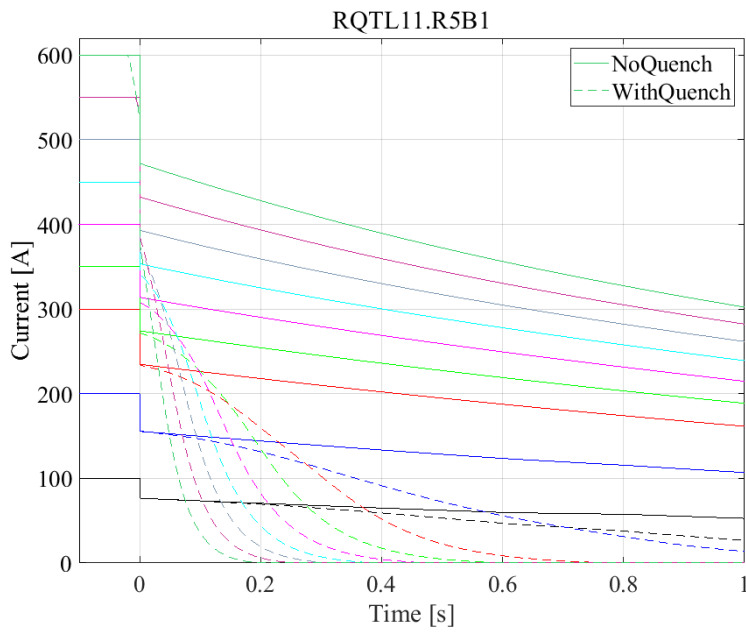


Figure G.13: Simulated current discharge on different current level in the RQTL11.R5B1 circuit, after the power supply is switched off at $t_{PC} = 0$ s, for the simulations with and without an initial quench, representing a case with no expected quench-back

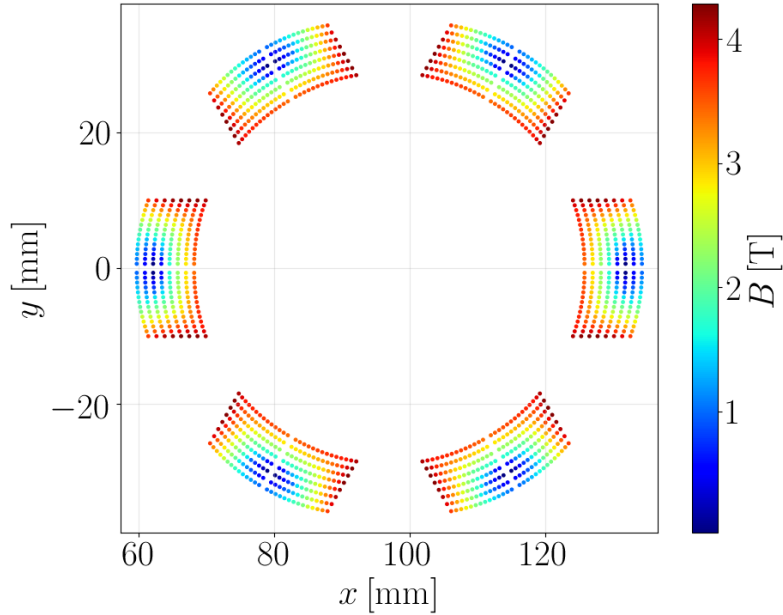


Figure G.14: Magnetic field in the coil of one aperture of the MS magnet, calculated using ROXIE [43, 44] and including iron yoke effects

Listing 3: Coding example to prepare the MCBYH quench location simulations

```
# Import necessary packages
from steam_nb_api.ledet.ParameterSweep import *
from steam_nb_api.ledet.ParametersLEDET import ParametersLEDET
from steam_nb_api.ledet.Simulation import RunSimulations

# Provide location of the magnets reference LEDET Excel-File
testfile = "C:\\\\Users\\\\steam-notebooks\\\\steam-ledet-input\\\\MCBYH_1AP
\\\\MCBYH_1AP_0.xlsx"
# Create an ParameterLEDET object, containing all magnet informations
a = ParametersLEDET()
a.readLEDETEExcel(testfile)
# Create a Sweep object and standard value for amount of data points
Sw = MinMaxSweep(a, 1)
# Include the desired turns and times of quenches [short version]
Sw.addQuenchSweep("tStartQuench", [[ 1], [ 25], [ 351], [ 375], [...]],
[[-0.175], [-0.175], [-0.175], [-0.175], [...]])
# Proceed with preparation as in Listing 1
Sw.prepareSimulation('MBRB', 'C:\\Users\\STEAM\\LEDET\\')
Sw.generatePermutations()
RunSimulations('C:\\Users\\STEAM\\\\LEDET\\', 'LEDET_v2', 'MCBYH_1AP')
```

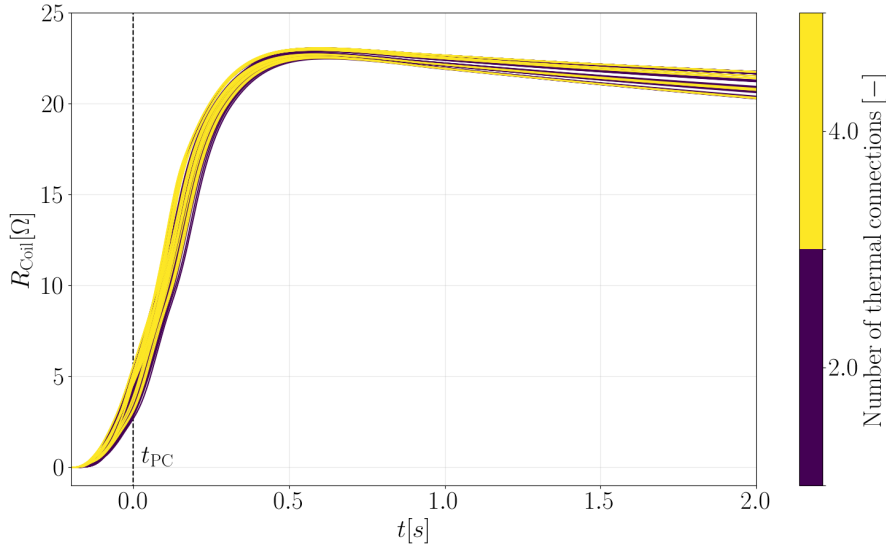


Figure G.15: Development of the coil resistance in an FPA at $t_{\text{PC}} = 0$ s for all selected initial quench positions from nominal current. Colors indicate the number of neighboring turns to the first quenching turn.

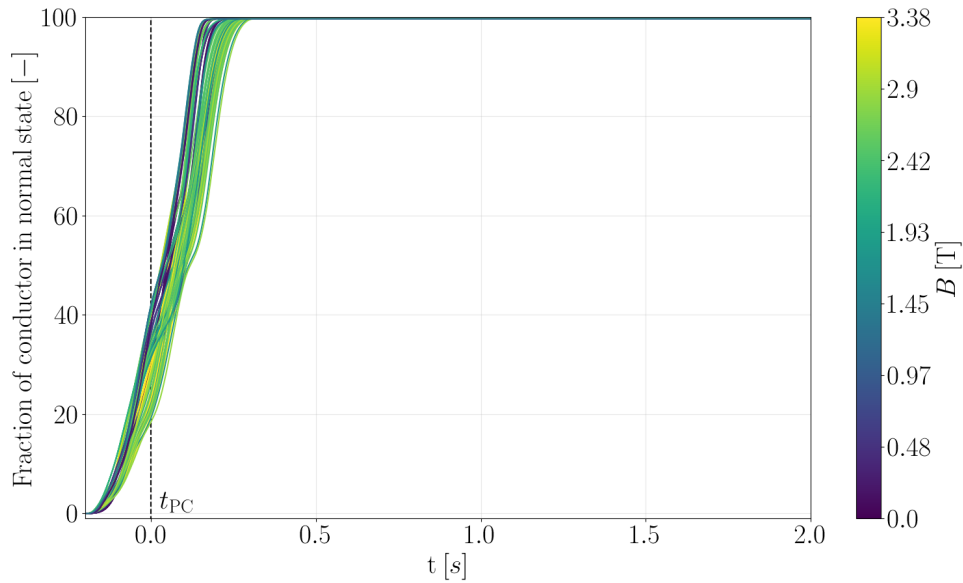


Figure G.16: Development of the amount of conductor in normal state in an FPA at $t_{PC} = 0$ s for all selected initial quench positions from nominal current. Colors indicate the initial magnetic field in the first quenching turn.

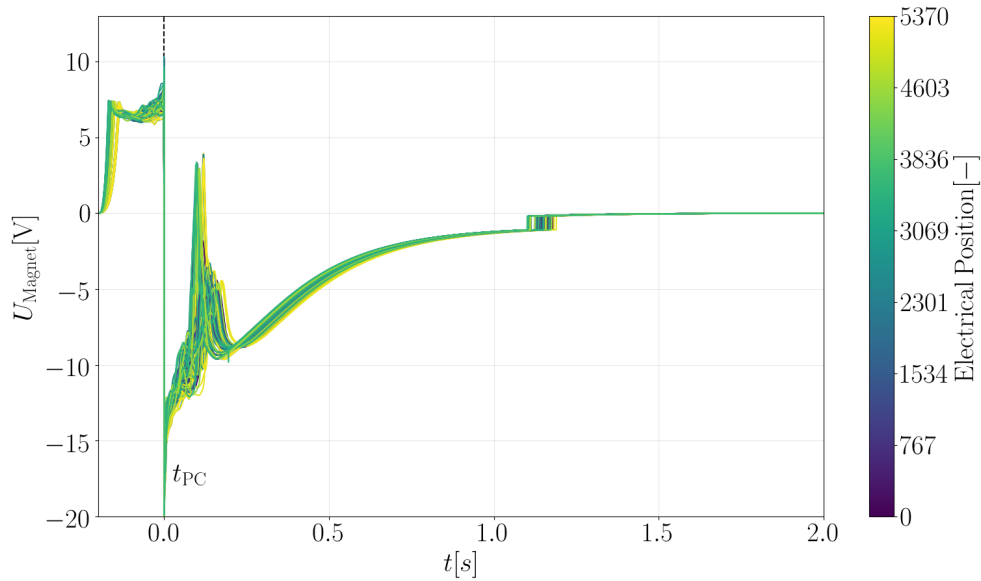


Figure G.17: Voltage across the MCBYH dipole in an FPA at $t_{PC} = 0$ s for all selected initial quench positions from nominal current. Colors indicate the electrical position of the assumed quench hot-spot, with negative lead at 5370 and positive lead at 0.

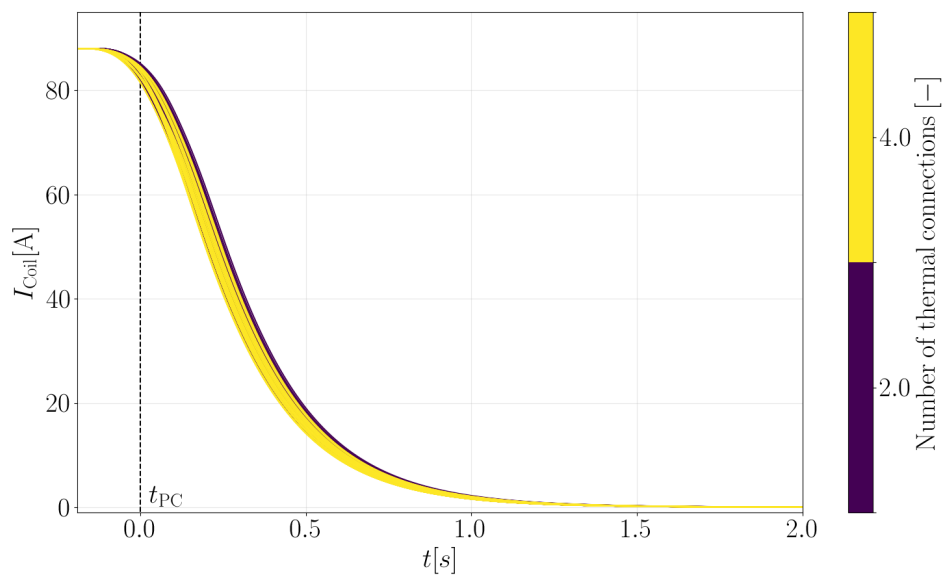


Figure G.18: Decay of the magnet current in an FPA at $t_{\text{PC}} = 0$ s for all selected initial quench positions from nominal current. Colors the number of neighboring turns to the first quenching turn.

H Annex to Chapter 5

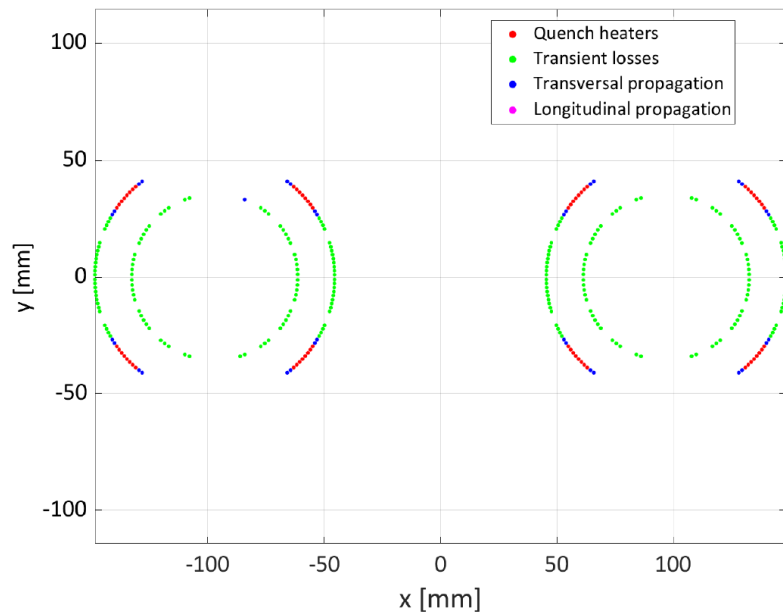


Figure H.19: Cause of quench of each half-turn in the first quenching MB magnet, for the presented event in Chapter 5

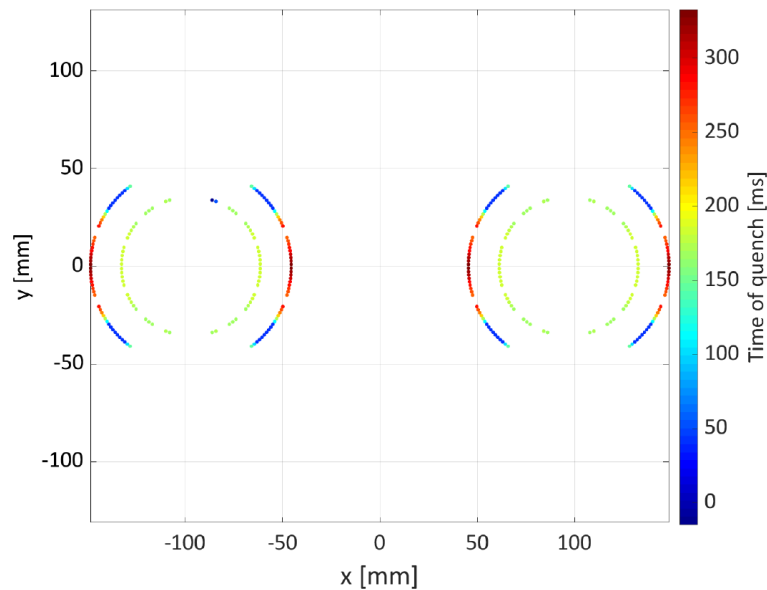


Figure H.20: Time of quench of each half-turn in the first quenching MB magnet, for the presented event in Chapter 5

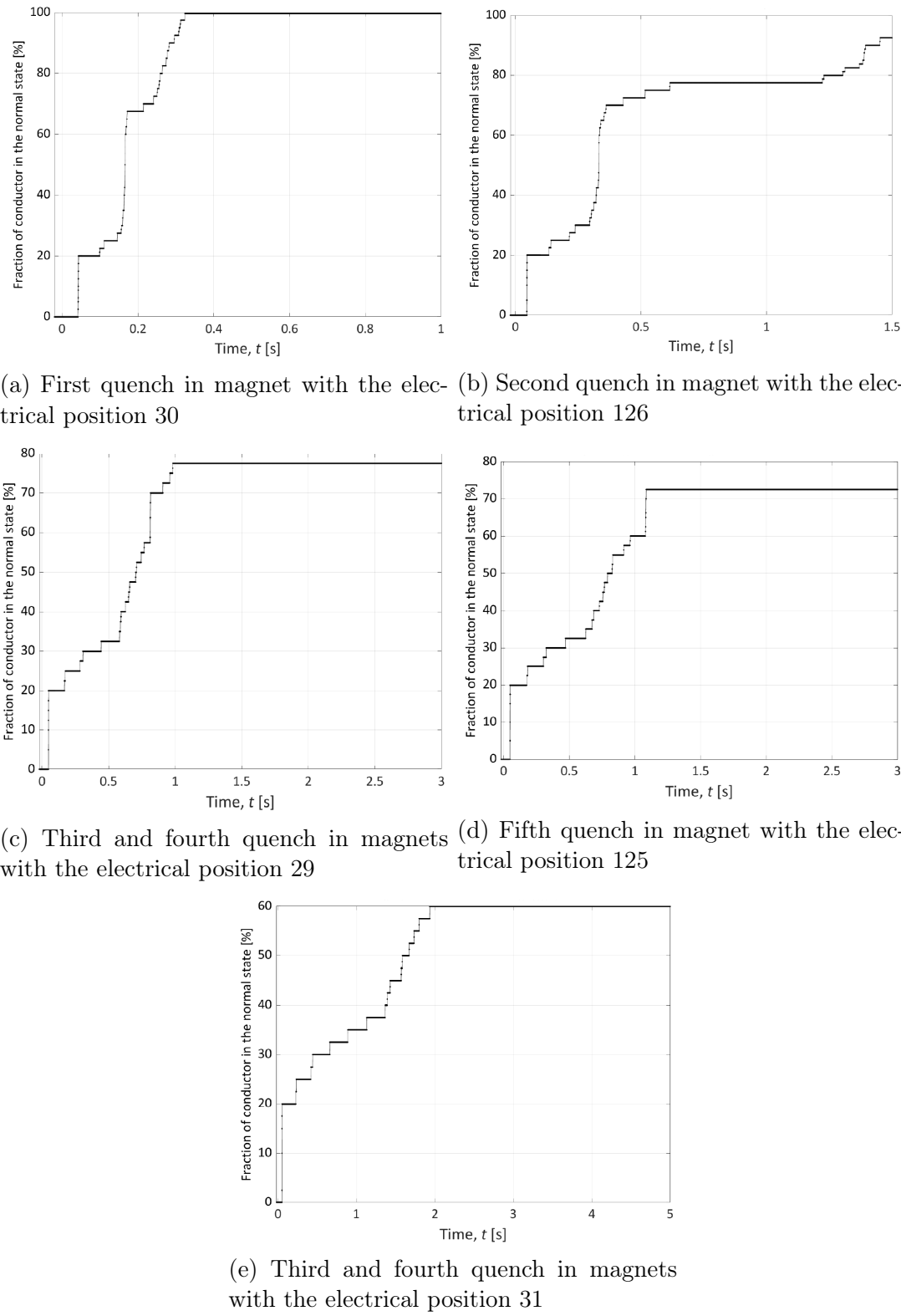


Figure H.21: Fraction of conductor, transferred into normal state for the simulations at different current levels. $t = 0$ s corresponds to the start of each simulation.

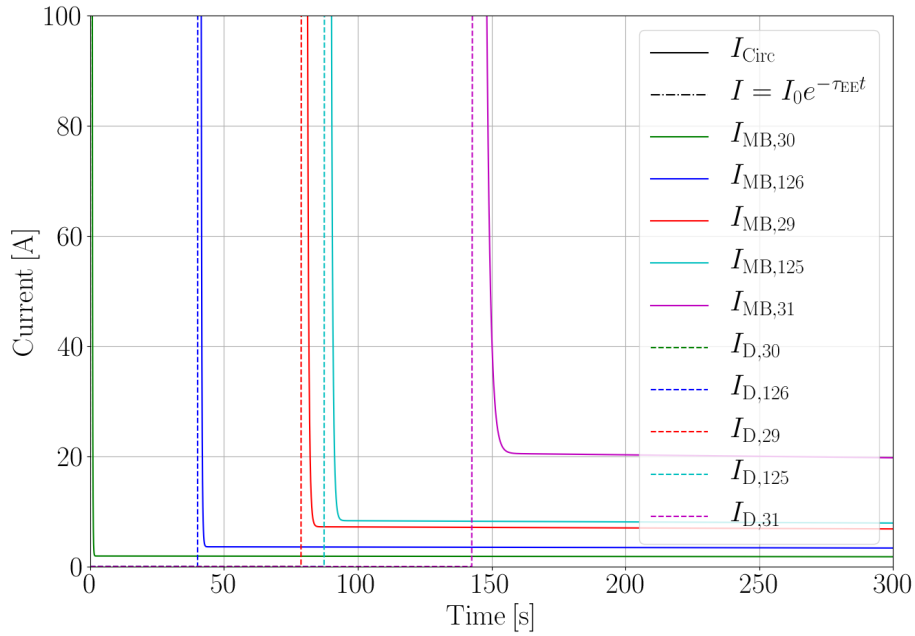


Figure H.22: Remaining current flow in the magnets after the discharge in each magnet, shown for each quenching magnet

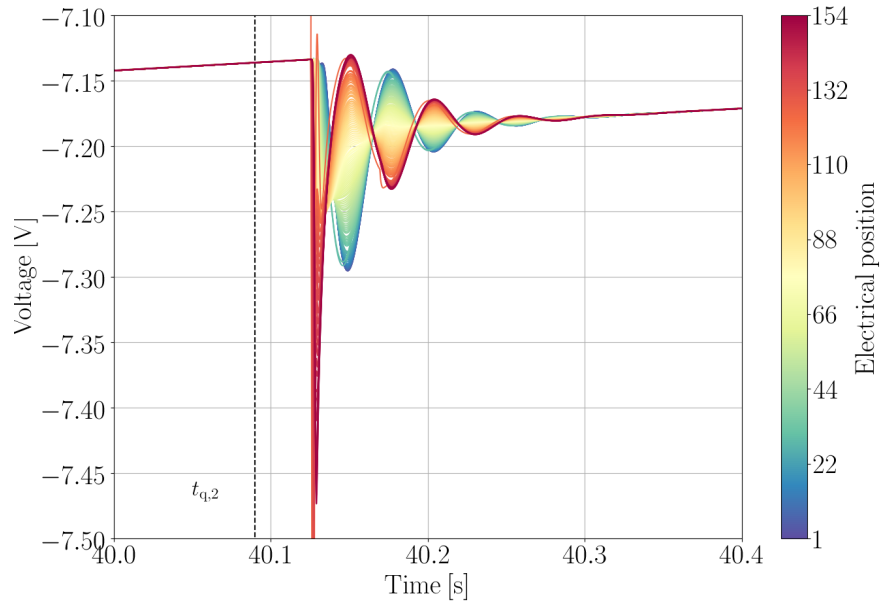


Figure H.23: Voltages across each magnet in the RB circuit, shortly after the second quench at $t_{q,2}$ in the magnet with the electrical position 126

References

- [1] O. Bruening et al. *LHC Design Report: Volume I The LHC Main Ring*. Geneva, Switzerland, 2004. URL: <https://cds.cern.ch/record/782076>.
- [2] STEAM Team. *STEAM: Simulation of Transient Effects in Accelerator Magnets*. URL: <https://espace.cern.ch/steam/>.
- [3] CERN. “CERN: Website About and Science”. In: (2021). URL: <https://home.cern/>.
- [4] Education, Communications and Outreach Group. *FAQ - LHC the guide*. February 2017. URL: https://home.cern/sites/home.web.cern.ch/files/2018-07/CERN-Brochure-2017-002-Eng_0.pdf.
- [5] CERN. *LHC Season 2: Facts & Figures*. URL: https://home.cern/sites/home.web.cern.ch/files/2018-07/factsandfigures-en_0.pdf.
- [6] Esma Mobs. *The CERN accelerator complex - 2019: Complexe des accélérateurs du CERN - 2019*. URL: <https://cds.cern.ch/record/2684277>.
- [7] Oliver Brüning and Lucio Rossi. *The High Luminosity Large Hadron Collider*. Vol. 24. WORLD SCIENTIFIC, 2015. ISBN: 978-981-4675-46-8. DOI: 10.1142/9581.
- [8] CERN TE-MSC-TF section. *SM-18 Test facilities*. URL: <https://espace.cern.ch/te-dep-msc-tf-archived2018>.
- [9] R. Kleiner and W. Buckel. *Superconductivity: An Introduction*. Wiley, 2015. ISBN: 9783527411627.
- [10] Ivan A. Parinov. *Microstructure and Properties of High-Temperature Superconductors*. Berlin, Heidelberg: Springer-Verlag Berlin Heidelberg, 2007. ISBN: 9783540709770. DOI: 10.1007/978-3-540-70977-0. URL: <http://site.ebrary.com/lib/alltitles/docDetail.action?docID=10190521>.
- [11] Stephan Russenschuck. *Field Computation for Accelerator Magnets*. Weinheim, Germany: Wiley-VCH Verlag GmbH & Co. KGaA, 2010. ISBN: 9783527635467. DOI: 10.1002/9783527635467.
- [12] L. Bortot. *Introduction to Superconductivity and Superconducting Magnets*. 26.11.2020. URL: <https://indico.cern.ch/event/884989/>.
- [13] Wikipedia contributors. *Type-II superconductor*. 3 September 2021. URL: https://en.wikipedia.org/w/index.php?title=Type-II_superconductor&oldid=1034767245.

REFERENCES

- [14] D. Schoerling. *Superconducting accelerator magnets*. 19th of May 2021. URL: https://indico.cern.event/1018359/contributions/4312237/attachments/2246966/3811056/Schoerling_CASatEAS_2021.pdf.
- [15] Martin N. Wilson. *Superconducting magnets*. Vol. 2. Monographs on cryogenics. Oxford: Clarendon Pr, 1983. ISBN: 0198548052. URL: <http://www.loc.gov/catdir/enhancements/fy0636/82018869-d.html>.
- [16] E. Ravaioli. “CLIQ: A new quench protection technology for superconducting magnets”. PhD thesis. University of Twente, 2015. URL: <https://cds.cern.ch/record/2031159?ln=de>.
- [17] D. Larbalestier et al. “High-Tc superconducting materials for electric power applications”. In: *Nature* 414 (2001), pp. 368–377. URL: <https://doi.org/10.1038/35104654>.
- [18] Steve Myers. “The engineering needed for particle physics”. In: *Philosophical transactions. Series A, Mathematical, physical, and engineering sciences* 370.1973 (2012), pp. 3887–3923. ISSN: 1364-503X. DOI: [10.1098/rsta.2011.0053](https://doi.org/10.1098/rsta.2011.0053).
- [19] L. Bottura. *Cable Stability*. 2014. DOI: [10.5170/CERN-2014-005.401](https://doi.org/10.5170/CERN-2014-005.401).
- [20] E. Tedesco. *Unit 12 - Protection principles*. 4.09.2020. URL: <https://indico.cern.ch/category/12408/>.
- [21] A. Verweij. “LHC - Cable and Strand characteristics”. In: Internal distribution (CERN).
- [22] D. Calcoen. *QPS for Dummies*. URL: <https://wikis.cern.ch/display/MPEEP/QPS+for+Dummies>.
- [23] A. P. Verweij. “Electrodynamics of Superconducting Cables in Accelerator Magnets”. PhD thesis. University of Twente, 1995. URL: <https://cds.cern.ch/record/292595?ln=de>.
- [24] E. Ravaioli et al. “Lumped-Element Dynamic Electro-Thermal model of a superconducting magnet”. In: *Cryogenics* 80.2 (2016), pp. 346–356. ISSN: 00112275. DOI: [10.1016/j.cryogenics.2016.04.004](https://doi.org/10.1016/j.cryogenics.2016.04.004).
- [25] G. H. Morgan. “Theoretical Behavior of Twisted Multicore Superconducting Wire in a Time-Varying Uniform Magnetic Field”. In: *Journal of Applied Physics* 41.9 (1970), pp. 3673–3679. ISSN: 0018-9219. DOI: [10.1063/1.1659491](https://doi.org/10.1063/1.1659491).
- [26] E. Tedesco. *Unit 13 - Protection systems*. 18.09.2020. URL: <https://indico.cern.ch/category/12408/>.

- [27] D. Pracht. “Multiphysics modelling of the LHC main quadrupole superconducting circuit”. Master Thesis. Hochschule Hannover, 2019. URL: <http://cds.cern.ch/record/2681097/files/CERN-THESIS-2019-071.pdf>.
- [28] F. Rodriguez-Mateos and F. Sonnemann. “Quench heater studies for the LHC magnets”. In: *PACS2001. Proceedings of the 2001 Particle Accelerator Conference (Cat. No.01CH37268)*. IEEE, 18-22 June 2001, pp. 3451–3453. ISBN: 0-7803-7191-7. DOI: [10.1109/PAC.2001.988141](https://doi.org/10.1109/PAC.2001.988141).
- [29] E. Ravaioli et al. “New, Coupling Loss Induced, Quench Protection System for Superconducting Accelerator Magnets”. In: *IEEE Transactions on Applied Superconductivity* 24.3 (2014), pp. 1–5. ISSN: 1051-8223. DOI: [10.1109/TASC.2013.2281223](https://doi.org/10.1109/TASC.2013.2281223).
- [30] STEAM Team. *STEAM-COSIM*. URL: <https://espace.cern.ch/steam/COSIM>.
- [31] L. Bortot et al. “STEAM: A hierarchical cosimulation framework for superconducting accelerator magnet circuits”. In: *IEEE Transactions on applied superconductivity* (2017). URL: <https://doi.org/10.1109/TASC.2017.2787665>.
- [32] M. Maciejewski. “Co-simulation of transient effects in superconducting accelerator magnets”. PhD. Thesis. 2019. URL: <http://cds.cern.ch/record/2675039>.
- [33] Frank P. Incropera et al. *Fundamentals of heat and mass transfer*. 6. ed. Hoboken, NJ: Wiley, 2007. ISBN: 978-0-471-45728-2. URL: <http://www.loc.gov/catdir/enhancements/fy0626/2005058360-d.html>.
- [34] F. Murgia. “Multiphysics Modelling of the LHC Individually Powered Quadrupole Superconducting Circuits”. Master thesis. Alma Mater Studiorum - University of Bologna, 2020. URL: <https://cds.cern.ch/record/2729131/files/CERN-THESIS-2020-102.pdf>.
- [35] STEAM Team. *SIGMA Documentation v2.0*. Geneva, Switzerland, 2019. URL: <https://edms.cern.ch/document/2141579>.
- [36] E. Ravaioli and STEAM Team. *STEAM LEDET - User Manual*. 2019. URL: <https://edms.cern.ch/document/2046824/1.06.04>.
- [37] M. Janitschke et al. “A Simplified Approach to Simulate Quench Development in a Superconducting Magnet”. In: *IEEE Transactions on Applied Superconductivity* (2021). URL: [10.1109/TASC.2021.3059980](https://doi.org/10.1109/TASC.2021.3059980).

REFERENCES

- [38] H. ten Kate, H. Boschman, and L. van de Klundert. “Longitudinal propagation velocity of the normal zone in superconducting wires”. In: *IEEE Transactions on Magnetics* 23.2 (1987), pp. 1557–1560. ISSN: 0018-9464. DOI: 10.1109/TMAG.1987.1065020.
- [39] H. H. J. ten Kate. *Superconducting Magnets: Quench Propagation and Protection*. 2013. URL: https://indico.cern.ch/event/194284/contributions/1472819/attachments/281522/393603/TenKate_-_CAS_-Handout-Quench-Erice-2103.pdf.
- [40] PSPICE. 2020. URL: <https://www.pspice.com/>.
- [41] M. Maciejewski. *Co-Simulation of Transient Effects in Superconducting Accelerator Magnets*. 13-14 June 2019. URL: <https://indico.cern.ch/event/808547/contributions/3367281/>.
- [42] STEAM Team. *STEAM Co-Sim - User Manual*. 2018. URL: https://edms.cern.ch/ui/file/2047054/1/STEAM_Co-sim_user_manual.pdf.
- [43] Stephan Russenschuck. *ROXIE: the Routine for the Optimization of Magnet X-sections, Inverse Field Computation and Coil End Design*. 1993. DOI: 10.5170/CERN-1999-001.1.
- [44] Stephan Russenschuck. *1st International Roxie Users Meeting and Workshop*. 1999. DOI: 10.5170/CERN-1999-001.
- [45] STEAM Team. *STEAM notebook API*. URL: <https://gitlab.cern.ch/steam/steam-notebook-api>.
- [46] STEAM Team. *STEAM notebooks*. URL: <https://gitlab.cern.ch/steam/steam-notebooks>.
- [47] LHC Signal Monitoring team. *LHC Signal Monitoring Project Overview: API for logging db query and signal processing*. URL: <http://sigmon-docs.web.cern.ch/overview/>.
- [48] *LHC ROXIE Magnets Repository*. URL: <http://roxie-lhc-magnets.web.cern.ch/roxie-LHC-magnets/MCBY/>.
- [49] H. Durand. *MCBYH - WIDE APERTURE DIPOLE CORREC - DIPOLE MODULE*. 28.03.2000. URL: https://edms5.cern.ch/cdd/plsql/c4w.display_details?cookie=2656074&p_drob_id=422754&p_version=**.
- [50] CERN TE-EPC-LPC section. *LHC ATLAS power converters, LHC 120 A - 10 V*. URL: <http://te-epc-lpc.web.cern.ch/te-epc-lpc/converters/lhc120a-10v/general.stm>.

- [51] N. J. Simon, E. S. Drexler, and R. P. Reed. *Properties of copper and copper alloys at cryogenic temperatures. Final report*. Ed. by NIST Monograph 177. 1992. DOI: 10.6028/NIST.MONO.177.
- [52] *Handbook of applied superconductivity*. Bristol: Inst. of Physics Publ, 1998. ISBN: 978-0750303774.
- [53] CERN TE-EPC-LPC section. *LHC ATLAS power converters, LHC4-6-8kA-08V*. URL: <http://te-epc-lpc.web.cern.ch/te-epc-lpc/converters/lhc4-6-8ka-08v/general.stm>.
- [54] Akriyi Liakopoulou. “Analysis of Short-Circuit Transients in the LHC Main Dipole Circuit and Development of an Automated Analysis Algorithm”. Master Thesis. Enschede: University of Twente, 2019. URL: <http://cds.cern.ch/record/2676750>.
- [55] LHC-SIGMON Team. *Hardware Commissioning notebooks: Analysis of an FPA in an RB Circuit*. 2021.
- [56] Z. Charifouline and LHC-SIGMON Team. *Powering Procedure and Acceptance Criteria for the 13 kA Dipole Circuits*. 2021. URL: <https://edms.cern.ch/document/874713>.
- [57] R. Denz. “Electronic Systems for the Protection of Superconducting Elements in the LHC”. In: *IEEE Transactions on Applied Superconductivity* 16.2 (2006), pp. 1725–1728. ISSN: 1051-8223. DOI: 10.1109/TASC.2005.864258.
- [58] Reiner Denz et al. “Upgrade of the Protection System for the Superconducting Elements of the LHC During LS1”. In: *IEEE Transactions on Applied Superconductivity* 24.3 (2014), pp. 1–4. ISSN: 1051-8223. DOI: 10.1109/TASC.2013.2283101.
- [59] E. Ravaioli et al. “Impact of the Voltage Transients After a Fast Power Abort on the Quench Detection System in the LHC Main Dipole Chain”. In: *IEEE Transactions on Applied Superconductivity* 22.3 (2012), p. 9002504. ISSN: 1051-8223. DOI: 10.1109/TASC.2012.2183572.
- [60] E. Ravaioli et al. “Modeling of the Voltage Waves in the LHC Main Dipole Circuits”. In: *IEEE Transactions on Applied Superconductivity* 22.3 (2012), p. 9002704. ISSN: 1051-8223. DOI: 10.1109/TASC.2011.2176306.

REFERENCES

- [61] Stephan Russenschuck, ed. *ROXIE: routine for the optimization of magnet x-sections, inverse field calculation and coil end design: First International Roxie Users Meeting and Workshop, CERN, 16 - 18 March, 1998 ; proceedings.* Geneva, 1999. ISBN: 9290831405.
- [62] E. Ravaioli, A. P. Verweij, and Herman H. J. ten Kate. “Unbalanced Impedance of the Aperture Coils of Some LHC Main Dipole Magnets”. In: *IEEE Transactions on Applied Superconductivity* 23.3 (2013), p. 4000104. ISSN: 1051-8223. DOI: 10.1109/TASC.2012.2227650.
- [63] B. T. Matthias, T. H. Geballe, and V. B. Compton. “Superconductivity”. In: *Reviews of Modern Physics* 35.1 (1963), pp. 1–22. ISSN: 0034-6861. DOI: 10.1103/RevModPhys.35.1.
- [64] B. T. Matthias et al. “Superconductivity of Nb₃ Sn”. In: *Physical Review* 95.6 (1954), p. 1435. ISSN: 0031-899X. DOI: 10.1103/PhysRev.95.1435.
- [65] J. Nagamatsu et al. “Superconductivity at 39 K in magnesium diboride”. In: *Nature* 410.6824 (2001), pp. 63–64. ISSN: 0028-0836. DOI: 10.1038/35065039.
- [66] S. Mozaffari et al. “Superconducting phase diagram of H₃S under high magnetic fields.” In: *Nature Communications* 10 (2019). URL: <https://doi.org/10.1038/s41467-019-10552-y>.